SAND2014-17443 O

Draft Report: Results of Stainless Steel Canister Corrosion Studies and Environmental Sample Investigations

Fuel Cycle Research & Development

Prepared for
U.S. Department of Energy
Used Fuel Disposition Program

Charles Bryan and David Enos
Sandia National Laboratories
September 5, 2014

FCRD-UFD-2014-000316
SAND2014-xxxx

Sandia National Laboratories is a multi-program laboratory managed and operated by Sandia Corporation, a wholly owned subsidiary of Lockheed Martin Corporation, for the U.S. Department of Energy's National Nuclear Security Administration under contract DE-AC04-94AL85000.

Sandia
National
Laboratories

Page reserved for Document Submittal Sheet

SUMMARY

This progress report describes work being done at Sandia National Laboratories (SNL) to assess the localized corrosion performance of container/cask materials used in the interim storage of used nuclear fuel. The work involves both characterization of the potential physical and chemical environment on the surface of the storage canisters and how it might evolve through time, and testing to evaluate performance of the canister materials under anticipated storage conditions.

To evaluate the potential environment on the surface of the canisters, SNL is working with the Electric Power Research Institute (EPRI) to collect and analyze dust samples from the surface of in-service SNF storage canisters. In FY 13, SNL analyzed samples from the Calvert Cliffs Independent Spent Fuel Storage Installation (ISFSI); here, results are presented for samples collected from two additional near-marine ISFSI sites, Hope Creek NJ, and Diablo Canyon CA. The Hope Creek site is located on the shores of the Delaware River within the tidal zone; the water is brackish and wave action is normally minor. The Diablo Canyon site is located on a rocky Pacific Ocean shoreline with breaking waves.

Two types of samples were collected: SaltSmart™ samples, which leach the soluble salts from a known surface area of the canister, and dry pad samples, which collected a surface salt and dust using a swipe method with a mildly abrasive ScotchBrite™ pad. The dry samples were used to characterize the mineralogy and texture of the soluble and insoluble components in the dust via microanalytical techniques, including mapping X-ray Fluorescence spectroscopy and Scanning Electron Microscopy. For both Hope Creek and Diablo Canyon canisters, dust loadings were much higher on the flat upper surfaces of the canisters than on the vertical sides. Maximum dust sizes collected at both sites were slightly larger than 20 µm, but *Phragmites* grass seeds ~1 mm in size, were observed on the tops of the Hope Creek canisters. At both sites, the surface dust could be divided into fractions generated by manufacturing processes and by natural processes. The fraction from manufacturing processes consisted of variably-oxidized angular and spherical particles of stainless steel and iron, generated by machining and welding/cutting processes, respectively. Dust from natural sources consisted largely of detrital quartz and aluminosilicates (feldspars and clays) at both sites. At Hope Creek, soluble salts were dominated by sulfates and nitrates, mostly of calcium. Chloride was a trace component and the only chloride mineral observed by SEM was NaCl. Chloride surface loads measured by the Saltsmart™ sensors were very low, less than 60 mg m^{-2} on the canister top, and less than 10 mg m^{-2} on the canister sides. At Diablo Canyon, sea-salt aggregates of NaCl and $Mg\text{-}SO_4$, with minor K and Ca, were abundant in the dust, in some cases dominating the observed dust assemblage. Measured Saltsmart™ chloride surface loads were very low (<5 mg m^{-2}); however, high canister surface temperatures damaged the Saltsmart™ sensors, and, in light of the SEM observations of abundant sea-salts on the package surfaces, the measured values may not be valid.

Experimental efforts at SNL to assess corrosion of interim storage canister materials include three tasks in FY14. First, a full-diameter canister mockup, made using materials and techniques identical to those used to make interim storage canisters, was designed and ordered from Ranor Inc., a cask vendor for

Areva/TN. The mockup will be delivered prior to the end of FY14, and will be used for evaluating weld residual stresses and degrees of sensitization for typical interim storage canister welds. Following weld characterization, the mockup will be sectioned and provided to participating organizations for corrosion testing purposes. A test plan is being developed for these efforts.

In a second task, experimental work was carried out to evaluate crevice corrosion of 304SS in the presence of limited reactants, as would be present on a dust-covered storage canister. This work tests the theory that limited salt loads will limit corrosion penetration over time, and is a continuation of work carried out in FY13. Laser confocal microscopy was utilized to assess the volume and depth of corrosion pits formed during the crevice corrosion tests. Results indicate that for the duration of the current experiments (100 days), no stifling of corrosion occurred due to limitations in the amount of reactants present at three different salt loadings.

Finally, work has been carried out this year perfecting an instrument for depositing sea-salts onto metal surfaces for atmospheric corrosion testing purposes. The system uses an X-Y plotter system with a commercial airbrush, and deposition is monitored with a quartz crystal microbalance. The system is capable of depositing very even salt loadings, even at very low total deposition rates.

CONTENTS

FIGURES

TABLES

ACRONYMS

ASME B&PVC	American Society of Mechanical Engineers Boiler and Pressure Vessel Code
ASTM	American Society for Testing and Materials
DOE	Department of Energy
EDS	energy dispersive [X-ray] spectroscopy
EPR	Electrochemical Reactivation
EPRI	Electric Power Research Institute
FCRD	Fuel Cycle Research and Development
IC	ion chromatography
ICP-OES	inductively coupled plasma-optical emission spectroscopy
ISFSI	independent spent fuel storage installation
NWTRB	Nuclear Waste Technical Review Board
NRC	Nuclear Regulatory Commission
QCM	Quartz Crystal Microbalance
SCC	stress corrosion cracking
SEM	scanning electron microscope
SNF	spent nuclear fuel
SNL	Sandia National Laboratories
UFD	Used Fuel Disposition
XRD	X-ray diffraction
XRF	X-ray fluorescence

DRAFT REPORT: RESULTS OF STAINLESS STEEL CANISTER CORROSION STUDIES AND ENVIRONMENTAL SAMPLE INVESTIGATIONS

1. INTRODUCTION

This progress report describes work being done at Sandia National Laboratories (SNL) to assess the localized corrosion performance of container/cask materials used in the interim storage of used nuclear fuel. The work involves both characterization of the potential physical and chemical environment on the surface of the storage canisters and how it might evolve through time, and testing to evaluate performance of the canister materials under anticipated storage conditions.

To evaluate the potential environment on the surface of the canisters, SNL is working with the Electric Power Research Institute (EPRI) as part of a cooperative research and development agreement (CRADA) to collect and analyze dust samples from the surface of in-service spent nuclear fuel (SNF) storage canisters. In FY 13, SNL analyzed samples from the Calvert Cliffs Independent Spent Fuel Storage Installation (ISFSI); here, results are presented for samples collected from two additional near-marine ISFSI sites, Hope Creek, New Jersey, and Diablo Canyon, California. The Hope Creek site is located on the shores of the Delaware River within the tidal zone; the water is brackish and wave action is normally minor. The Diablo Canyon site is located on a rocky Pacific Ocean shoreline with breaking waves. This cooperative work provides the first real data on the mineralogical and chemical composition of in-service canister surface deposits. The emphasis of the work is to identify and quantify, per unit area, the soluble salts present on the canister surfaces. Upon deliquescence, these salts could represent potentially corrosive brines that could support stress corrosion cracking of the in-service canisters. The results of these analyses are provided in Section 2.

Also discussed here are experimental efforts at SNL to assess corrosion of interim storage canister materials. This includes several efforts. First, a full-diameter waste package mockup, made using materials and techniques identical to those used to make interim storage canisters was designed and ordered from Ranor Inc., a cask vendor that supplies storage canisters to Areva/TN (NUHOMS canisters). The cask will be delivered prior to the end of FY14, and will be used for evaluating weld residual stresses and degrees of sensitization for typical interim storage canister welds. Following weld characterization, the mockup will be sectioned and provided to participating organizations for corrosion testing purposes. A test plan is being developed for these efforts. The mockup design and preliminary testing plans are discussed in Section 3.

Section 4 presents additional experimental work was carried out to evaluate crevice corrosion of 304SS in the presence of limited reactants, as would be present on a dust-covered storage canister. This work tests the theory that limited salt loads will limit corrosion penetration over time, and is a continuation of work carried out last year. Laser confocal microscopy was utilized to assess the volume and depth of corrosion pits formed during the crevice corrosion tests. Results indicate that for the duration of the current experiments (100 days), no stifling of corrosion occurred due to limited reactants at three different salt loadings.

Finally, Section 5 describes an instrument that has been perfected this year for depositing sea-salts onto metal surfaces for atmospheric corrosion testing purposes. The system uses an X-Y plotter system with a commercial airbrush, and deposition is monitored with a quartz crystal microbalance. The system is capable of depositing very even salt loadings, even at very low total deposition rates.

2. ANALYSIS OF DUST SAMPLES COLLECTED FROM THE SURFACE OF IN-SERVICE SNF STORAGE CANISTERS

2.1 Overview

When spent nuclear fuel (SNF) storage pools at commercial nuclear reactors become filled to capacity, it is necessary to shift SNF to dry storage systems. Modern dry storage systems consist of a stainless steel canister within an overpack that protects the canister from the weather. Decay heat from the waste drives convective airflow through an annulus between the overpack and the canister, cooling the container. Over time, dust, drawn into the overpacks with the circulating air, is deposited on the surfaces of containers within the storage systems. Salts within the dust will deliquesce as heat production declines over time and the packages cool, and it is possible that deliquescence-induced corrosion of the stainless steel waste container could lead to penetration of the container walls by chloride-induced stress corrosion cracking (SCC). To address this concern, the Electrical Power Research Institute (EPRI) has instituted a sampling program for the dust on the surface of in-service SNF storage canisters. The first samples were collected from a NUHOMS horizontal storage system at the Calvert Cliffs Independent Spent Fuel Storage Installation (ISFSI) in June 2012, 15.6 years after waste emplacement (Calvert Cliffs Nuclear Power Plant, 2012). In November 2013, the second set of samples was collected at Hope Creek, from canisters in storage for 6 years; and in January, 2014, a third set was collected from Diablo Canyon, from canisters in storage for 2-4 years. The Calvert Cliffs samples were analyzed in part by an external lab contracted by EPRI, and in part by Sandia and are reported elsewhere (Calvert Cliffs Nuclear Power Plant, 2013; DOE, 2013). The samples from the Hope Creek and Diablo Canyon sites were sent to Sandia National Laboratories (SNL) for characterization.

This chapter summarizes the results of analyses of dust samples collected from the surface of SNF dry storage containers at the Hope Creek and Diablo Canyon ISFSIs. The dry storage systems that were sampled are Holtec HI-STORM 100S-218, Version B systems, which have a 304 SS storage cask placed into a vertical steel-lined concrete overpack (Figure 1). The system is passively ventilated via four air inlet vents at the base of the unit located 90º from each other, and four outlet vents on the top, offset 45º circumferentially from the inlets.

Both wet and dry samples of the dust/salts were collected at each site, using two different devices:

- The wet samples were collected using SaltSmart™ sensors. These devices are manufactured by Louisville Solutions, Inc., and used in shipyards to quantify the amount of chloride on metal surfaces per unit area. They are designed for use with very low salt loadings. For this study, the sensors were mounted on a remote sampling tool developed by Holtec and lowered into the overpack through one of the outlet vents. Each sensor has a flat wick, which was pressed flat against the metal surface pneumatically; for samples taken from the flat top of the canisters, the sensors were pressed against the surface manually, using a long rod. A small amount of deionized water was then injected into one end of the sensor, and was drawn across the wick by capillary processes to a reservoir pad within the body of the sensor. In the shipyard application, the conductivity of the reservoir pad (a function of the total dissolved salts in the water) is monitored, and is used to estimate the chloride concentration on the metal surface, assuming that the salts are similar in composition to sea salts. For this study, the sensors were placed in sealed screw-cap polypropylene centrifuge tubes after retrieval from the overpack and shipped overnight to SNL, packed with ice packs to keep them cool. At Sandia, the sensors were disassembled and the soluble salts were rinsed from the internal components and leached out of the wicks and pads with deionized water and retained for chemical analysis. Rather than estimating chloride concentration from conductivity, the salt compositions were measured directly.
- Dry dust samples were collected using a similar remote sampling tool, equipped a scraper tool instead of the SaltSmart™ sensor. The scraper tool consisted of a rectangular piece of a mildly abrasive

Scotch-Brite™ sponge-like pad, backed with a steel plate. As with the SaltSmart™, once the sampling tool was in position, the pad was pneumatically pushed against the canister surface. However, in the case of the dry sampling tool, a second pneumatic valve then moved the pad back and forth across the surface, to dislodge and collect the dust. Once again, canister-top samples were collected by using a long rod to manually brush the over the surface. Following retrieval from the overpack, the dry pad samples were removed from the sampling tool, placed into a screw-cap centrifuge tube, and sent to SNL for characterization of the collected dust.

Figure 1. Holtec HI-STORM dry cask storage systems at Diablo Canyon.

At SNL, the wet samples were analyzed by chemical analysis to determine the composition and abundance of soluble salts present. The pads containing the dry dust were removed from the steel plate backers and analyzed by X-ray fluorescence to obtain bulk chemical compositions. Then, a small portion of the sponge was removed and retained for scanning electron microscope analysis. The remaining sponge was washed thoroughly with deionized water and the leachate collected, filtered, and analyzed for soluble salts. Original plans were for the remaining insoluble residue to be digested and analyzed using wet chemical methods. However, because of extensive contamination by talc shed from the pad matrix, it was decided not to determine the bulk chemistry of the insoluble fraction.

Methods used to characterize the samples include:

- **X-ray fluorescence (XRF) analysis.** This method was implemented as a microbeam technique, allowing chemical mapping of the dry dust samples on the surface of the collection pads, with a resolution of ~100 µm. It provides semi-quantitative chemical analyses; yielding element ratios that can be used in mass balance and normative mineral calculations. However, one limitation is that elements lighter than sodium (e.g. oxygen, nitrogen, carbon) cannot be detected.

- **Scanning Electron Microscopy (SEM) imaging and energy dispersive system (EDS) element mapping**. SEM/EDS analysis of the dry dust samples provides textural and mineralogical information of dust/dust components, and allows visual identification of organic matter (floral/faunal fragments).
- **X-ray diffraction (XRD) analysis**. This analysis did not prove useful—the surface of the pads was too rough for effective measurement, and no mineral peaks could be identified.
- **Chemical analyses of the dust and soluble salts**. The soluble salts were leached form the SaltSmart™ sensors and analyzed. For the dry samples, the pad was washed thoroughly with deionized water and the leachate collected and filtered. The leachate was then analyzed for soluble salts.

As discussed in the following sections, although both the wet and dry sampling methods had limitations, the analyses were effective in identifying the major mineralogy of the dust on the canister surfaces, and the composition of the salts present. The Hope Creek ISFSI is located ~0.25 mile from the Delaware River, about 15 upstream from Delaware Bay. The Delaware River is subject to tides at the site, and is brackish in composition. The Hope Creek canisters had very light salt surface loads, and higher dust and salt concentrations occurred on the canister tops than on the vertical sides. Soluble salts were dominantly calcium, nitrate, sulfate, and carbonate compounds; an assemblage consistent with continental rather than marine aerosol assemblages. Chloride salts, mostly occurring as NaCl, were very rare.

The Diablo Canyon ISFSI is located ~0.35 miles from the Pacific Ocean. In contrast to the Hope Creek samples, dust collected from the surfaces of dry storage canisters at Diablo Canyon were chloride-rich. The chloride was present as sea-salt aggregates consisting dominantly of intergrown NaCl and an Mg-SO_4 phase. The aggregates had characteristic morphologies, occurring as hollow spherical aggregates of halite with interstitial Mg-SO_4 or as euhedral skeletal crystals of halite (NaCl) with sheaf-like bundles of Mg-SO_4. The morphology suggests that the crystals formed by evaporation of droplets of seawater suspended in the atmosphere, drying from the outside inwards. The aggregates were commonly 5-20 microns in diameter. Dust and chloride loads were much heavier on the canister tops than the sides, and the two Diablo Canyon canisters sampled showed distinct variations in salt chemistry. Dusts on the side of one of the canisters, MPC-123, appeared to contain a significantly larger continental dust component than the other canister.

Detailed sampling and analytical methods, and a list of the samples collected, are provided in Section 2.2 and Section 2.3 of this report. Section 2.4 presents and discusses the results of the different analyses, and Section 2.5 provides a summary. This report provides typical results for the samples from the different ISFSI sites and canisters; for a complete suite of the SEM/EDS and XRF analyses performed, is provided in Bryan and Enos (2014).

2.2 Samples

Sampling at Hope Creek and Diablo Canyon was carried out through one of the upper ventilation openings on each package. After removal of the screen covering the opening, spot welds holding the gamma shield in place were cut, and the gamma shield extracted. Then a guide rail for the sampling device for the side of the package was inserted into the opening by workers on a scissor lift (Figure 2). This rail guided the remote sampling tool down into the narrow (~2 inch) annulus between the canister and the overpack. The sampling tool was forced down the annulus with a steel ribbon, with trailing tubing to operate a pneumatic system on the sampling head. The wet samples were collected using SaltSmart™ sensors, which are used in shipyards to quantify the amount of salts on metal surfaces per unit area. The sensors were mounted on the sampling head in a shallow recess, so that they did not contact the metal surface during the emplacement process. Each sensor has a flat wick, which was pressed flat against the metal surface pneumatically. A small amount of deionized water was then injected into one end of the sensor, and was drawn across the wick by capillary forces to a reservoir pad within the body of the sensor. In the shipyard application, the conductivity of the pad (a function of the total dissolved salts in the water) is monitored, and is used to estimate the chloride concentration on the metal surface, assuming that the salts are similar in composition to sea salts. For this study, the sensors were retained and disassembled at Sandia, where the salts were leached and analyzed to determine composition. Testing has shown that under appropriate conditions, the SaltSmart™ sensors can provide an accurate assessment of the amount and composition of salts on the canister surface (Memo from C. Bryan to L. Zsidai dated Nov. 13, 2013; SAND#2013-9948P).

Figure 2. Sampling dust from the surface of interim storage canisters within their overpacks.

Dry dust samples were collected using a similar remote sampling tool, equipped a scraper tool instead of the SaltSmart™ sensor. The scraper tool consisted of a rectangular piece of a mildly abrasive Scotch-Brite™ sponge-like pad, backed with a steel plate. Once in position, the pad was pneumatically pushed against the canister surface, and a second pneumatic controller moved the pad back and forth across the surface, to dislodge and collect the dust.

Access to the canister top surfaces was less restricted, so instead of using the pneumatically-powered remote sampling tool, a log rod was used to manually press the SaltSmart™ sensors and dry pads against the metal surface. The dry sampling pads used for the canister tops varied from those used to sample the sides. The pads used to sample the tops of the containers were about 1.5 cm thick (with thinner sides to allow attachment to a steel back-plate), while those used to sample the sides were thinned to ~0.7 cm. Using the thinner pads allowed them to be recessed into the sampling tool, so that they did not contact the surface of the canister until the sampling tool was lowered into position through the narrow annulus and the pads extended pneumatically.

During sampling at Hope Creek and Diablo Canyon, the SaltSmart™ sensors and the abrasive sponges used to the dry dust sampling were always handled with gloves, and once mounted on the sampling tool, were enclosed in a plastic bag until the tool was inserted into the overpack. Upon retrieval from the overpack, a plastic bag was immediately placed over the sampling tool, and not removed until the scissor lift was lowered. At ground level, the plastic bag was removed, and the SaltSmart™ sensor or abrasive sponge was extracted from the sampling tool and immediately placed into a 50 ml screw-cap polypropylene centrifuge tube. The tubes containing the samples were then placed into a cooler with ice packs to limit degassing and microbial activity. Within a day or two of collection, the samples were shipped to SNL in the cooler, with fresh ice packs to keep them cool. Once at SNL, they were refrigerated until analysis. Table 1 and Table 2 list the samples that were received from Hope Creek and Diablo Canyon, respectively, and provide a short description of each. The SaltSmart™ sensors are referred to as wet samples, because the salts were leached off the storage canister surface by water passing through the wick. The abrasive pads collected dust without the aid of water, and are referred to as dry samples.

The samples were collected from two canisters at each site. At Hope Creek, these canisters were designated MPC-144 and MPC-145; at Diablo Canyon, they were MPC-123 and MPC-170. Upon delivery to Sandia, the samples were examined and a description was recorded. Additionally, when the SaltSmart™ samples were disassembled to extract the soluble salts, the condition of the wick and the reservoir pad was noted. Table 1 and Table 2 also list the sampling location and the canister surface temperature at the sampling location for each sample. Initially, all samples were given to Sandia without location information to ensure that the analyses were not biased, but during data interpretation, the canister surface locations and temperatures were provided. Samples were also collected from the gamma shields after removal, and a few blanks were included as unknowns. SNL was not informed of the identity of each sample until the analyses had been largely completed.

A few general observations can be made based on sample observations prior to analysis. First, for both the wet and dry samples, those collected from the flat tops of the canisters are more heavily coated with dust than those collected from the sides. This suggests that more dust was present on the tops of the canisters, but it should be remembered that a different collection method and thicker pads were used to collect the dry samples from the canister tops, and that may have contributed to the higher dust loads. Also, for the Hope Creek samples, the SaltSmart™ wicks are generally more lightly coated along the upstream (inlet) edge of the wick; sometimes, a clear dividing line is visible. This suggests that the sensors were not flat against the surface. This is consistent with the field observation that the water tube attached to the sensor inlet was thicker than the SaltSmart™ sensor, and when the sample holder was pneumatically extended to press the sample against the canister surface, the water line was pinched between the sample holder and the surface, preventing the SaltSmart™ from lying flat against the surface. In general, most of the wick surface (80-90%) appears to have contacted the canister; however, for SaltSmart^{TM} sample 145-006, only about 1/3 of the wick appears to have contacted the surface. When estimating the salt load per unit area, it is important to remember that the surface area sampled may be less than the area of the SaltSmart™ wick, especially for this sample. It is not clear that the Diablo Canyon SaltSmart™ samples had the same issue, as the dust coatings on these samples were generally too light to see. Finally, it is worth noting that windblown seeds of the marsh grass *Phragmites,* which is abundant around the site, were observed on the canister tops at Hope Creek, apparently having been blown in through the outlet vents. One of these seeds was captured on the pad for dry sample 145-012.

The surface temperatures at each sampling location are provided in Table 1and Table 2, and are plotted versus sample location in Figure 3and Figure 4 for the Hope Creek and Diablo Canyon canisters, respectively. It should be noted that in the case of Hope Creek MPC-144 and Diablo Canyon MPC-170, temperatures were not consistent over the course of the sampling effort, with measured temperatures for the wet and dry sampling forming two different trends as a function of depth. The observed temperature differences are too large to be due to variations in the external air temperature, and it is assumed that readings from one or more of the thermocouples are inaccurate; possibly, poor contact was achieved with the canister surface.

Testing by the manufacturer indicated that the maximum operating temperature for the SaltSmart™ sensors was 90ºC. The dry pads had a much higher maximum operating temperature. For this reason, thermocouple readings or dry pad samples were taken first, and the recorded temperatures used to determine what parts of the canisters could be sampled using the SaltSmart™ sensors. The Hope Creek canisters were sufficiently cool that the entire surface of each canister could be sampled, but the Diablo Canyon canisters were much hotter, and only the lower portion of the canister sides was sampled with the SaltSmart™ devices. The SaltSmart™ sensors actually began to operate poorly at temperatures ≥~80ºC; the wick would adhere to the silicone pressure pad backing it, and the reservoir pad would not be fully wetted, suggesting that water flow through the sensor may have been limited, and salt recovery may not have been complete. SaltSmart™ samples where the wick adhered to the pressure pad, or which did not have fully wetted reservoir pads, are also shown in Figure 3 and Figure 4.

Table 1. List of Hope Creek Samples.

Sample #	Sample Type	T (ºC)	Sample location	Description
Canister MPC-144				
144-001	Dry pad		Gamma shield, bottom of top section	Thin pad, slight brown discoloration on the surface.
144-002	Dry pad		Gamma shield, side of top section	Thin pad, no visible discoloration.
144-003	SaltSmart		Gamma shield, side of bottom section	No visible discoloration. During collection, appeared to be unsaturated.
144-004	SaltSmart		Gamma shield, side of bottom section	No visible discoloration.
144-005	Dry pad	28.9	Canister side. Insertion depth: 13.5 ft from upper edge	Thin pad, little or no discoloration.
144-006	Dry pad	32.0	Canister side. Insertion depth: 8.5 ft from upper edge	Thin pad, little or no discoloration.
144-007	Dry pad	52.4	Canister side. Insertion depth: 1.0 ft from upper edge	Thin pad, little or no discoloration.
144-008	SaltSmart	34	Canister side. Insertion depth: 13.0 ft from upper edge	No visible discoloration.
144-009	SaltSmart	46.9	Canister side. Insertion depth: 7.5 ft from upper edge	Slight brown discoloration on the wick; one large (a few mm) brown stain.
144-010	SaltSmart	56.6	Canister side. Insertion depth: 1.0 ft from upper edge	No visible discoloration.
144-011	Dry pad	55.9	Canister top. Insertion (horiz.): 40.5 in.	Thick pad, strongly discolored.
144-012	Dry pad	60.7	Canister top. Insertion (horiz.): 64.5 in.	Thick pad, slightly discolored.
144-013	SaltSmart	58.9	Canister top. Insertion (horiz.): 42.5 in.	Wick heavily coated with brown dust; upon disassembly, the absorbent pad was also discolored
144-014	SaltSmart	60.7	Canister top. Insertion (horiz.): 58.5 in.	Wick discolored—some grains coarse enough to be seen by eye.
Canister MPC-145				
145-001	Dry pad		Gamma shield	Thin pad, no visible discoloration.
145-002	SaltSmart		Gamma shield	No visible discoloration.
145-003	Dry pad	21.6	Canister side. Insertion depth: 13.5 ft from upper edge	Thin pad, no visible discoloration.
145-004	Dry pad	34.1	Canister side Insertion depth: 8.5 ft from upper edge	Thin pad, no visible discoloration.
145-005	Dry pad	50.3	Canister side Insertion depth: 1.5 ft from upper edge	Thin pad, slight brown discoloration.
145-006	SaltSmart	21.4	Canister side. Insertion depth: 13 ft from upper edge	Wick shows slight discoloration in a band at one end (~1/3 of the pad). It appears that the sensor was tilted, and the wick was only partially in contact with the surface. Pad was nearly dry upon disassembly.
145-007	SaltSmart	38.2	Canister side. Insertion depth: 7.5 ft from upper edge	Wick shows no discoloration.
145-011	SaltSmart		Blank	Wick shows no discoloration. Upon disassembly, pad was not saturated.
145-012	Dry pad	77.8	Canister top. Insertion (horiz.): 64.5 in.	Thick pad, heavy discoloration, a small seed was adhering to one edge of the pad.
145-013	SaltSmart	78.9	Canister top. Insertion (horiz.): 58.5 in.	Wick heavily discolored with brown dust. Upon disassembly, the pad was not saturated.
145-014	SaltSmart	54.6	Canister side. Insertion depth: 1.0 ft from upper edge	No visible discoloration.

Table 2. List of Diablo Canyon Samples.

Sample #	Sample Type	T (°C)	Sample location	Description
Canister MPC-123				
123-001	Dry pad		Gamma shield	Thin pad, no visible discoloration.
123-002	SaltSmart		Gamma shield	No visible discoloration.
123-003	SaltSmart	48.7	Canister side. Insertion depth: 14 ft from upper edge	No visible discoloration. One black speck visible with hand lens.
123-004	SaltSmart	78.6	Canister side. Insertion depth: 11.5 ft from upper edge	No visible discoloration. A few black specks visible with hand lens.
123-005	SaltSmart	86.1	Canister side. Insertion depth: 10.5 ft from upper edge	No visible discoloration. A few black specks visible with hand lens. Note: Wick adhered to silicone pressure pad, reservoir pad only partially wetted.
123-006	Dry pad	80.7	Canister side. Insertion depth: 11 ft from upper edge	Thin pad, minor discoloration along two edges of pad.
123-007	Dry pad		Blank (removed form tool after failed attempt to enter annulus).	Thin pad, no visible discoloration.
123-008	Dry pad	99.8	Canister side. Insertion depth: 7.5 ft from upper edge	Thin pad, moderately discolored.
123-009	Dry pad	118.6	Canister side. Insertion depth: 3.0 ft from upper edge	Thin pad, slight discoloration in one corner.
123-010	SaltSmart		Blank	No visible discoloration.
123-011	Dry pad	97.1	Canister top (center). Insertion (horiz.): 64.5 in.	Thick pad, slightly discolored, with visible black specks.
123-012	Dry pad	95.6	Canister top (7” from closure ring). Insertion (horiz.): 7 in.	Thick pad, moderately discolored, with visible black specks.
Canister MPC-170				
170-001	Dry pad		Gamma shield	Thick pad, no visible discoloration.
170-002	SaltSmart		Gamma shield	No visible discoloration.
170-003	Dry pad	86.4	Canister top (center). Insertion (horiz.): 64.5 in.	Thick pad, somewhat discolored
170-004	Dry pad	67.7	Canister side. Insertion depth: 11 ft from upper edge	Thin pad, slightly discolored.
170-005	Dry pad	89.9	Canister side. Insertion depth: 7.5 ft from upper edge	Thin pad, discolored along one edge.
170-006	Dry pad	82.6	Canister side. Insertion depth: 3.0 ft from upper edge	Thin pad, slightly discolored along two edges.
170-007	SaltSmart	80.8	Canister side. Insertion depth: 10.5 ft from upper edge	No visible discoloration. A few black specks visible with hand lens. Note: Wick adhered to silicone pressure pad, reservoir pad only slightly damp.
170-008	SaltSmart	83.8	Canister side. Insertion depth: 9.5 ft from upper edge	No visible discoloration. Black specks visible to naked eye and with hand lens. Note: Wick adhered to silicone pressure pad, reservoir pad only partially wetted.
170-009	SaltSmart	86.8	Canister side. Insertion depth: 9.0 ft from upper edge	No visible discoloration. Black specks visible to naked eye and with hand lens. Note: Wick adhered badly to silicone pressure pad, but reservoir pad well wetted.

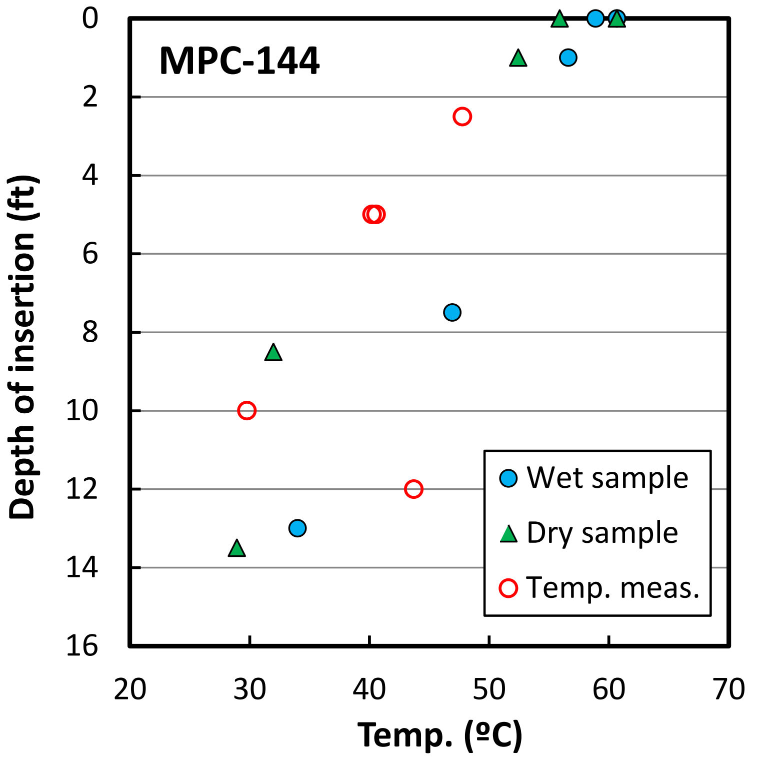

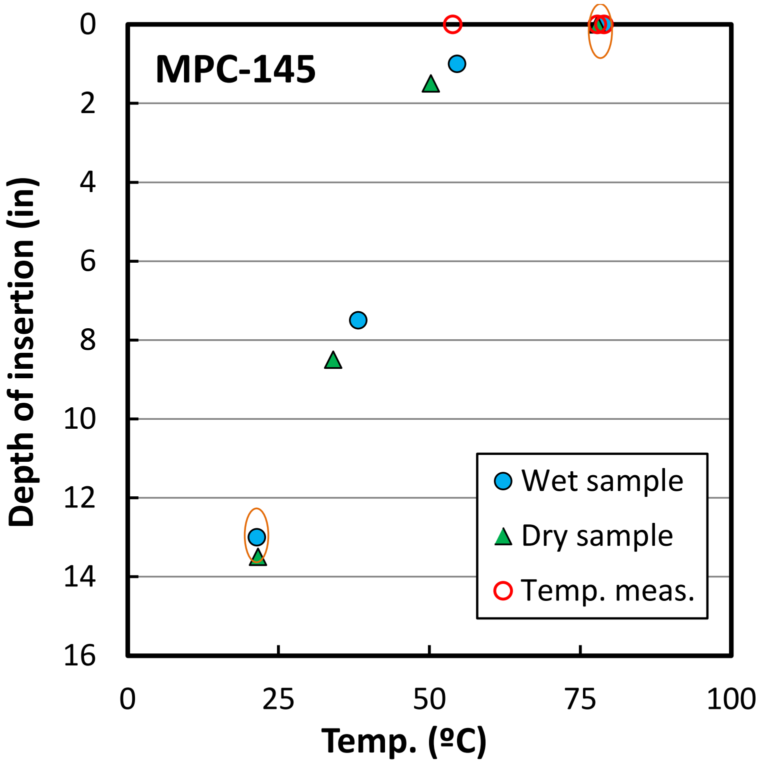

Figure 3. Hope Creek sample locations and temperatures. Orange ovals mark SaltSmart™ samples with heat-damaged wicks or unsaturated reservoir pads.

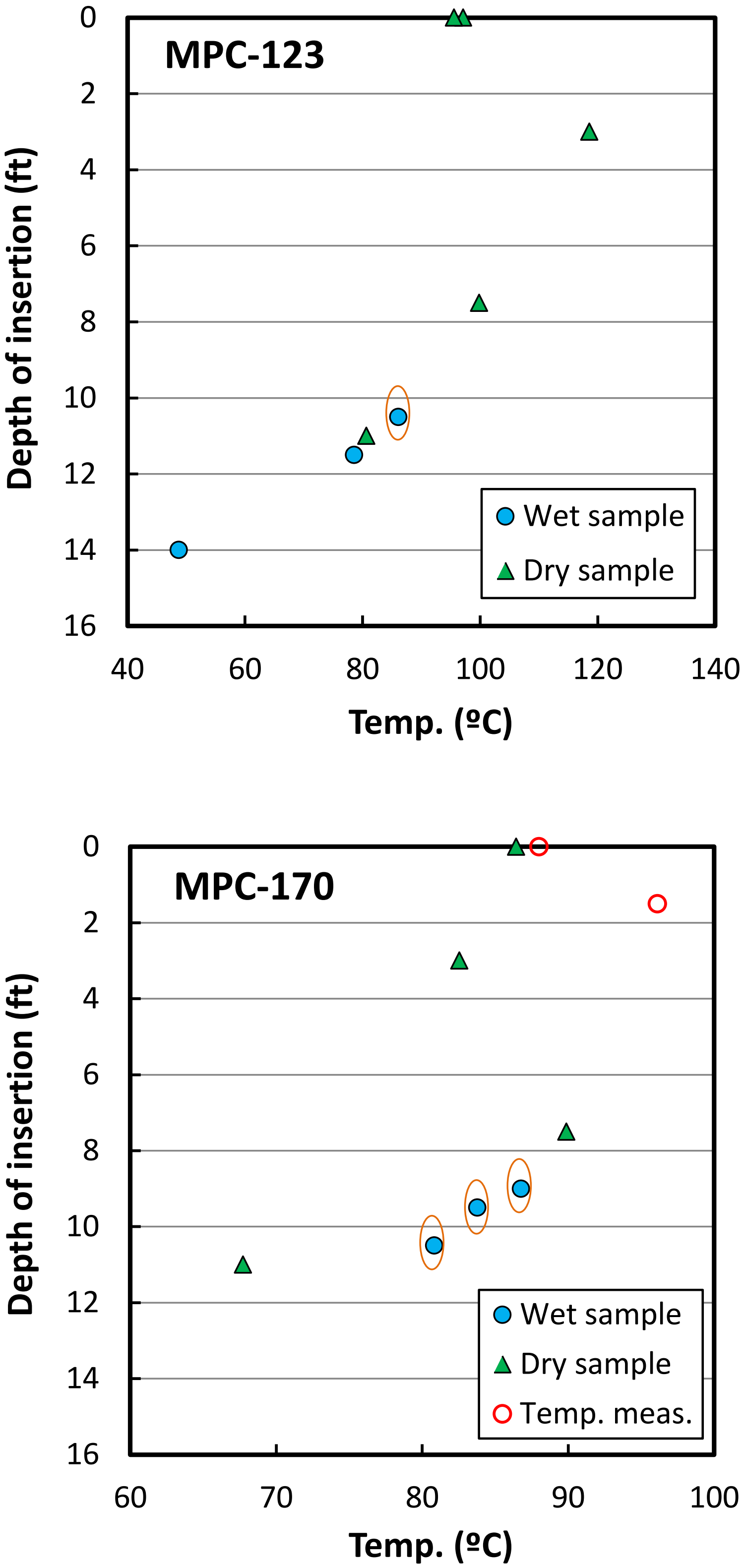

Figure 4. Diablo Canyon sample locations and temperatures. Orange ovals mark SaltSmart™ samples with heat-damaged wicks or unsaturated reservoir pads.

2.3 Methods

2.3.1 SEM Imaging and EDS Analysis

SEM/EDS analysis of the dry dust samples provides textural and mineralogical information of dust/dust components, and allows visual identification of organic matter (floral/faunal fragments). Sample fractions retained for SEM analysis were plasma-coated with gold to reduce sample charging during analysis. Imaging and element mapping was done with a Carl Zeiss Supra™ 55VP SEM, equipped with an Oxford X-Max EDS detector and Aztec© software. An accelerating voltage of 15 keV was used, and working distances of 7.1 to 9.4 mm, with varying degrees of magnification. Images were obtained using both secondary and backscattered electron imaging. A relatively high beam current was used to produce a high count rate and facilitate rapid element mapping. However, the elevated beam current did enhance sample charging for the fibrous pad samples, resulting lower image quality in some cases.

2.3.2 XRF Analysis

Due to an equipment failure at Sandia, the XRF mapping was accomplished at Los Alamos National Laboratories, using an EDAX Eagle Micro-XRF system, instead of the Bruker M4 Tornado micro-XRF system used for analysis of Calvert Cliffs samples. This energy dispersive system was equipped with a micro-focus Rhodium X-ray source operated at 40 keV and 200 µA. The spatial resolution was ~100 µm. Mapping was performed via an XY translation stage. Samples were run under vacuum atmosphere ($5x10^{-3}$ Torr). The summed X-ray spectrum was processed to produce a semi-quantitative chemical analysis for the abrasive pad and the dust on the sample surface. The XRF analysis provides element ratios which, in combination with the wet chemical analysis, can be used in mass balance and normative mineral calculations. However, one limitation is that elements lighter than sodium (e.g. oxygen, nitrogen, carbon) cannot be detected, and detection limits for sodium are poor.

2.3.3 XRD Analysis

XRD analysis was performed using a Bruker D2 Phaser diffractometer with a Cu Kα X-ray source, and a LynxEye solid-state energy discriminating X-ray detector. Samples were analyzed “as-received,” with minimal preparation, directly on the abrasive pads. However, the abrasive pads were too coarsely porous to allow in-situ XRD analysis, and no mineral peaks were identified. An additional attempt was made to analyze the insoluble residue remaining after washing the soluble salts from the dry pads and filtering the residue onto Whatman 541 paper filters. This, too, was largely unsuccessful—only a single peak, the most prominent peak for quartz, and a few small possibly corresponding to talc were identifiable. The XRD analysis will not be discussed further here.

2.3.4 Chemical Analysis

2.3.4.1 SaltSmart™ sensors — soluble salts

Once at Sandia, the SaltSmart™ sensors were disassembled and the soluble salts were extracted with DI water for chemical analysis. Then the salt compositions, including chloride concentration, were measured directly by inductively-coupled plasma optical emission spectroscopy (ICP-OES), and cation/anion ion chromatography (IC).

For analysis, the SaltSmart™ sensors were removed from the 50 ml centrifuge tubes and split open along the seam with a small chisel. The component parts of each sensor are shown in Figure 5. The wick and the reservoir pad inside the SaltSmart™ device were removed and transferred to a pre-weighed 50 ml polypropylene screw-cap sample tube. Moisture was observed on other plastic internal pieces of the sensors and on the inside surfaces of the two halves of the shell. The internal pieces, and the inside surfaces of the shells, were rinsed with deionized water (>18MΩ) and the water transferred to the polypropylene sample tubes containing the wicks and pads. The original centrifuge tubes used for shipping the samples commonly contained condensate, and these were also rinsed into the polypropylene sample tubes. Additional DI water was added, to achieve a total water volume of ~15 ml per sample; the exact volume was determined by the weight difference between the empty and filled vials; the weights of a dry wick and reservoir pad were also considered. The samples were placed on a shaker table overnight to leach the salts in the wick and pad into the solution.

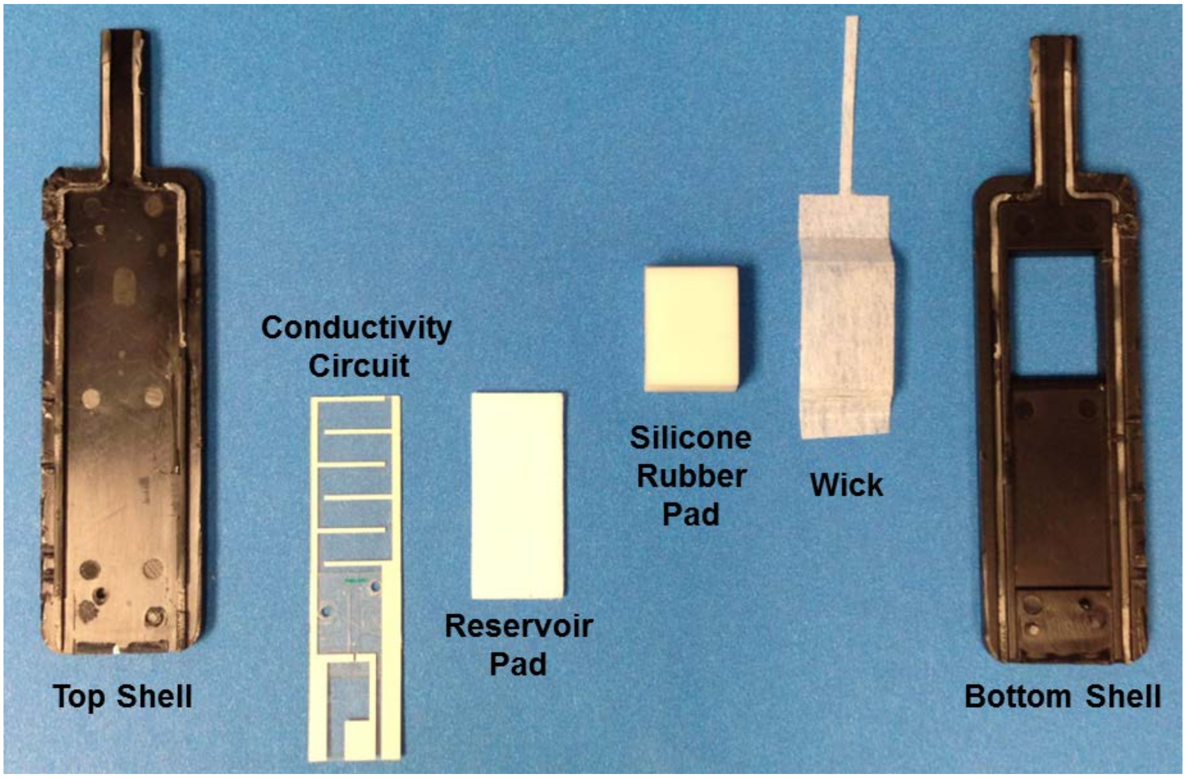

Figure 5. Disassembled SaltSmart^{TM} Device.

Also during disassembly, the condition of the wick and the saturation state of the reservoir pad were recorded. During normal operation of the sensor, the reservoir pads inside the sensors are completely saturated after use, indicating that water flow was adequate through the sensor. This was confirmed by ambient-temperature testing of SaltSmart™ sensors at Sandia. Testing at Sandia using metal coupons with known deposited salt loadings showed that SaltSmart™ sensors are efficient at removing soluble salts from metal surfaces, and that the disassembly and leaching procedure used on the Hope Creek and Diablo Canyon samples is effective (Memo from C. Bryan to L. Zsidai dated Nov. 13, 2013; SAND#2013-9948P); experimental salt recoveries were in the 80-100% range.

Although testing by the SaltSmart™ company suggested that the sensors performed adequately to ~90ºC, the condition of the Hope Creek and Diablo Canyon samples indicated that the operational limit for SaltSmart™ sensors is lower. During sample disassembly, it was observed that the reservoir pad was saturated in most of the relatively low-temperature Hope Creek samples, but that that the wicks adhered strongly to the silicon pressure pad for samples collected at temperatures of ~80ºC and above; in nearly all of those cases, the reservoir pad was not saturated. Wick adherence and/or poor reservoir pad saturation was observed for three of the Hope Creek samples and for most of the Diablo Canyon samples (See Figure 3 and Figure 4). In only one instance was poor wetting associated with a lower-temperature sample (sample 145-006); in this case, it appears to be associated with poor contact between the wick and canister surface. It is possible, perhaps likely, that salt removal was incomplete for SaltSmart™ samples that were poorly wetted, as the adherence of the wick to the silicone pressure pad and the incomplete saturation of the reservoir pad suggest that water transport through the wick was limited.

Following equilibration, aliquots of each sample were separated for analysis. Approximately 8 ml of the solution (the actual amount was determined by weight) was extracted from the sample tubes and retained for cation analysis. This fluid was spiked to contain 2% Optima-grade HNO_3 and 1 mg/L Sc as an internal standard, and brought to a volume of 12 ml for analysis by inductively coupled plasma optical emission spectroscopy (ICP-OES). ICP-OES analyses were done using a sequential Perkin-Elmer Optima 8000 ICP-OES, in both axial and radial viewing modes. Analytes examined were Ca^{2+}, Mg^{2+}, Na^+, and K^+. A minimum of two wavelengths were evaluated for each element; collected spectra were evaluated for interfering peaks, and for each element, the wavelength was chosen that best reproduced known standard concentrations when the standards were analyzed as unknowns. Concentrations were estimated using integrated peak areas. Because the range of concentrations in the samples was unknown, five to six standards were made by diluting Spex Certiprep™ Assurance and Claritas-Grade ICP stock solutions and were run with the samples. Sample concentrations were estimated using a subset of the standards (never less than three and a blank), excluding those which were higher than necessary to constrain the sample concentration. This was done because the calibration curves were based on the least squares method, which over-weights higher-concentration standards and results in larger errors for values in the lower part of the range.

Three ml of the solution was extracted from the sample tubes and retained for anion analysis by ion chromatography (IC). Anionic analytes were F^-, Cl^-, Br^-, NO_2^-, NO_3^-, SO_4^{-2}, and PO_4^{-3}; however, Br^- and NO_2^- were never detected, and are not included here. IC analyses were done with a Dionex ICS-1100 RFIC Ion chromatograph with a Dionex Ionpac AS-23 RFIC column and AG-23 guard column, and a Dionex AERS 500 suppressor. Blanks were run every two-three samples to assess carryover, but little was observed. As with the cation analyses, five to six standards and a blank were made by dilution of stock Dionex IC anion standards, but only a bounding subset was used to estimate sample concentrations.

Finally, three ml of the solution was acidified to 0.1% HNO_3 and retained for analysis of ammonium, $(NH)_4^+$. Unlike other cationic components of the salts, ammonium cannot be measured by ICP-OES. The analyses were done with a Dionex ICS-1100 RFIC Ion chromatograph with a Dionex Ionpac CS-12A column and CG-12A guard column, and a CSRS 300 suppressor, all 4 mm in diameter. The standards were made by dilution of stock Dionex IC cation standards.

2.3.4.2 Dry pads — soluble salts

Following analysis of the whole pad by Micro-XRF, the pad samples were removed from the steel plates and sectioned. About ¼ of each pad was retained for SEM/EDS analysis, while the rest was used for chemical analysis of soluble salts. The remainder of each sample was placed in a pre-weighed polypropylene sample vial, and the vials were reweighed to determine the pad weight (to allow for accurate blank correction later). Then, 10 ml of cold deionized water was added to each vial, and each vial was reweighed to determine the exact liquid mass present. The samples were agitated for two hours on a shaker table, and the pads were removed from the vials and transferred to filter funnels containing pre-rinsed Whatman #541 paper. The leachate containing the soluble salts transferred to a syringe, filtered through 0.2 µm polyethersulfone syringe filters, and split into three aliquots for chemical analysis (ICP-OES cations, IC anions, and IC ammonia) as described previously for the SaltSmart™ samples. Any sediment remaining in the vials after transferring the leachate was added to the pad samples in the filter funnels.

The pads and sediment in the filter funnels were rinsed thoroughly with ~40 ml DI water, making an effort to dislodge any particles on the pads. Then, then the pads were extracted from the filters and discarded. The paper filters with the remaining insoluble residues were then dried. An attempt was made to analyze them by XRD, but little was observed—the X-ray pattern from the nylon in the pad dominated the spectrum. A very small peak was tentatively identified as the dominant peak for quartz was present in the patterns of the more heavily loaded canister top samples. In one sample, a few small peaks that may represent talc, used as filler in the resin in the pads, were also observed. Because of the very light dust load on most pads, and the high degree of contamination by talc, a decision was made not to perform bulk analyses of the dry pad insoluble residues.

2.4 Results

2.4.1 SEM/EDS Analysis

SEM/EDS analysis of the dry pad samples was carried out to determine dust and salt mineralogy, to identify organic materials present, and to determine dust particle size and morphology. Analyzed samples include a blank pad and pads from both Hope Creek and Diablo Canyon (Table 1 and Table 2). SEM images were taken of characteristic features, and EDS element mapping was done to assess mineralogy. Results are summarized here with typical images from some samples; a complete suite of analyses is provided in Appendix A, and allows the reader to better assess the representativeness of the results provided here.

2.4.1.1 Blanks

The sponge-like pads used to collect the dry dust samples were 3M Scotch-Brite™ light-duty scrubbing pads (part # 3M-05683). The pad consists of nylon fibers bound together with a resin. The pads were purchased after consultation with 3M, and were intended not to contain any mineral components. However, after using the pads, it was determined that talc (Mg-silicate) is present as filler in the resin binding the pads together. The pads are easily abraded, and when this occurs, the talc, which has perfect basal cleavage, flakes apart, generating particulate material, which interfered with analysis of dust collected from the storage canisters. Although this was a problem, the simple chemical composition of talc ($Mg_3Si_4O_{10}(OH)_2$) meant that it was in general possible to distinguish it from the dust adhering to the canisters, and to identify the dust species.

Figure 6 is a low-magnification image of the blank pad. The fibers form a network, and the resin-filler binds the mass together, forming broad bridges at fiber intersections. The talc is generally embedded within the resin, and does not penetrate the exposed surface, except where the resin has been abraded. The bridges are ideal locations for analysis of adhering dust, because the talc is embedded within the resin, particulate talc contamination is commonly minimal, and the broad flat surface is ideal for SEM analysis. However, in cases where the sampled dust load is light, the adhering dust may be mostly on the exposed uppermost surfaces of the pads, where abrasion has revealed the talc. In these cases, much of the particulate matter on the pads may be talc flakes. In addition to Mg, Si, and O in the talc, the nylon is an amide, containing carbon (C), nitrogen (N), and oxygen (O), and these species are reflected in the EDS spectrum and the element maps. The dominant chemical components in the pad, as identified by EDS, are C, Si, and Mg; N is obscured by proximity to the C peak, but shows up in the element maps. Other chemical components that leach from the pad during chemical analysis include sodium (Na), phosphate (containing phosphorous, P), and sulfate (containing sulfur, S); however, these contribute too little to the bulk composition to be identified by SEM/EDS analysis.

Figure 7 is a higher resolution image of the bad blank, showing the texture of the pad and the embedded talc. In general, the blank pad had little adhering particulate matter, other than talc particles freed by abrasion during cutting and handling of the pad for SEM analysis.

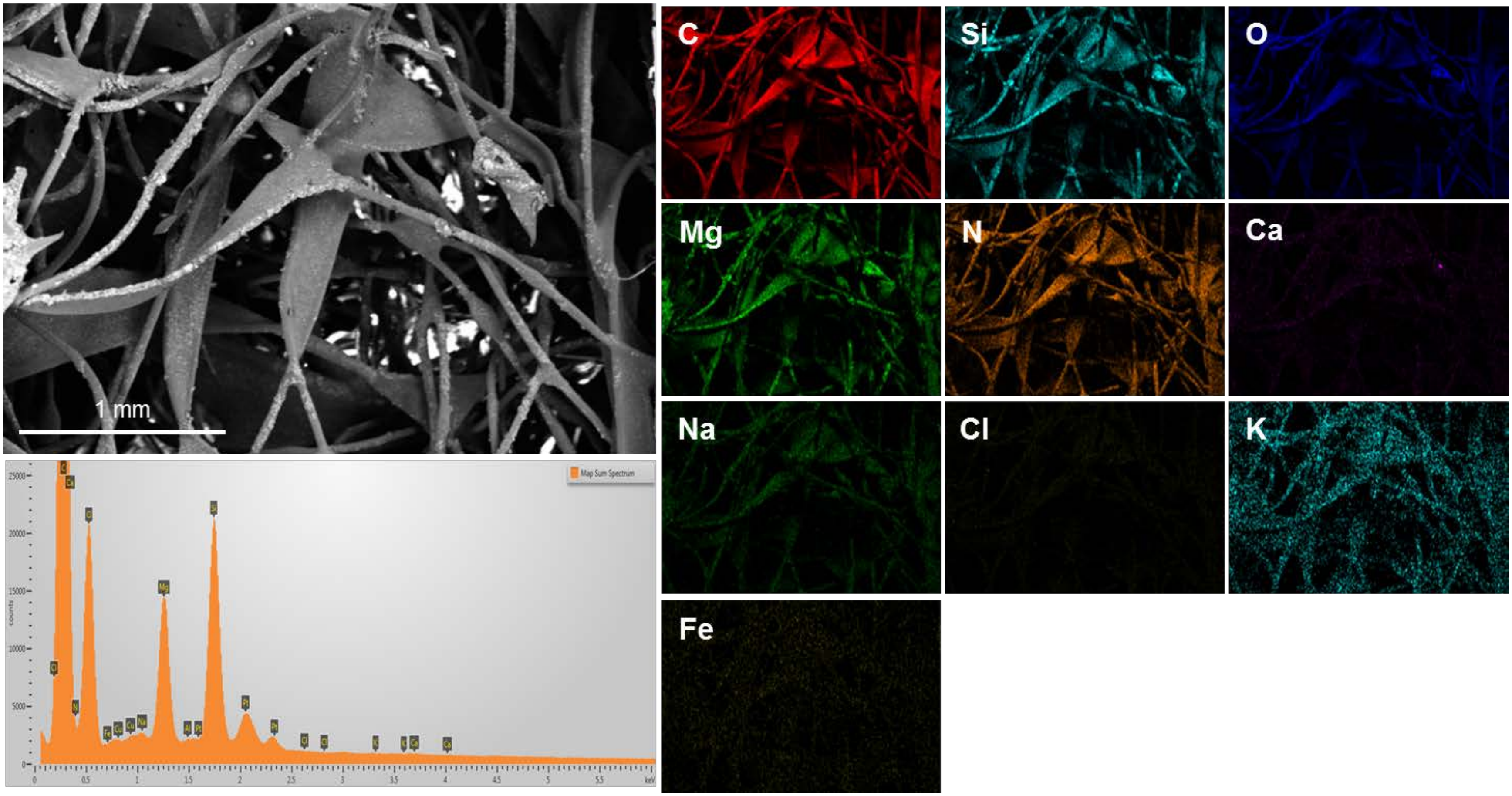

Figure 6. Low magnification SEM image/EDS map of Scotch-Brite™ pad blank.

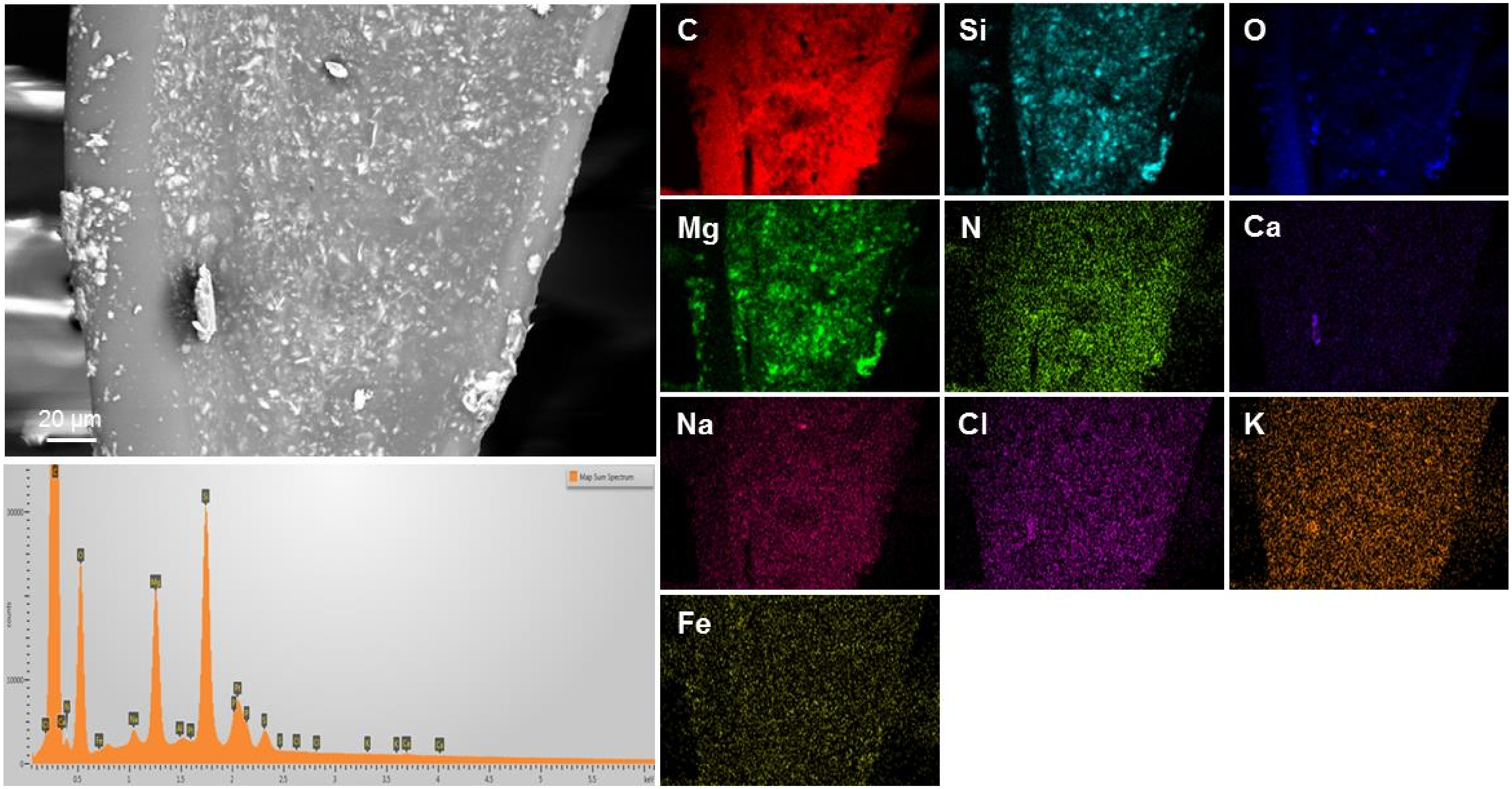

Figure 7. High magnification SEM image/EDS map of Scotch-Brite™ pad blank.

2.4.1.2 Hope Creek Samples

Two canisters were sampled at the Hope Creek ISFSI. These were designated MPC-144 and MPC-145. For this study, the complete suite of samples was analyzed only for canister MPC-145. To verify that mineralogy did not vary significantly from canister to canister, two samples from MPC-144 were analyzed—the lowermost sample collected from the canister side, and a sample from the canister top. For each canister, a few representative SEM image/EDS element map combinations are discussed here; a complete suite of analyses is provided in Bryan and Enos (2014). It should be noted that for some of the samples from the canister sides, dust was so sparse that only a few sites on each pad had any adhering dust at all. For very lightly loaded samples, the SEM images are not typical of the pad surface; the images represent locations where concentrations of dust particles are present, and hence provide an overestimation of the typical dust loading.

MPC-145. Canister MPC-145, for which a complete suite of samples were analyzed, will be discussed first. Samples 145-003, 145-004, and 145-005 were collected from the canister side at distances, respectively, of 13.5, 8.5, and 1.5 feet below the upper edge of the canister. Sample #145-012 was collected from the top of the canister, near the center. Dust and salt loads on pads used to sample the sides of the canister were extremely light. However, the flat top of the canister had large amounts of dust, and much adhered to the sampling pad. There is no significant variation in the mineralogy present from place to place on the canister surface. The phases observed on all of the samples from MPC-145 are listed in Table 3. Most of the dust consists of terrestrially-derived detrital mineral grains, including quartz (Si-O), and several different aluminosilicates (phases containing Si, Al, O and usually, other elements). The aluminosilicates include blocky, angular Na, K, and Ca bearing phases that appear to be feldspars, platy biotite flakes, and aggregate grains of finer particles that are likely to be clays. Angular Fe and Fe-Cr particles in various stages of oxidation are steel and stainless steel particles generated during manufacturing of the canisters; spherical particles of the same compositions may be welding spatter. The only common soluble salt is a Ca-SO_4 phase (gypsum or anhydrite); chloride occurs mostly as rare small particles of NaCl.

Sample 145-003 was collected at a distance of 13.5 feet below the upper edge of the canister. SEM/EDS data for this sample (Figure 8) show an accumulation of dust, mostly aluminosilicates and Fe-Cr particles, near an abraded edge—note that many of the particles in the image are talc released from the pad by abrasion. On very lightly loaded pads, dust was commonly only present on or near abraded areas. Also, on lightly loaded pads, Fe-Cr particles formed a larger proportion of the total, because the amount of environmentally-derived dust (relative to manufacturing-derived particles) was low. A single grain of NaCl is present in the image.

Sample #145-004, collected 8.5 feet below the top of the canister, was very similar. Dust particles were very sparse, and most particulate material was talc, freed by abrasion from the pad. Adhering particles were sparse and generally small, less than 5 microns in diameter. The dominant dust phases include quartz, aluminosilicates, 304SS particles, and Ca-SO_4. Sample 145-005 was collected 1.5 feet below the upper edge of the canister, and once again, the pad was very lightly loaded; adhering dust was largely restricted to topographically high regions on the pad, which had been abraded by contact with the canister surface. Only one location on the pad has significant dust, and it consisted largely of fine particles of stainless steel embedded in the resin, and two large dust grains of biotite, and a Na-Zn phase. The Na-Zn phase is apparently from the corrosion-inhibiting Zn-rich paint on the outer surface of the canister overpack. Similar Zn-Na rich grains were seen on the other cask from Hope Creek, and on a canister at Diablo Canyon.

Samples from the tops of the canisters at Hope Creek, such as 145-012, were heavily coated with dust (Figure 9). Canister top samples are invariably more heavily coated than canister side samples, and it is likely that this reflects a higher salt load on the canister top. However, it is important to remember that a different sampling technique was used for the canister tops—sampling by hand using a long rod, rather than the remote, pneumatically-operated sampler used for the canister sides. A larger area was probably sampled, and the pressure on the pad certainly varied for the two methods. It is likely that the dust removal efficiency varies between the two methods, and this may be responsible for some of the observed differences in dust loading on the sample pads.

A typical SEM/EDS map for sample 145-012 is shown in Figure 10. In this map, and at other locations on the sample pad, quartz and aluminosilicates are the dominant phases. The aluminosilicates are mostly biotite and blocky mineral fragments that are probably feldspars. Ca and Ca-Mg carbonates are also common. Soluble salts at this sample location include sparse NaCl and Ca-SO_4.

Table 3. Minerals Observed in Dry Pad Samples from MPC-145

Elemental analysis	**Morphology**	**Interpretation**	**Abundance**
Si-O	Angular grains	Quartz fragments	Common to abundant
K-Al-Si-O	Blocky, angular fragments	Potassium feldspar	Common
Na(±Ca)-Al-Si-O	Blocky, angular fragments	Sodic plagioclase	Common
Ca(±Na)-Al-Si-O	Blocky, angular fragments	Calcic plagioclase	Rare
Na-K-Al-Si-O	Blocky, angular fragments	Volcanic alkali feldspar or zeolite?	Rare
Ca-K-Na-Al-Si-O	Blocky, angular fragments	Zeolite?	Sparse
K-Fe-Mg-Al-Si-O	Large planar flakes	Biotite	Rare-common
Al-Si-O	Aggregate grains	Kaolinite	Rare
Fe-Cr	Striated flakes and fragments	Stainless steel particles generated by machining	Abundant
(K,Na,Ca)-Fe-Al-Si-O	Aggregate grains	Clays?	Common
Ca-Al-Si-O	Aggregate grains	Clays?	Rare
Ca-O-(C?)	Angular grains	Calcium carbonate	Common
Mg-O-(C?)	Angular grains	Magnesium carbonate	Rare
Mg-Ca-O-(C?)	Angular grains	Magnesium-calcium carbonate	Common
Na-Zn-O	Rounded particles	Particles from Zr-rich paint on the outside of the overpack?	Rare
C	Oval to spherical grains	Pollen	Rare to common
Fe-O	Angular particles	Iron oxides	Rare
Ca-S-O	Very fine particles	Gypsum	Rare to common
Na-Cl	Cubes and aggregates, commonly etched or corroded	Halite	Sparse
Na-K-Cl	Aggregate grains	Sylvite/halite aggregate?	Rare
C-Cl	Aggregate grains	Chloride-rich organic material?	Rare
Na-K-S-O	Aggregate grains	Aggregate of sulfates?	Rare

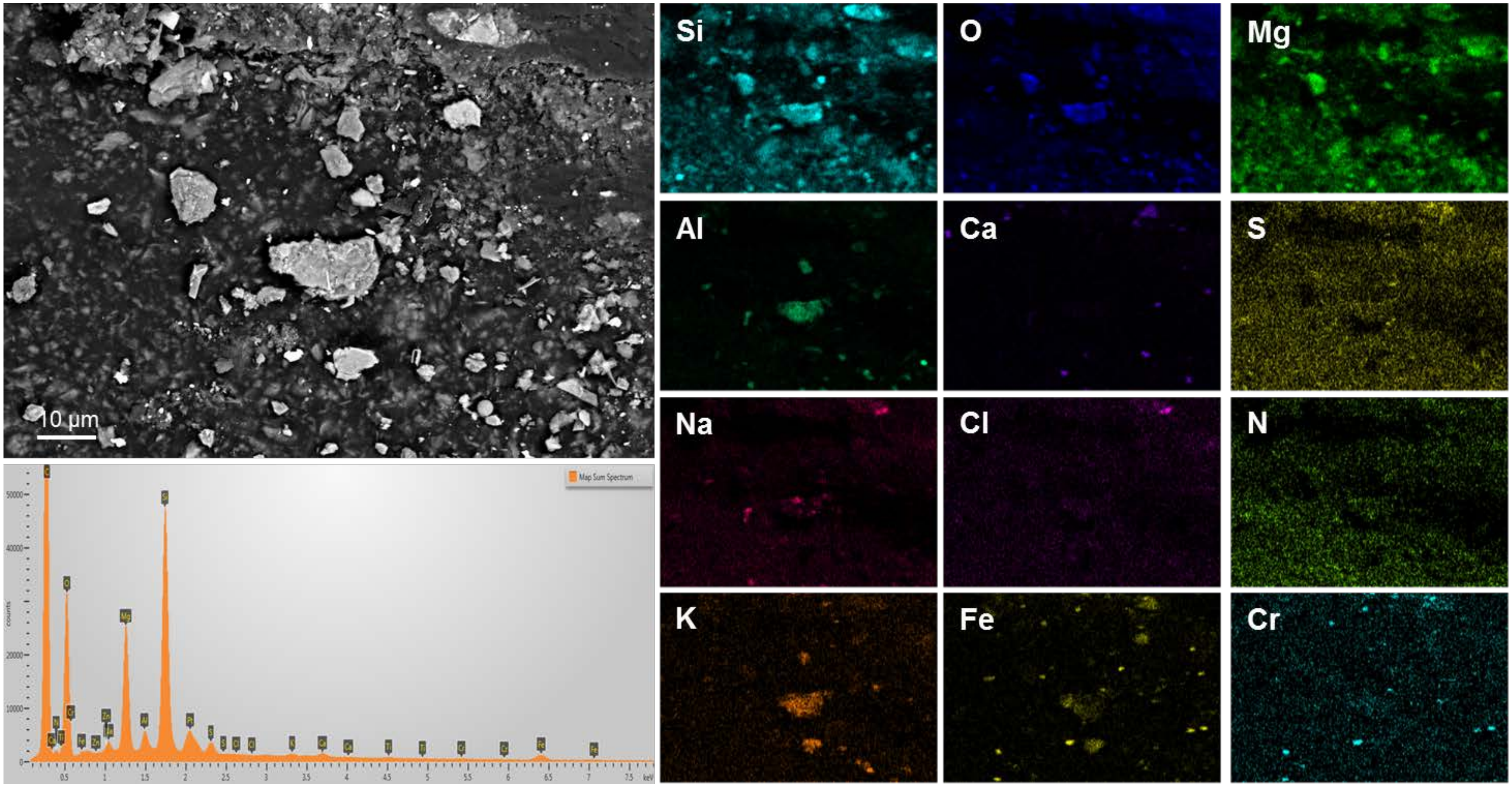

Figure 8. SEM image/EDS map (#2) of Sample 145-003, collected from the canister side, 13.5 feet below the upper edge.

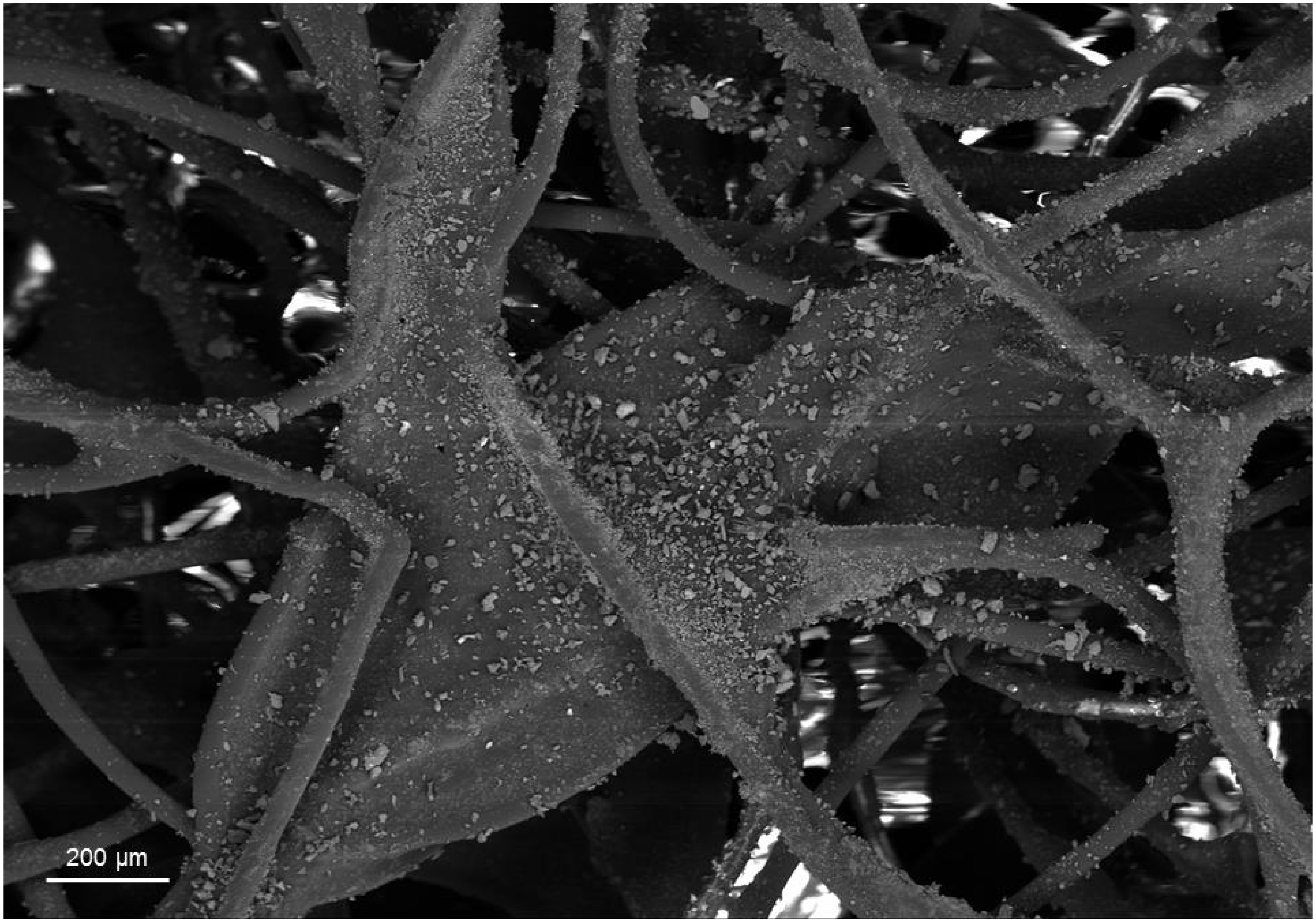

Figure 9. SEM image of sample 145-012, collected from the canister top, showing the heavy dust load.

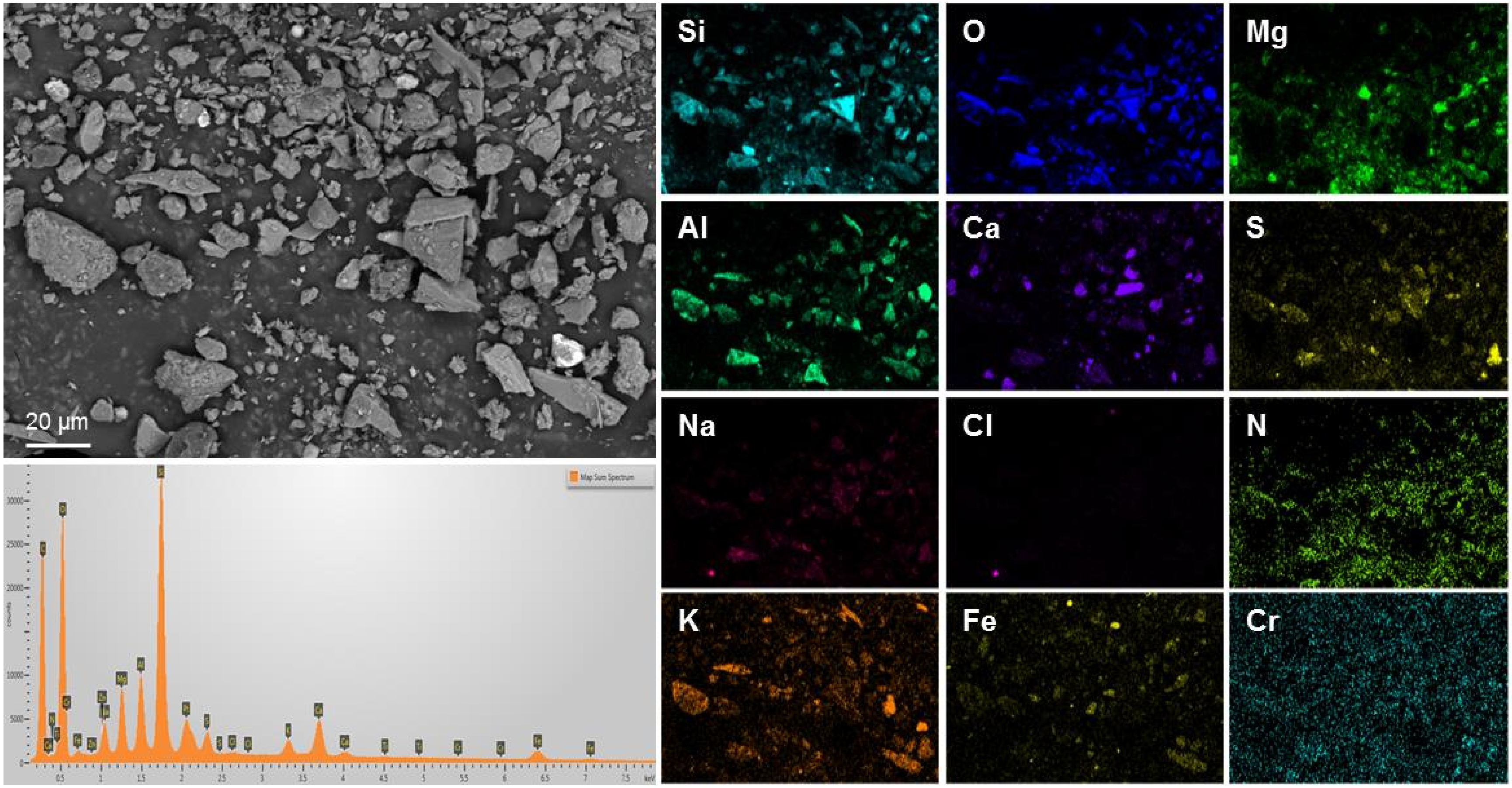

Figure 10. SEM image/EDS map of sample 145-012, collected from the canister top.

MPC-144. Results for MPC-144 were very similar to those for MPC-143. Phases observed during SEM analysis of samples from MPC-144 are listed in Table 4. Sample 144-005 was collected from the side of the canister, at a depth of 13.5 feet from the upper edge. The dust load on the pad was very light, and dust was largely restricted to areas where clear abrasion of the pad was present. SEM/EDS data for Sample 144-005 are shown in Figure 11 and Figure 12. Observed phases in sample 144-005 include coarse blocky grains K and Na feldspars, quartz grains, particles of 304SS; and sparse NaCl particles (note that a shadow partially obscures the element maps in Figure 12, strongly affecting the maps the lighter elements such as Na; the Cl-rich grains in this figure are all NaCl). Ca-carbonate was also commonly observed. Sample 144-011 was collected from the canister top, and copious amounts of dust adhered to the pad. An SEM/EDS map is shown in Figure 13. The dominant dust phases are identical to those in 144-005—quatrz and aluminosilicates, and Ca-carbonate. In other images of this sample, pollen grains were common, and rare salt particles of NaCl and Ca-SO_4 were observed; a single Zn-Na grain was present; the source of which was probably the Zn-rich anticorrosive paint on the exterior of the overpack.

Table 4. Minerals Observed in Dry Pad Samples from MPC-144

Elemental analysis	**Morphology**	**Interpretation**	**Abundance**
Si-O	Angular grains	Quartz fragments	Abundant
K-Al-Si-O	Blocky, angular fragments	Potassium feldspar	Abundant
Na-Al-Si-O-Ca	Blocky, angular fragments	Sodic plagioclase	Abundant
Ca-Al-Si-O	Blocky, angular fragments	Calcic plagioclase (?)	Rare
K-(Mg?)-Al-Si-O	Large flat flakes	Muscovite	Abundant
K-Fe-Mg-Al-Si-O	Large planar flakes	Biotite	Common-Abundant
Fe-Cr	Striated flakes and fragments	Stainless steel particles generated by machining	Abundant
Fe-Mg-Al-Si-O	Aggregate grains	Clays?	Common
Ca-Al-Si-O	Aggregate grains	Clays?	Rare-common
Mg-Al-Si-O	Aggregate grains	Clays?	Rare-common
Ca-O-(C?)	Angular grains	Calcium carbonate	Common
Na-Zn-O	Rounded particles	Particles of Zn-rich paint from the outside of the overpack?	Rare
C	Oval to spherical grains	Pollen	Rare-common
Fe-O	Isolated spheres, some hollow	Fly ash?	Rare-common
Ca-S-O	Very fine particles	Gypsum	Rare
Na-Cl	Cubes and aggregates, commonly etched or corroded	Halite	Sparse

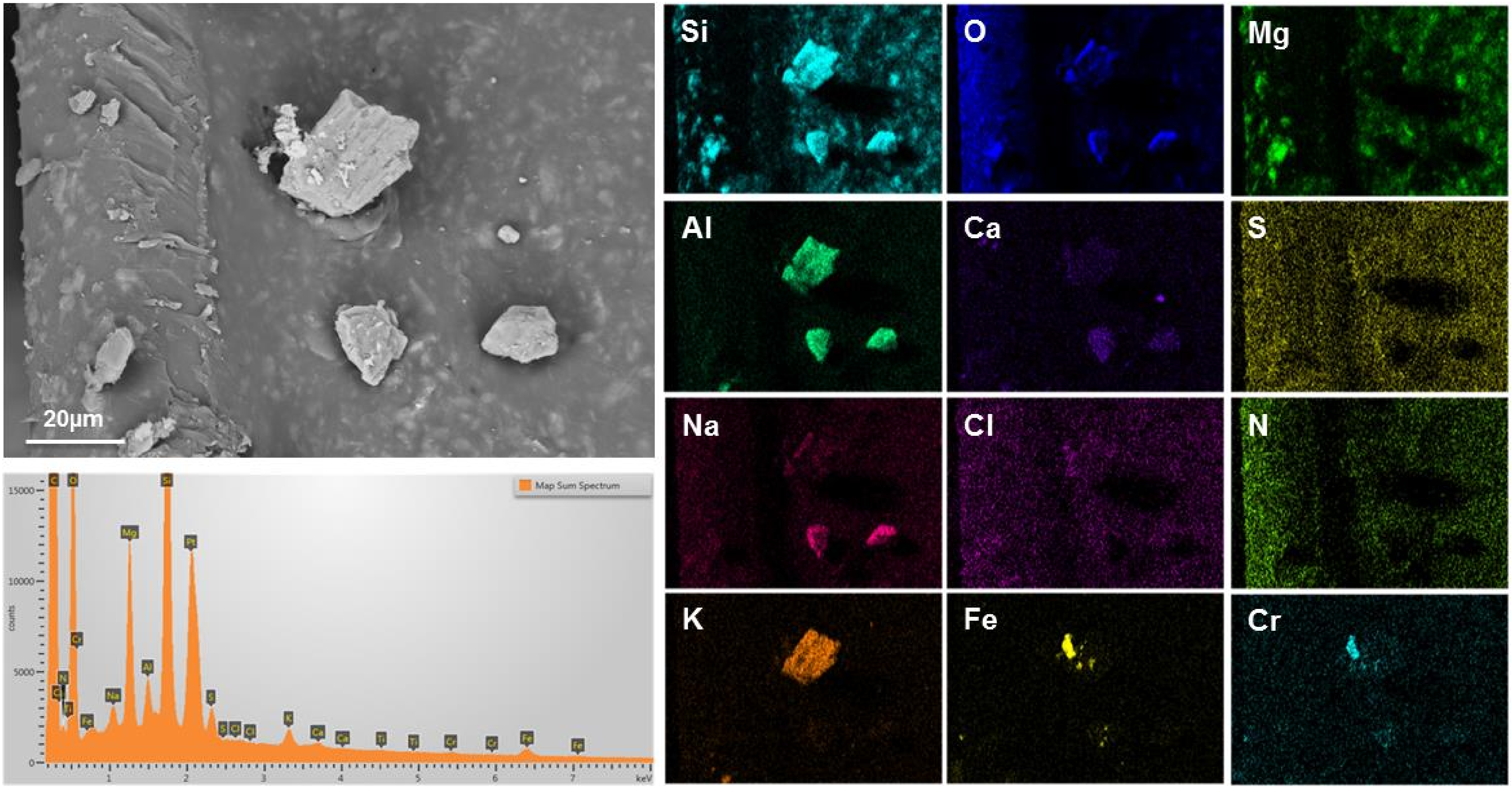

Figure 11. SEM image/EDS map (#1) of sample 144-005, collected from the canister side, 13.5 feet below the upper edge.

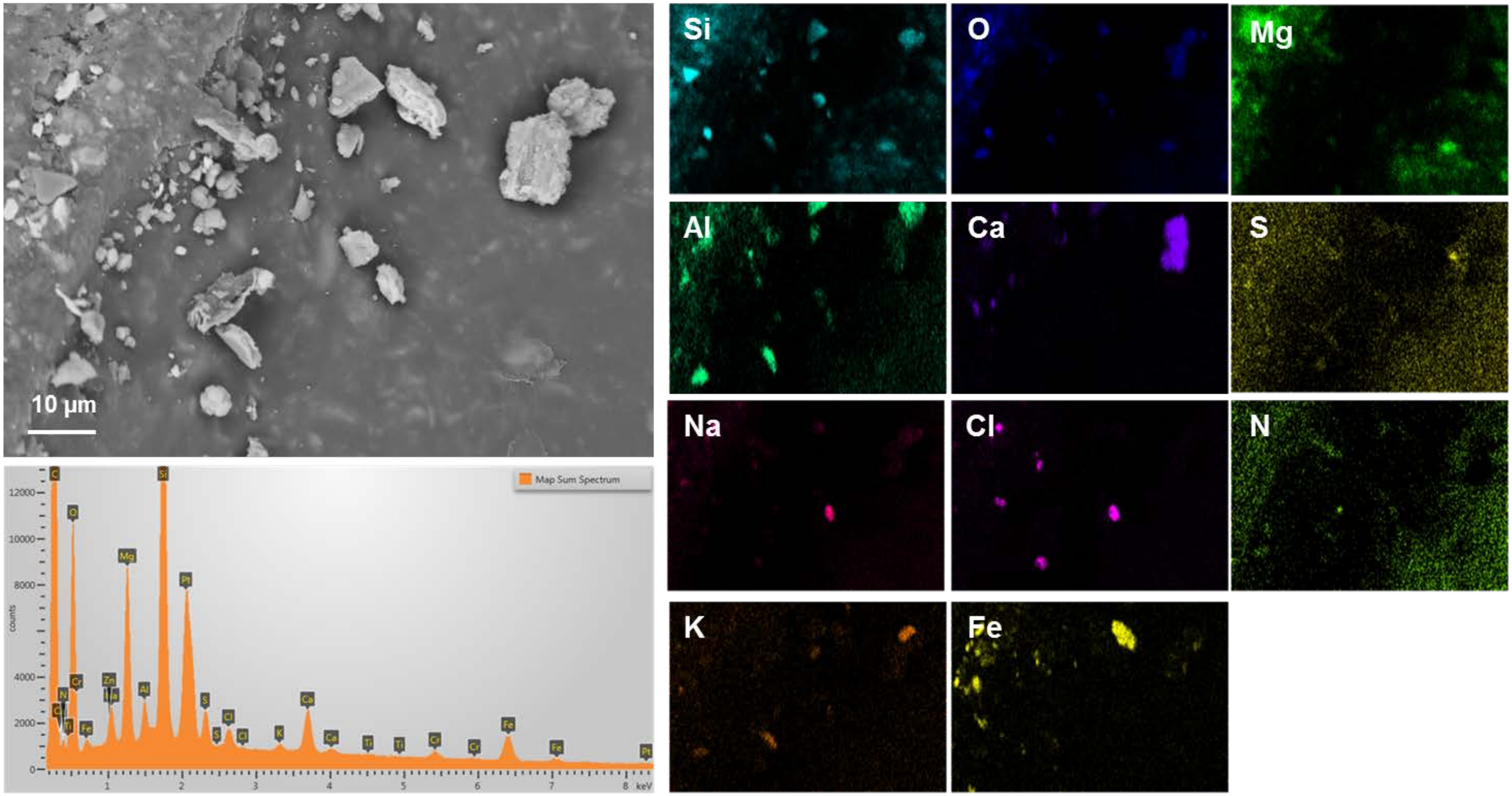

Figure 12. SEM image/EDS map (#2) of sample 144-005, collected from the canister side, 13.5 feet below the upper edge.

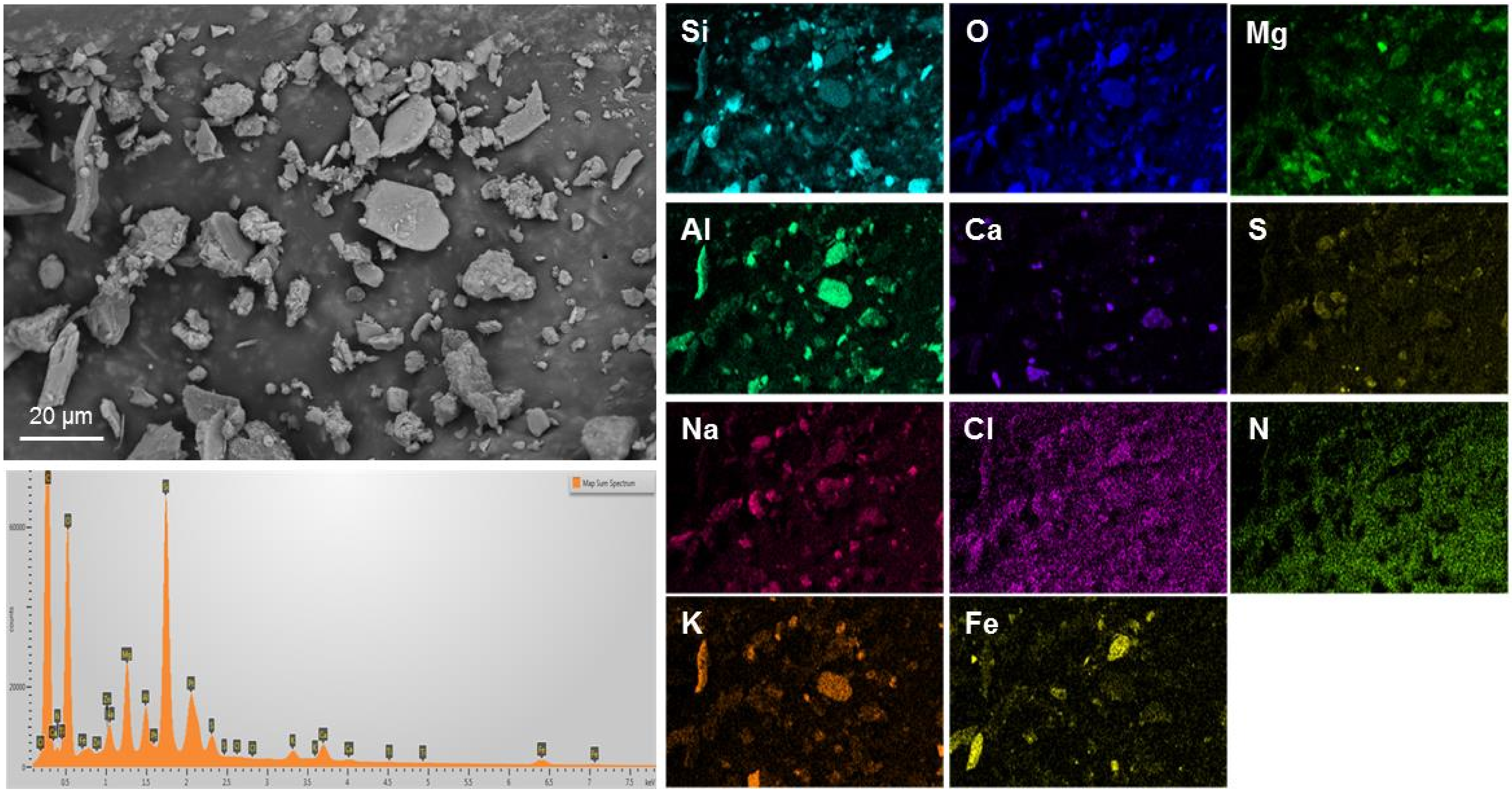

Figure 13. SEM image/EDS map (#2) of sample #144-011, collected from the canister top.

Summary of Hope Creek SEM/EDS results. To summarize, dust loads on the dry pad samples from the Hope Creek storage canisters were very light on the pads from the canister sides and heavy on the pads used to sample the upper surface. The mineralogy is similar over the entire surface of each canister, and on both canisters. The dust consists largely of terrestrially-derived detrital grains of quartz and aluminosilicates, including larger grains of feldspars and the micas, and sparser grains or aggregates of possible clay phases such as kaolinite and illite. Other common phases are particles of 304SS, sparse iron oxides, and Ca-carbonate. Salts were rarely observed in the dust, and consist largely of Ca-sulfate and rare grains of NaCl. Other materials present include pollen and iron oxide spherules (possibly representing oxidized fly ash or welding spatter).

The salts in the Hope Creek samples occur as heavily etched individual grains of NaCl, often only a few microns across, although a single spherical aggregate was seen in one image (see lower left center, Figure 12). It is not clear that these salts originate as sea-salts. The NaCl grains observed at Hope Creek may source to mist and fog being emitted from the nearby onsite cooling tower, which uses brackish river water. These do not resemble the sea-salt aerosols on the Diablo Canyon canisters, which consist of aggregates of NaCl and Mg-SO_4, as described in the next section.

2.4.1.3 Diablo Canyon Samples

Two canisters were sampled at the Diablo Canyon ISFSI. These were designated MPC-123 and MPC-170. Because salt minerals comprised a large fraction of the dusts on these packages, a suite of samples was analyzed from each canister, including 3 samples from the side and one from the top of each canister. For each sample, representative SEM image/EDS element map combinations are discussed here and additional analyses are provided in Appendix A.

MPC-123. For canister MPC-123, samples 123-006, 123-008, and 123-009 were collected from the canister side at distances, respectively, of 11, 7.5, and 3.0 feet below the upper edge of the canister MPC-123. Dust and salt loads were extremely light for all of these samples from the vertical side of the cask. Sample 123-012 was taken from the flat top of the canister, and was heavily loaded with dust.

The minerals observed on all of the samples from MPC-123 are listed in Table 5. Insoluble species vary little from canister top to side. Aluminosilicates are abundant, including feldspars and biotite, and fine particles or aggregate grains of clay minerals. Quartz is common. Fe-bearing phases are very abundant, and have variable compositions and morphologies. Fe-rich and Fe-Cr-rich particles are common, and occur in both metallic and oxidized form; they are generally angular, and probably represent variably oxidized particulates generated by machining during construction of the canister. But they can also be spherical, and apparently formed by welding or torch cutting of steel and stainless steel. However, while the insoluble phases are similar everywhere on the package, the salt phases at different locations do vary, as discussed below.

SEM/EDS data for sample 123-006 collected 11.0 feet below the upper edge of the canister, are shown in Figure 14 and Figure 15. Dust was sparse on this sample, but in Figure 14, several phases can be recognized, including quartz, K-feldspar, and a Ca-O phase which is probably calcium carbonate. This image also illustrates the variability in the Fe-bearing phases present in the dust. In addition to Fe-oxides, there is a large particle of Fe-Cr (stainless steel) and a sphere of Fe-Cr oxide, apparently an oxidized melt droplet formed by welding or cutting stainless steel. Figure 15 shows a few grains of NaCl; interestingly, the associated sulfate appears to be Ca-SO_4 rather than Mg-SO_4, as is commonly observed in these samples.

Table 5. Minerals Observed in Dry Pad Samples from MPC-123

Elemental analysis	**Morphology**	**Interpretation**	**Abundance**
Si-O	Angular grains	Quartz fragments	Common
K-Al-Si-O	Blocky, angular fragments	K-feldspar	Abundant
Ca(±Na)-Al-Si-O	Blocky, angular fragments	Calcic plagioclase	Rare
Ca-Fe-Al-Si-O	Large angular grains	Mafic aluminosilicate?	Rare to common
Ca-Mg-Fe-Al-Si-O	Large flakes	Biotite	Rare
K-Fe-Al-Si-O	Aggregate grains	Clays?	Sparse
Al-Si-O	Angular grains and aggregates	Kaolinite?	
Al-O-(H?)	Angular fragment	Gibbsite or brucite?	Rare
Fe±Cr±O	Striated flakes and fragments, spheres	Steel particles, of varying oxidation, generated by machining, Spheres generated by cutting and welding?	Abundant
Ca-S-O	Aggregate grains	Gypsum or anhydrite	Sparse
Ca-K-S-O	Aggregate grains	Aggregate of sulfates?	Rare
Na-Cl + Mg-S-O + Ca + K	Sea salt aggregates, commonly spherical. Cubes of NaCl associated with sheaf-like clusters of Mg-sulfate. Minor Ca and K, commonly associated with the sulfate.	Sea-salt aggregates	Abundant
Na-Cl-N-O	Anhedral grains	Nitrate was on the grain surface and rapidly burned off in the beam; interpreted as NaCl, partially converted to $NaNO_3$ via particle-gas conversion reactions.	Sparse (Common in sample 123-009)
Na-N-O	Fine grains	Sodium nitrate, possibly representing NaCl converted to NaNO3 via particle-gas conversion reactions	Sparse (Common in sample 123-009)
Ca-O-(C?)	Cylindrical needle	Calcium carbonate-biogenic	Single Feature
Ca-O-(C?)	Toothed blade	Biogenic calcium carbonate structure	Single feature

Dust on sample 123-008, somewhat higher on the package, has a similar mineralogy (Figure 16) in that phases likely produced during the manufacturing of the canister dominate the dust assemblage. Steel particles of varying degrees of oxidation, including Fe-Cr (stainless steel), Fe-Cr oxide, Fe metal and Fe oxide are common. Also present is a single grain of pyrite (Fe-S), and a grain of an Al-O-(H?) phase. A few tiny grains of NaCl are present, but also a particle of $NaNO_3$; another grain appears to be mixture of the two salts.

SEM/EDS data for 123-009 are shown in Figure 17 and Figure 18. This sample represents the canister side just below the upper edge, and it was the hottest location sampled at Diablo Canyon. As with the other canister side samples, dust was very sparse. Figure 17 shows little but Fe-Cr particles and salts. In contrast to most other samples from Diablo Canyon, the salts are mostly $NaNO_3$ particles, with only a few NaCl grains. Other maps of this sample (REF) show composite NaCl-$NaNO_3$ particles. For these composite grains; it was observed that the X-ray beam caused the grains to shrink, and the relative abundance of nitrogen decreased the longer the grain was in the beam. For these composite grains, it appears that the nitrate was mostly present on the surface of the NaCl grains. A 20 µm Ca-carbonate rod of probable biogenic origin is also present in Figure 17. Figure 18 shows another location on the pad, where NaCl is more common, althoughNaNO$_3$ is still present. The NaCl grains are co-located and apparently intergrown with a Ca-SO_4 phase (calcium sulfate). Again, this is unusual, as most sea-salt grains on the Diablo Canyon canisters are mixtures of NaCl and Mg-SO_4.

Sample 123-012 is from the top of the canister, and is heavily loaded with dust. Moreover, the dust compositions vary significantly from the samples collected from the sides of the canister (Figure 19 and Figure 20). Salt aggregates, consisting of NaCl + Mg-SO_4 (referred to as Mg-SO_4 rather than $MgSO_4$, because the hydration state is unknown), with minor associated Ca and K, are abundant in the dust. These aggregates are commonly hollow spherical aggregates of halite crystals with intergrown Mg-sulfate, but euhedral halite crystals with associated Mg-sulfate also occur. Since Na, Cl, Mg, and SO_4 are the most abundant ionic species in seawater, these are certainly sea-salt aggregates. The hollow spheres formed when droplets of seawater, suspended in the air by breaking waves, evaporated from the outside inwards. They commonly have an aperture, apparently where the last fluid escaped. As morning fogs are common at Diablo Canyon, it is likely that this evaporation occurred, in at least some cases, within the overpack as the deliquesced sea-salt droplets were drawn in and moved upwards through the heated annulus. Figure 19 illustrates the abundance of salts in the dust, and Figure 20 is a close-up of three salt aggregates, showing the size and morphology. Figure 21 magnifies a single sea-salt aggregate, showing the structure of the aggregate, and the relationship between the NaCl crystals and the interstitial Mg-SO_4. Several examples of the sea-salt aggregates from sample 123-012 are shown in Figure 22. While sea salt particles of all sizes are present on the canister surfaces, the aggregates are commonly quite coarse, in the 5-20 µm size range, and it is likely that these large grains account for most of the chloride deposited on the canister surfaces.

Samples from the side of canister MPC-123 differ from samples collected from the top of the canister in several ways. First, particles associated with manufacturing (i.e., Fe-Cr particles) are proportionally more common on the pad samples from the canister side. It is likely that this is mostly because the environmentally-derived proportion of the dust is much smaller on the side than on the top. Second, salt aggregates are mixed NaCl/Ca-SO_4 minerals rather than the NaCl and Mg-SO_4 aggregates found on the canister top (and on all samples from MPC-170). Finally, nitrates particles and nitrate-chloride mixed grains are present only on the side of MPC-123, not on the top, and not on MPC-170. The compositional difference may be a function of particle size as salt particles on the sides of the canister are generally smaller than those on the top. Temperature may also play a role—the greatest abundance of nitrate-containing particles is on the sample from the hottest location (sample # 123-009) on the package. We speculate that the nitrate represents particle-gas conversion reactions that occurred prior to the salts entering the overpack—reactions with HNO_3 in the air that convert chloride particles to nitrates. This process is more efficient for small particles, and results in a NaCl mineral grain partially converted to $NaNO_3$. At high canister surface temperatures, nitrate and mixed chloride-nitrate particles were preserved on the canister surface, because deliquescence and acid degassing did not occur. At lower temperatures, deliquescence of the mixed salts occurred and both HCl and HNO_3 degassed; however, chloride was replenished in the deliquesced brine by dissolution of the underlying chloride mineral. Replenishment of nitrate did not occur, so the nitrate was eventually depleted. This also explains the corroded surface of many of the NaCl crystals on the canister surfaces.

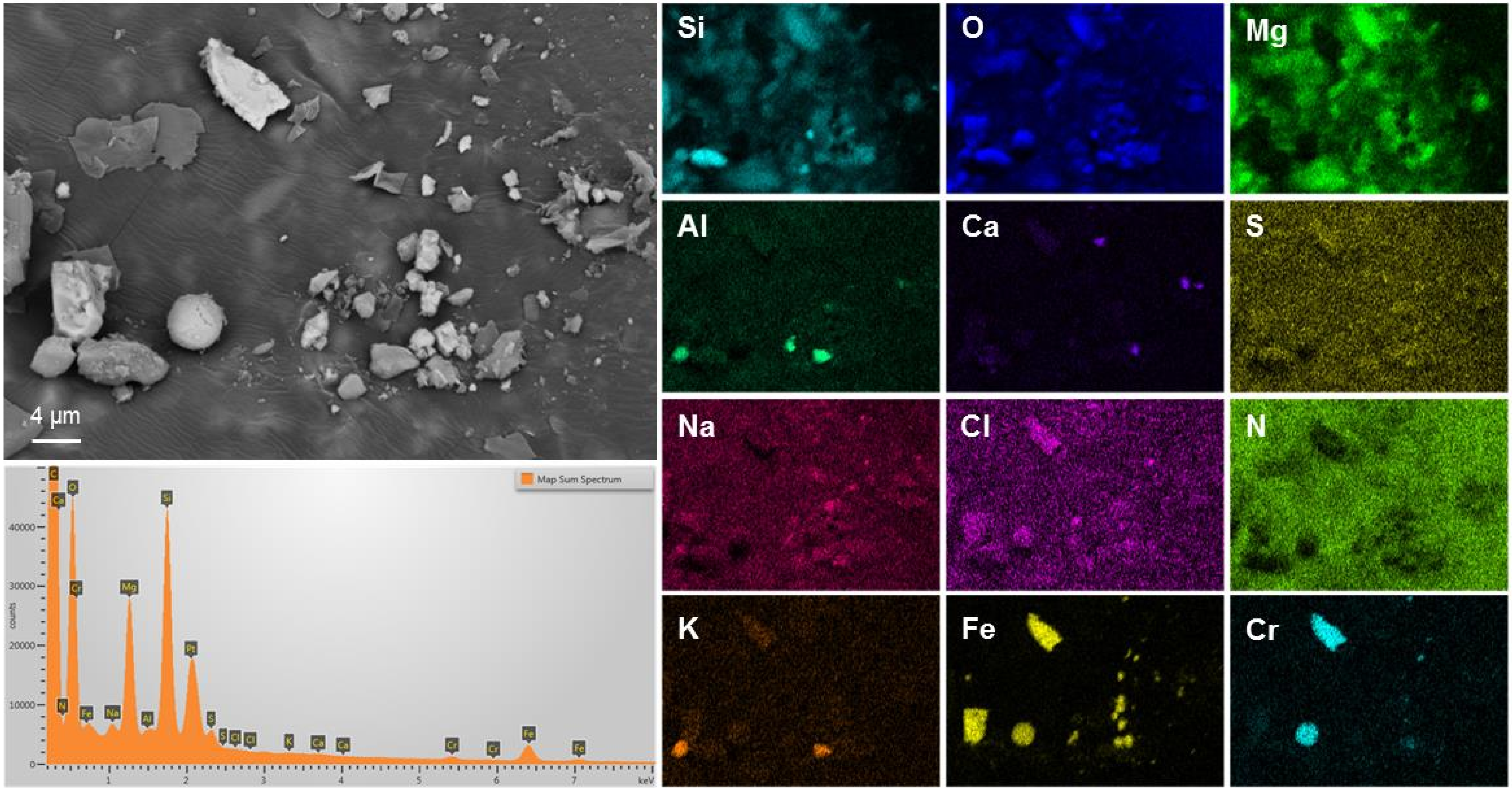

Figure 14. SEM image/EDS map (#1) of sample 123-006, collected from the canister side, 11.0 feet below the upper edge.

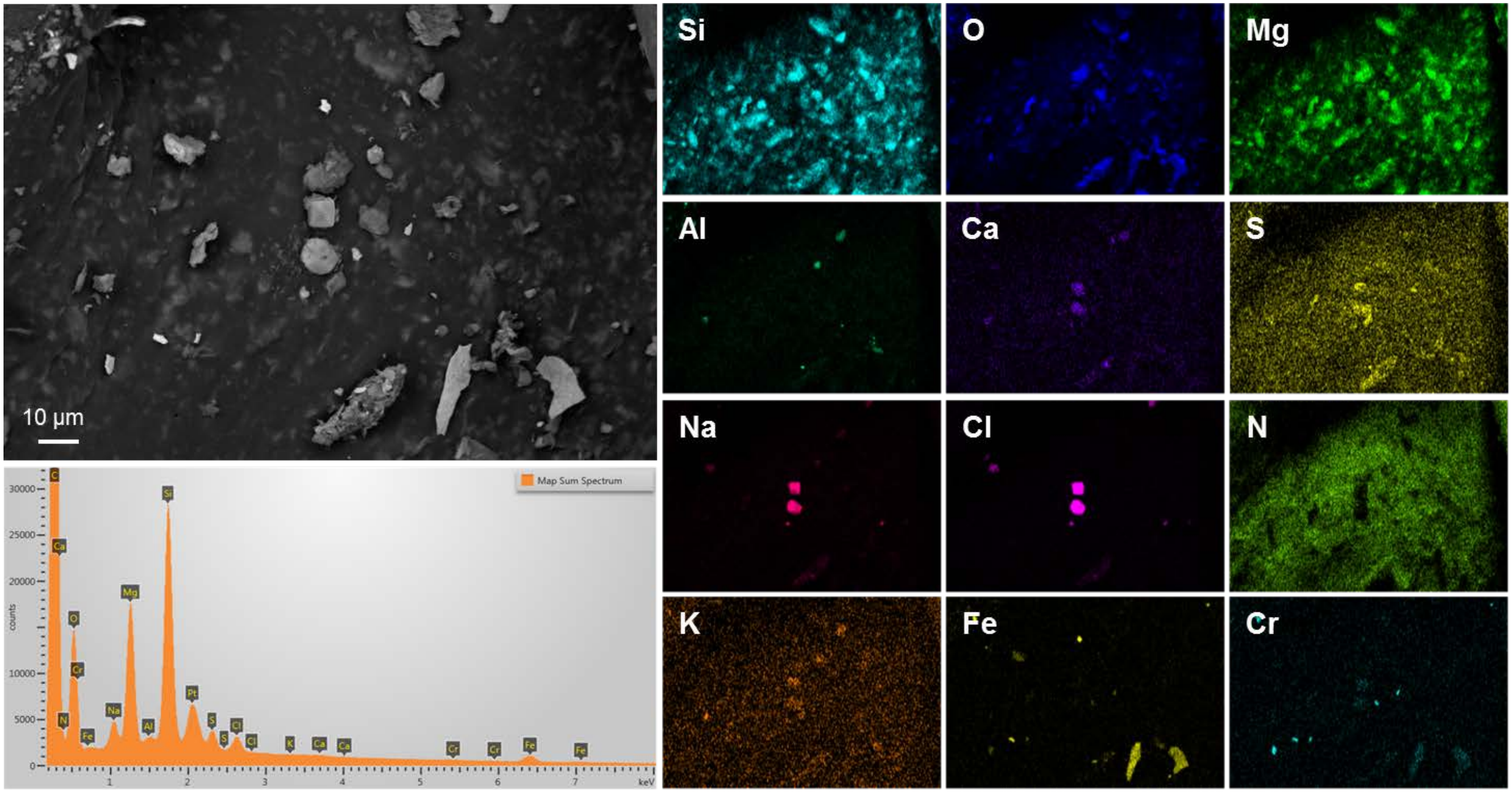

Figure 15. SEM image/EDS map (#2) of sample 123-006, collected from the canister side, 11.0 feet below the upper edge.

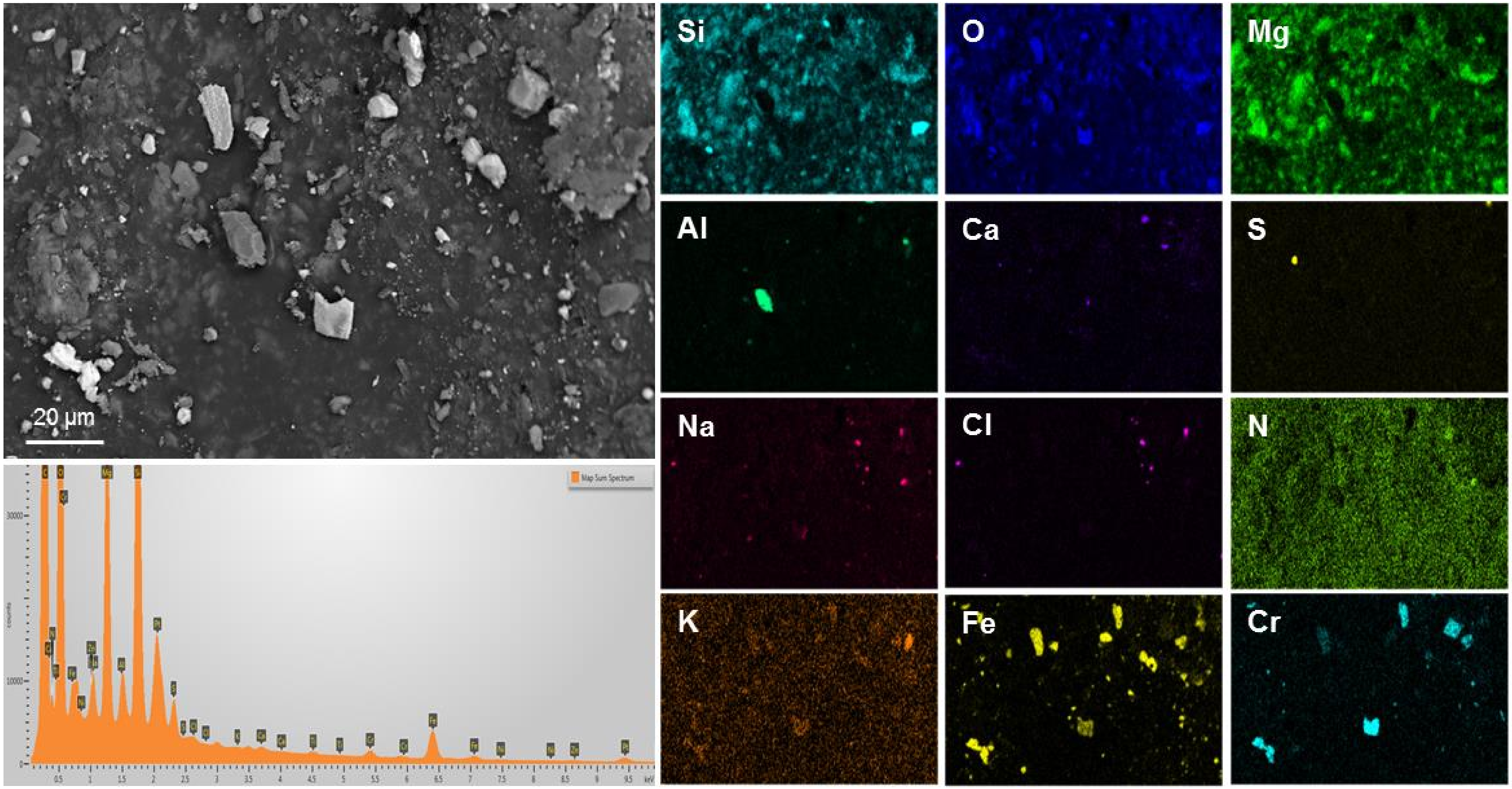

Figure 16. SEM image/EDS map (#1) of sample 123-008, collected from the canister side, 7.5 feet below the upper edge.

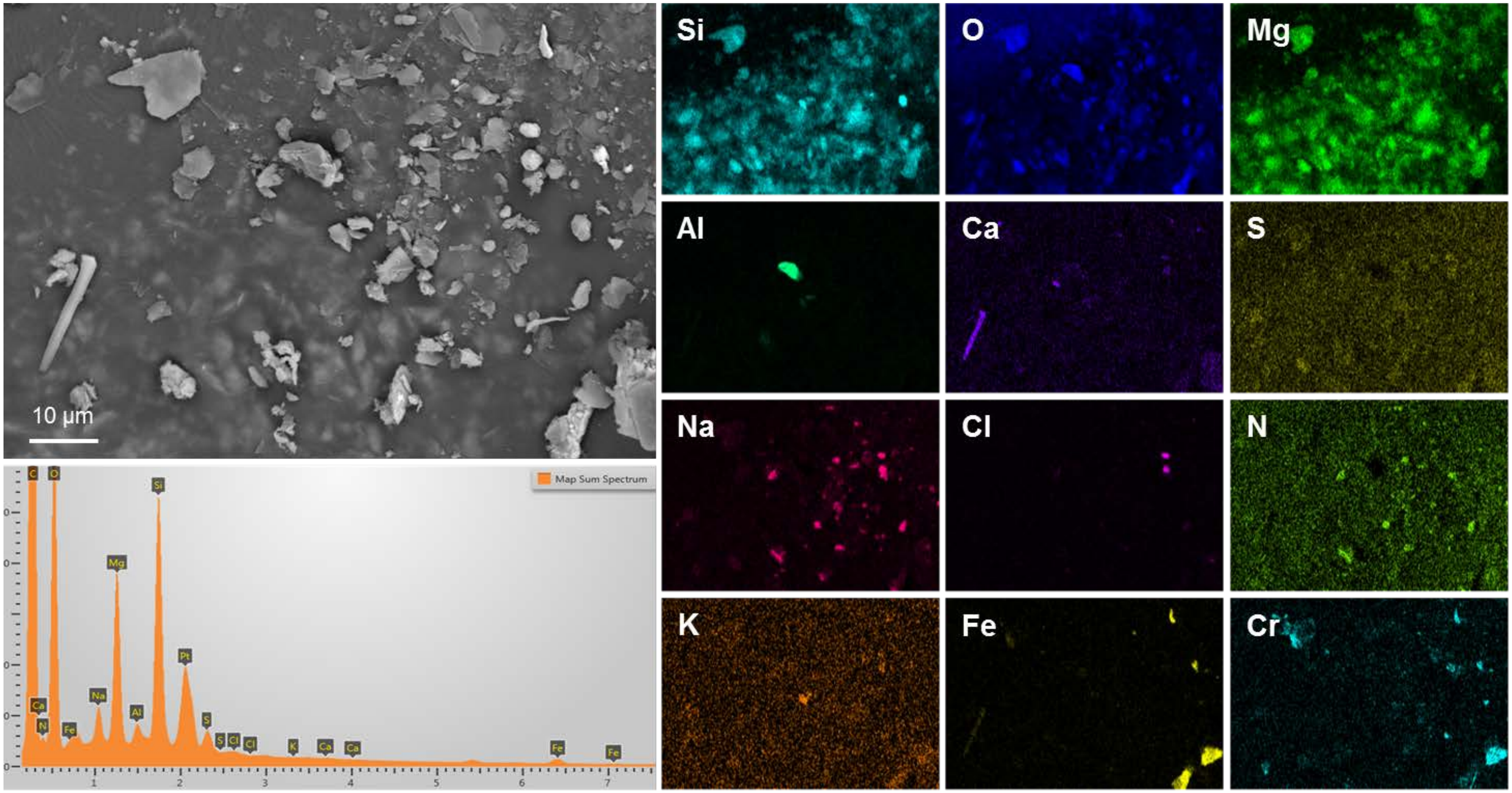

Figure 17. SEM image/EDS map (#1) of sample 123-009, collected from the canister side, 3.0 feet below the upper edge.

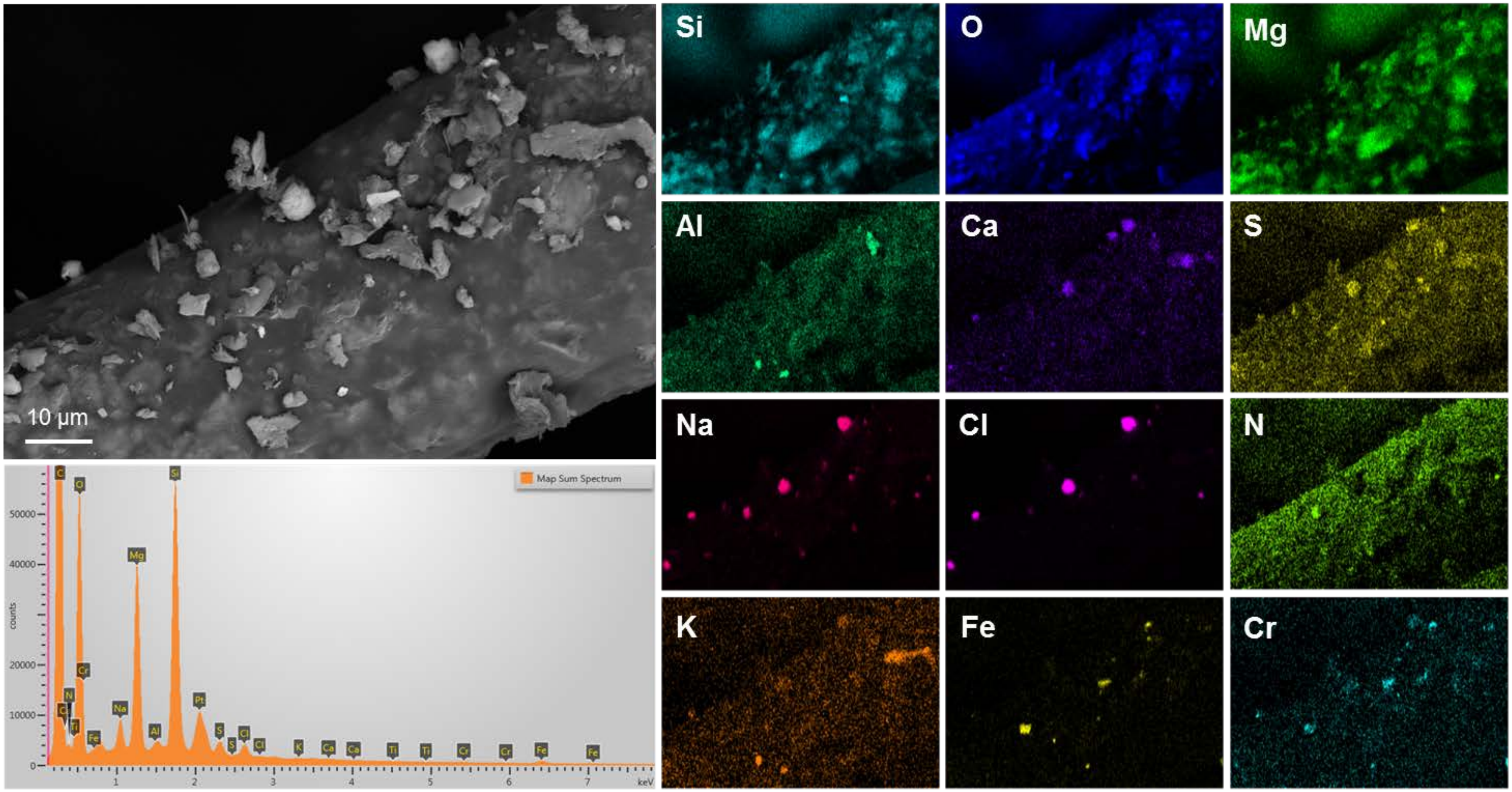

Figure 18. SEM image/EDS map (#2) of sample 123-009, collected from the canister side, 3.0 feet below the upper edge.

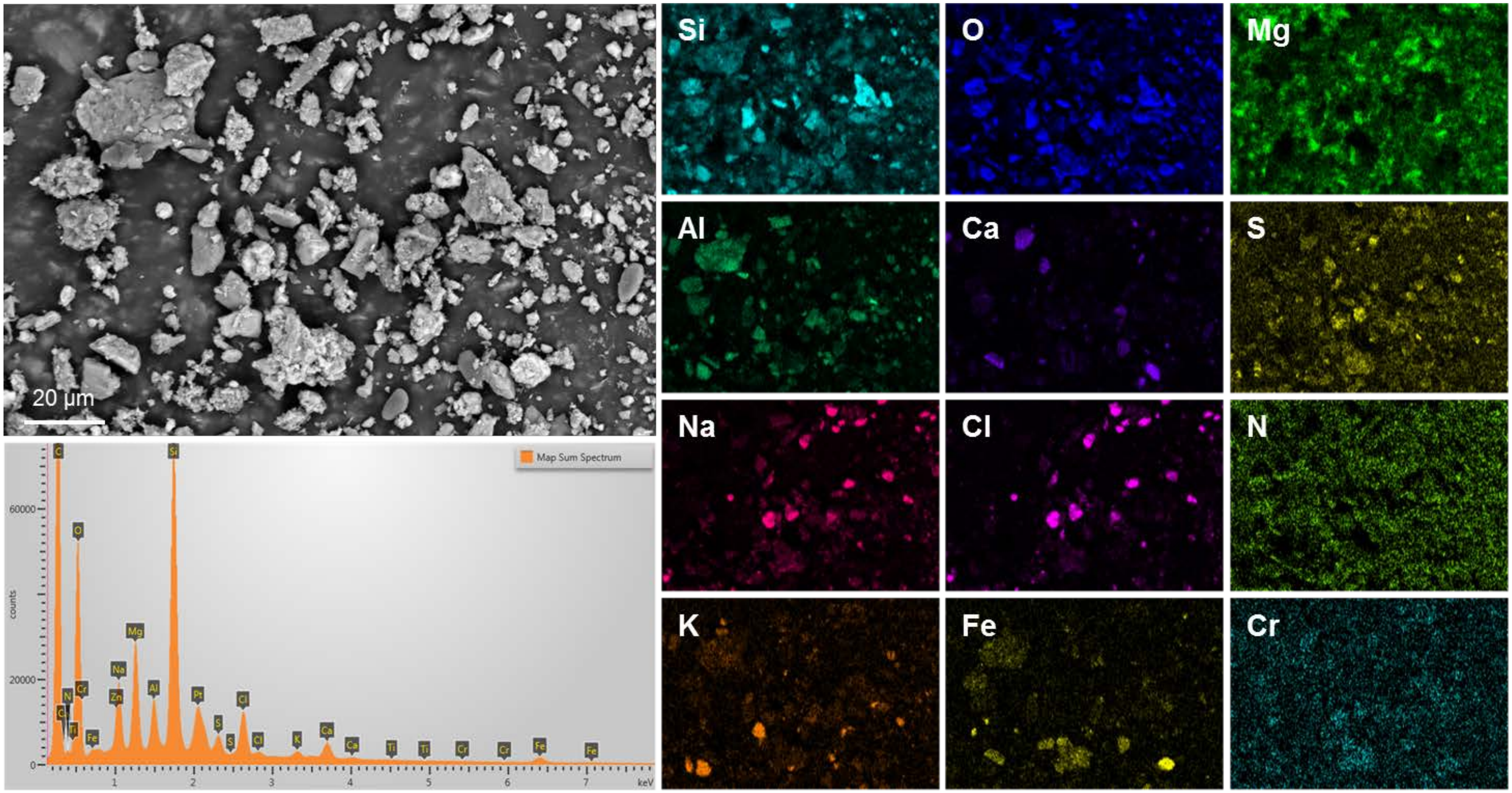

Figure 19. SEM image/EDS map (#1) of sample 123-012, collected from the canister top.

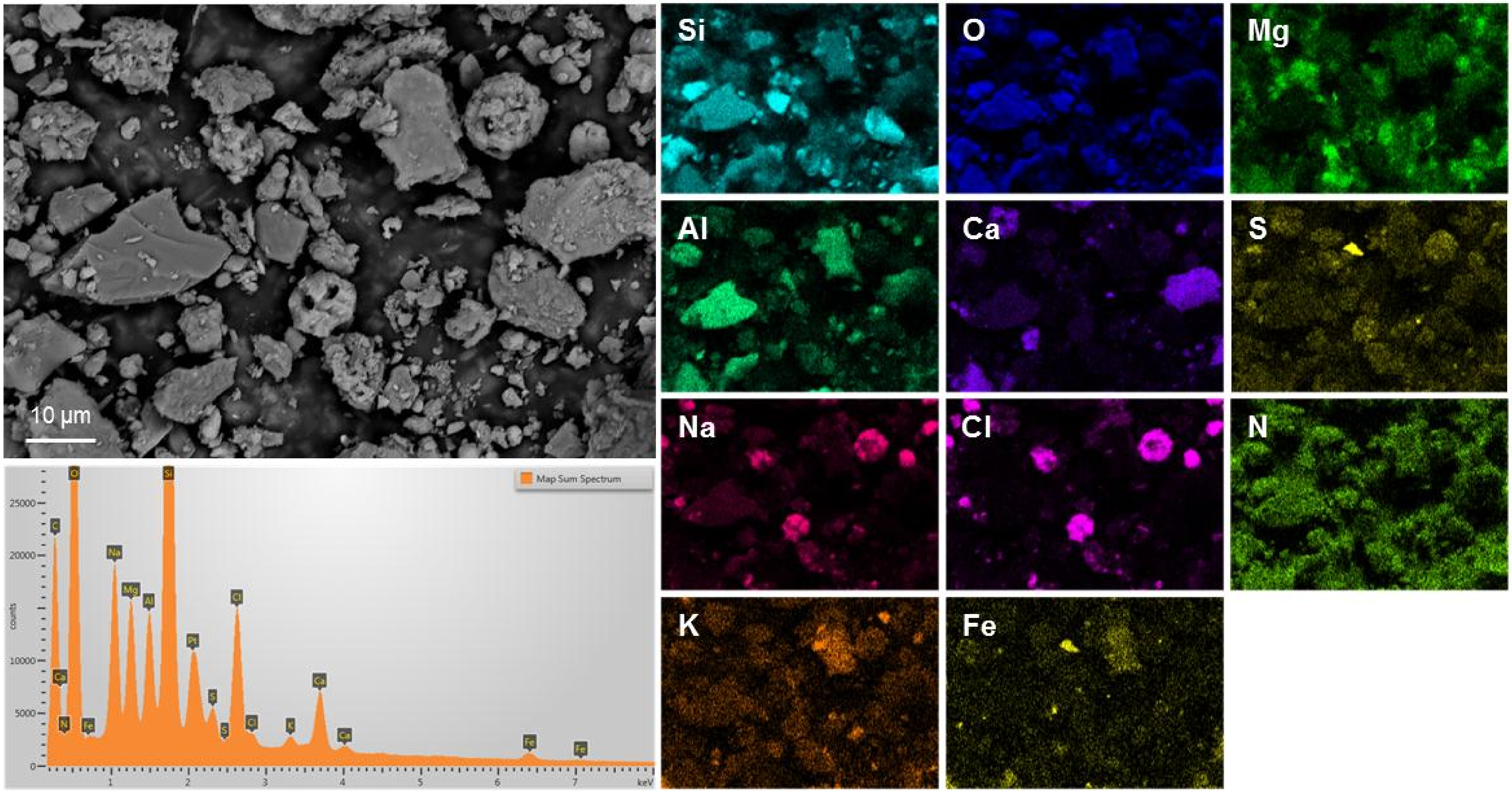

Figure 20. SEM image/EDS map (#2) of sample 123-012, collected from the canister top.

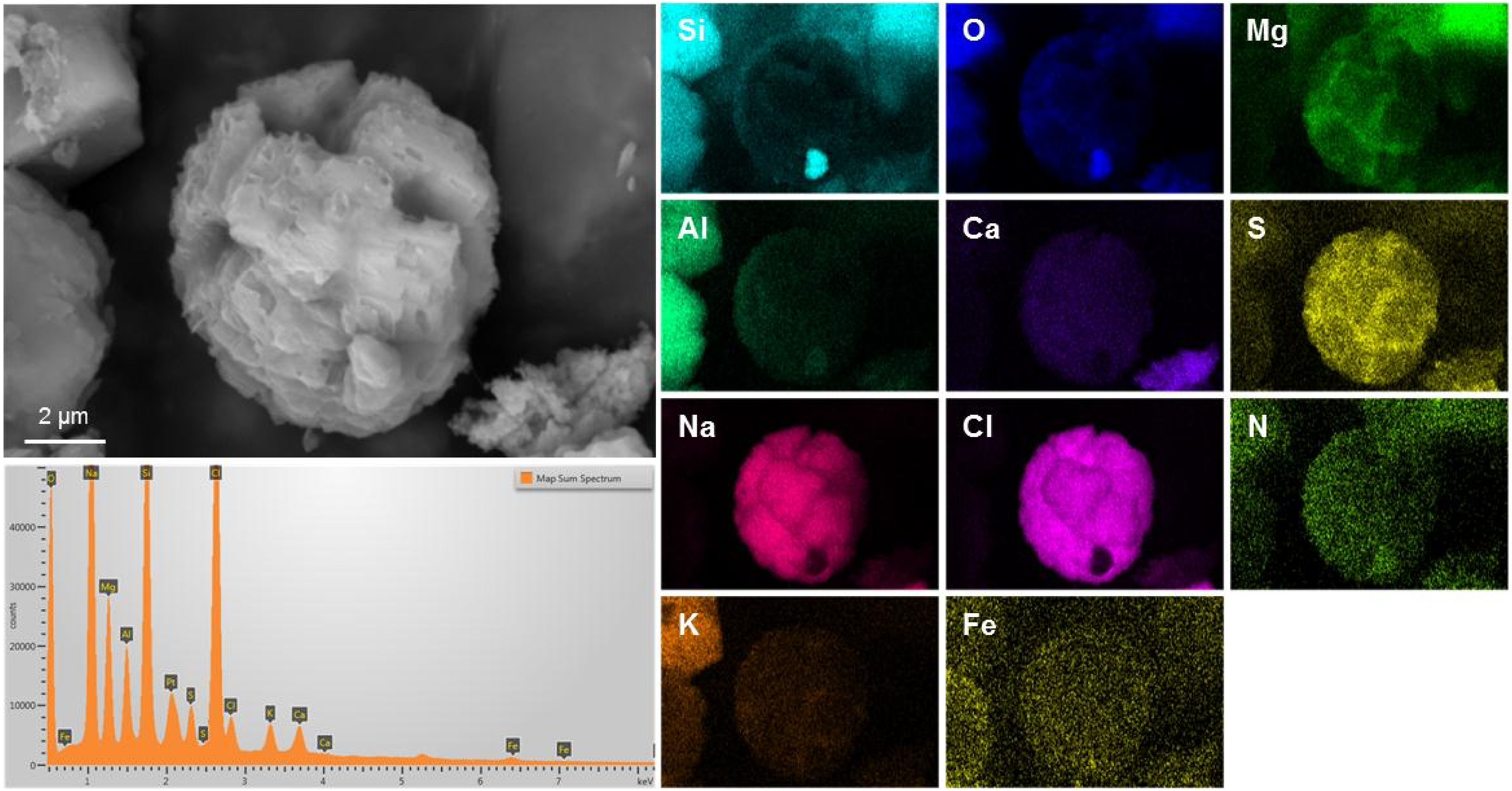

Figure 21. SEM image/EDS map of a sea-salt cluster in sample 123-012, collected from the canister top.

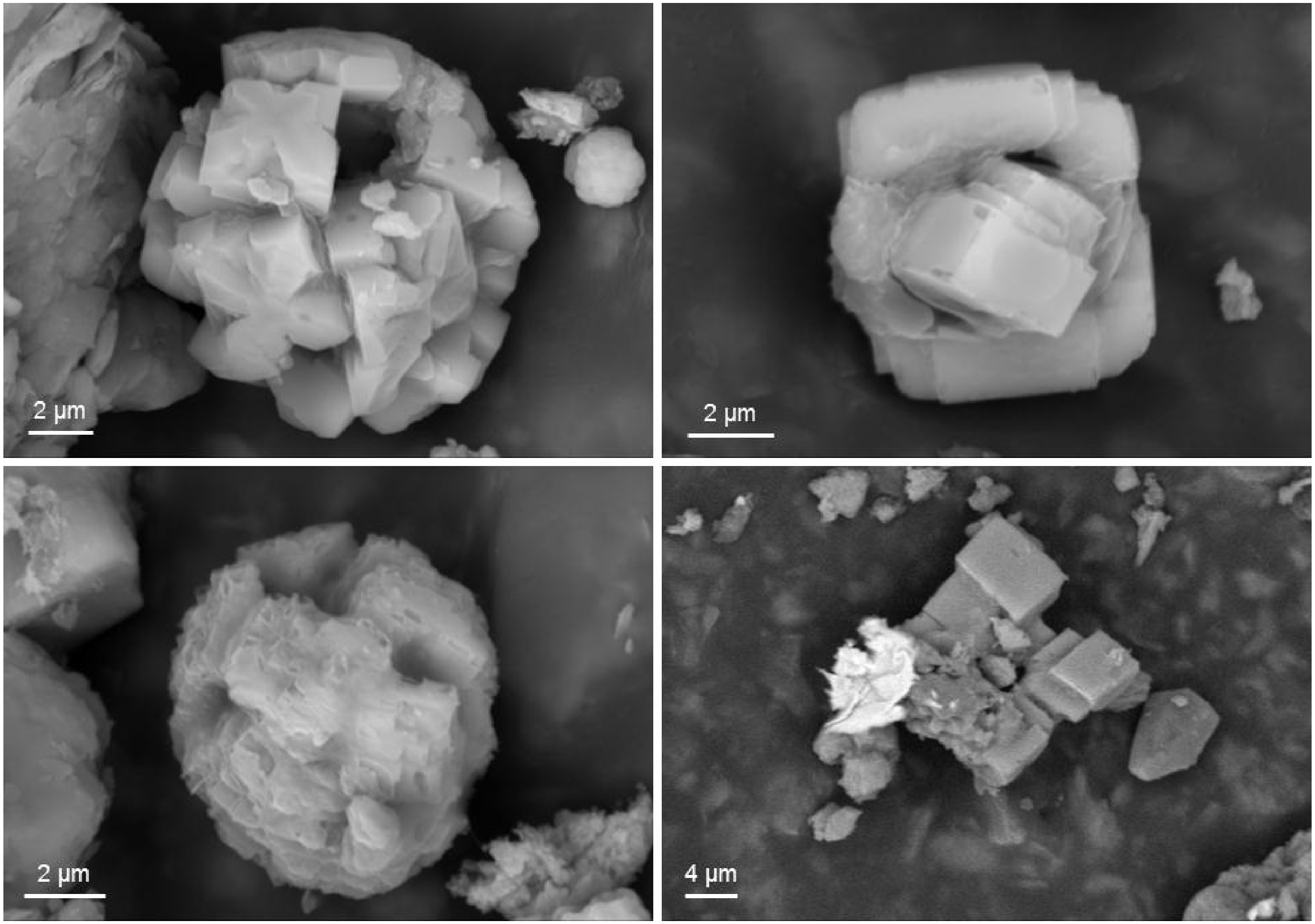

Figure 22. SEM images of sea-salt (intergrown NaCl cubes with interstitial Mg-SO4) aggregates in sample 123-012, collected from the canister top.

MPC-170: Four samples were also analyzed from canister MPC-170. Samples 170-004, 170-005, and 170-006 were collected from the canister side at distances, respectively, of 11, 7.5, and 3.0 feet below the upper edge of the canister. As with MPC-123, all of the dust and salt loads were extremely light for samples collected from the vertical side of the canister; in many cases, only a few spots on the sample pad had any visible dust. Sample 170-003 was taken from the flat top of the canister, and was heavily loaded with dust. The minerals observed in the samples from MPC-170 are listed in Table 6. Unlike MPC-123, the mineralogy varied little across the surface of MPC-170.

Sample 170-004 was collected from the canister side, 11 feet below the upper edge. Figure 23 and Figure 24 show the variability of the dust on the pad, which was very lightly loaded. Dust in Figure 23 consists of a few coarse (<20 µm) grains of quartz and aluminosilicate, with some finer sea-salt aggregates. Figure 24 shows an accumulation of dust on an abraded edge on the pad. The dust is almost entirely sea-salt particles, with a few aluminosilicates. Many of the sea-salt particles are very fine, and may have formed by comminution of coarser sea-salt grains as the pad was rubbed over the canister surface. The sea-salt aggregates are mixtures of NaCl and Mg-SO_4, with smaller amounts of Ca and K, generally associated with the sulfate.

Sample 170-005 was collected 7.5 feet below the upper edge of the canister. The dust load on the pad was very sparse. Figure 25 shows one of the few locations on the pad with dust particles, near an abraded edge. Most of the particles in the image are talc, freed by abrasion of the pad, but aluminosilicates and sea-salt particles are also present. Sample 170-006 was collected 3.0 feet below the upper edge of the canister, and was practically dust-free. Figure 26 shows an abraded fiber, heavily coated with talc particles freed by abrasion of the pad. But a few dust particles are present, and they are mostly stainless steel particles. A few grains of NaCl are also present.

Sample 170-003 was collected from the flat top of the canister, and the pad was heavily loaded with dust. Figure 27 shows a typical region on the pad. The dust consists largely of aluminosilicate minerals, with common sea-salt aggregates of intergrown NaCl and Mg-SO_4; Ca-SO_4 is also common as a separate phase. A magnified view of a sea-salt particle on the sample pad is shown in Figure 28; this particular grain consists of intergrown halite and Mg-sulfate, and does not appear to be hollow.

The typical morphology and size of the sea-salt grains is illustrated in Figure 29. All of these images are from sample 170-003, but they are similar to the sea-salt aggregates on canister MPC-123 (Figure 22). These large aggregates, which formed by evaporation of aerosolized seawater droplets, generally range in size from 5-20 µm. Although sea-salt grains occur in the finer size fractions (e.g., <2.5 µm), the majority of the salts on the tops of the Diablo Canyon packages, in terms of mass, are present as coarse aggregates such as these.

Summary for Diablo Canyon canisters. The soluble salts collected from the tops of the canisters MPC-123 and MPC-170 have similar mineral and salt compositions, the salts being dominated by large sea-salt aggregates of NaCl and Mg-SO_4. However, the samples taken from the sides of the two canisters differ significantly. The salts on the sides of the packages are mostly finer grained, with a significant fraction being in the <2.5µm range. The dry pad samples from the sides of MPC-170 have higher loads of dust and sea-salts, and the sea-salt aggregates consist of NaCl and Mg-SO_4, while those on MPC-123 seem to be mixtures of NaCl and Ca-SO_4. Moreover, Ca-SO_4 is common as an individual mineral phase on the MPC-170 samples, while it is rare in samples from MPC-0123.

Finally, no nitrate minerals were observed on samples collected from the surface of MPC-170, although they were common in the samples collected from the sides of MPC-123. However, nitrate salts were found on sample 170-001, from the overpack gamma shield for MPC-170 (Bryan and Enos, 2014). It is not clear why the samples from the two canisters differ, but it is noted that the outlet vents that were entered for sampling the canisters faced in opposite directions. The vent for MPC-123 faced SSE, while that for MPC170 faced NNW. The nearest inlet vents to these outlets also faced in opposite directions. Perhaps the differences in salt composition are due to variations in the proportion of continentally-derived versus ocean-derived salts with vent direction. An additional difference between the two Diablo Canyon canisters is temperature. The surface of MPC-123 was somewhat hotter (Figure 4), potentially limiting deliquescence and acid degassing, and preserving the nitrate salts.

Table 6. Minerals Observed in Dry Pad Samples from MPC-170

Elemental analysis	**Morphology**	**Interpretation**	**Abundance**
Si-O	Angular grains	Quartz	Abundant
K-Al-Si-O	Blocky, angular fragments	K-feldspar	Common
Na-Al-Si-O	Medium to fine particles	Sodic plagioclase?	Common
Al-Si-O	Aggregates of grains	aluminum oxide/hydroxide	Sparse
K-Mg-Fe-Al-Si-O	Large flakes	Biotite	Abundant
K-Al-Si-O	Fine particles and aggregate grains	Illite?	Sparse
Ca-Al-Si-O	Blocky, angular fragments and fine grains	Calcic plagioclase (?)	Rare
Fe-Cr	Striated flakes and fragments	Stainless steel particles generated by machining	Abundant
Fe	long striated grain	Fe metal	Rare
Fe-O	Angular grains	Iron oxides	Common
Fe-O	Isolated spheres, some hollow	Fly ash or welding spatter (oxidized)	Rare
Ca-S-O	Very fine particles	Gypsum or anhydrite	Common
Ca-O-(C?)	Fine particles and aggregates	Calcium carbonate	Rare to common
Na-Cl + Mg-S-O + (Ca + K)	Sea salt aggregates, commonly spherical, of euhedral NaCl associated with sheaf-like clusters of Mg-sulfate. Minor Ca and K. Sometimes, isolated NaCl crystals. In 170-001, Na-Cl + Ca-SO_4 aggregates common.	Sea-salt aggregates	Abundant
Na-Zn-O	Rounded particles	Zr-rich paint particles from the outside of the overpack(?)	Rare
C	Oval to spherical particles	Pollen	Rare to common
C	Fibers	Plant matter	Rare

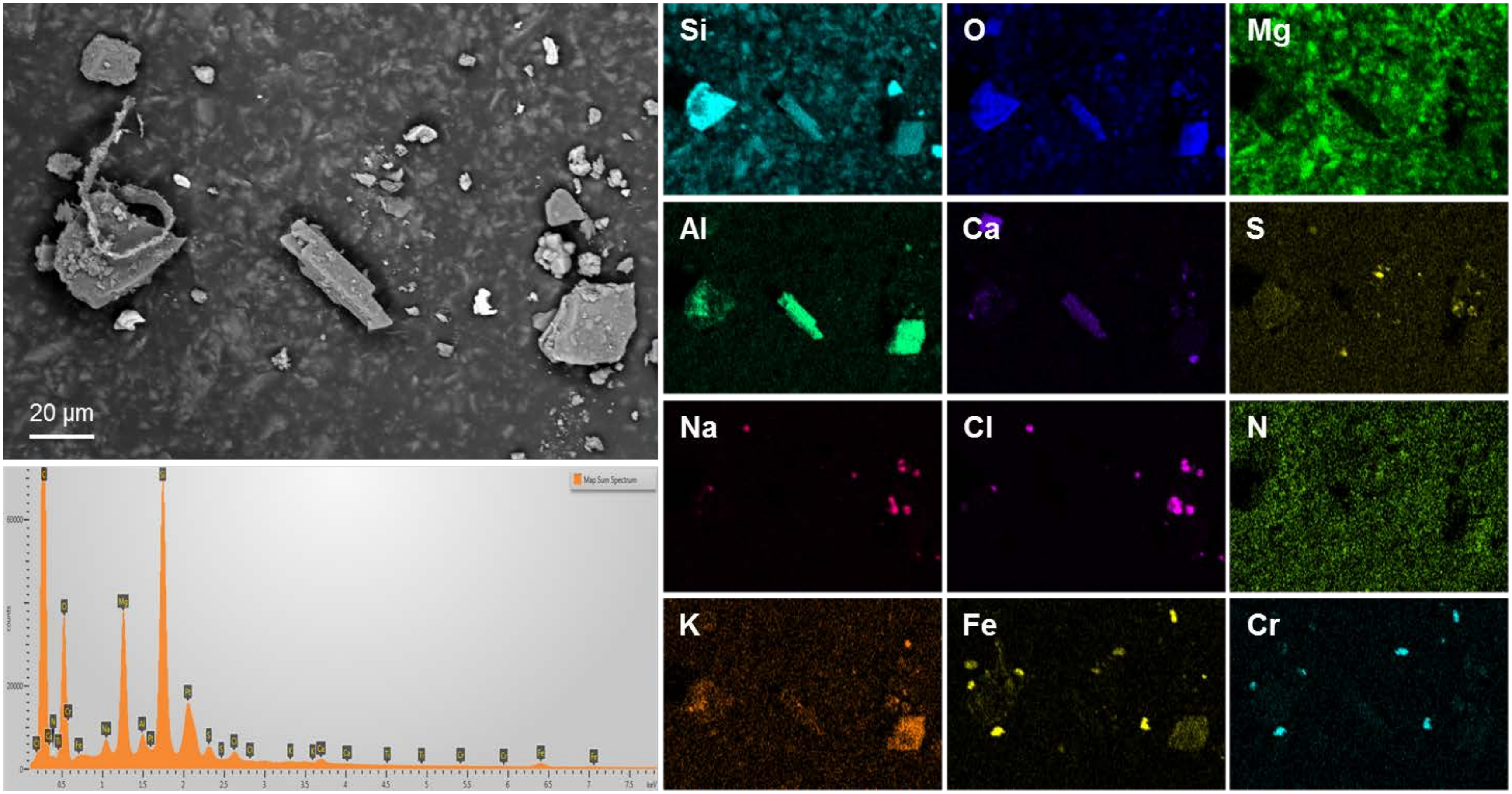

Figure 23. SEM image/EDS map (#1) of sample 170-004, collected from the canister side, 11.0 feet from the upper edge.

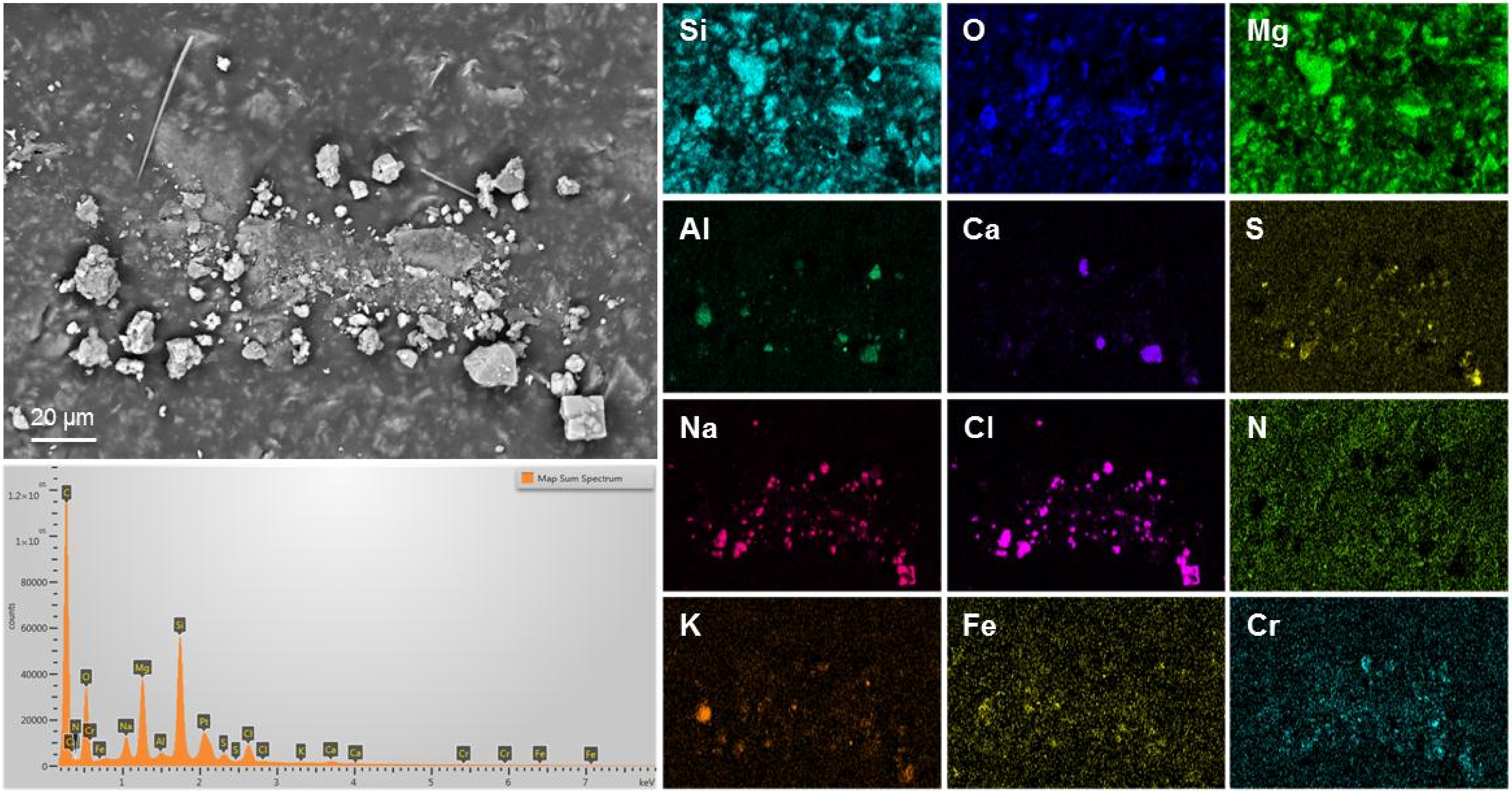

Figure 24. SEM image/EDS map (#2) of sample 170-004, collected from the canister side, 11.0 feet from the upper edge.

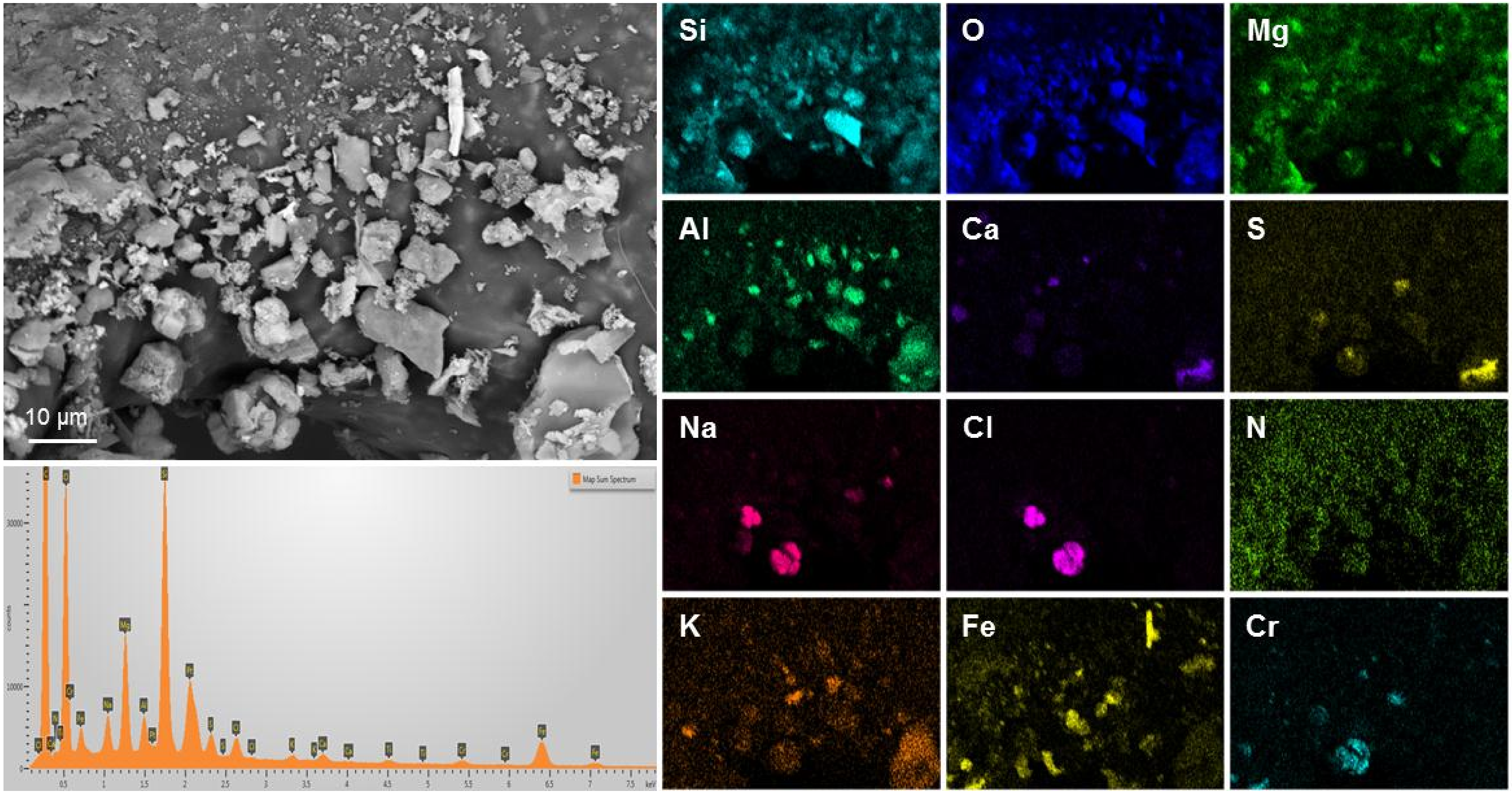

Figure 25. SEM image/EDS map (#2) of sample 170-005, collected from the canister side, 7.5 feet from the upper edge.

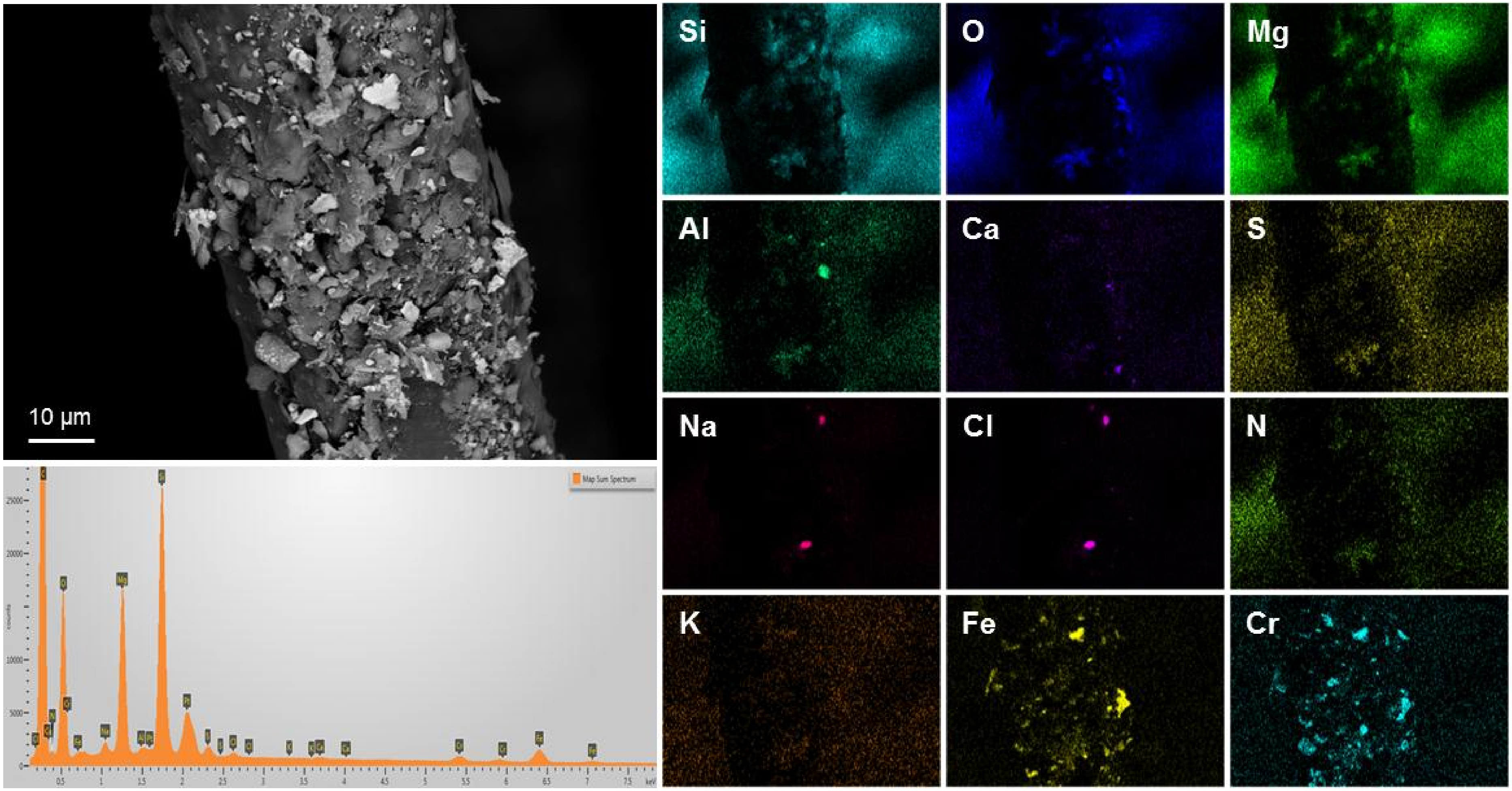

Figure 26. SEM image/EDS map of sample 170-006, collected from the canister side, 3.0 feet from the upper edge.

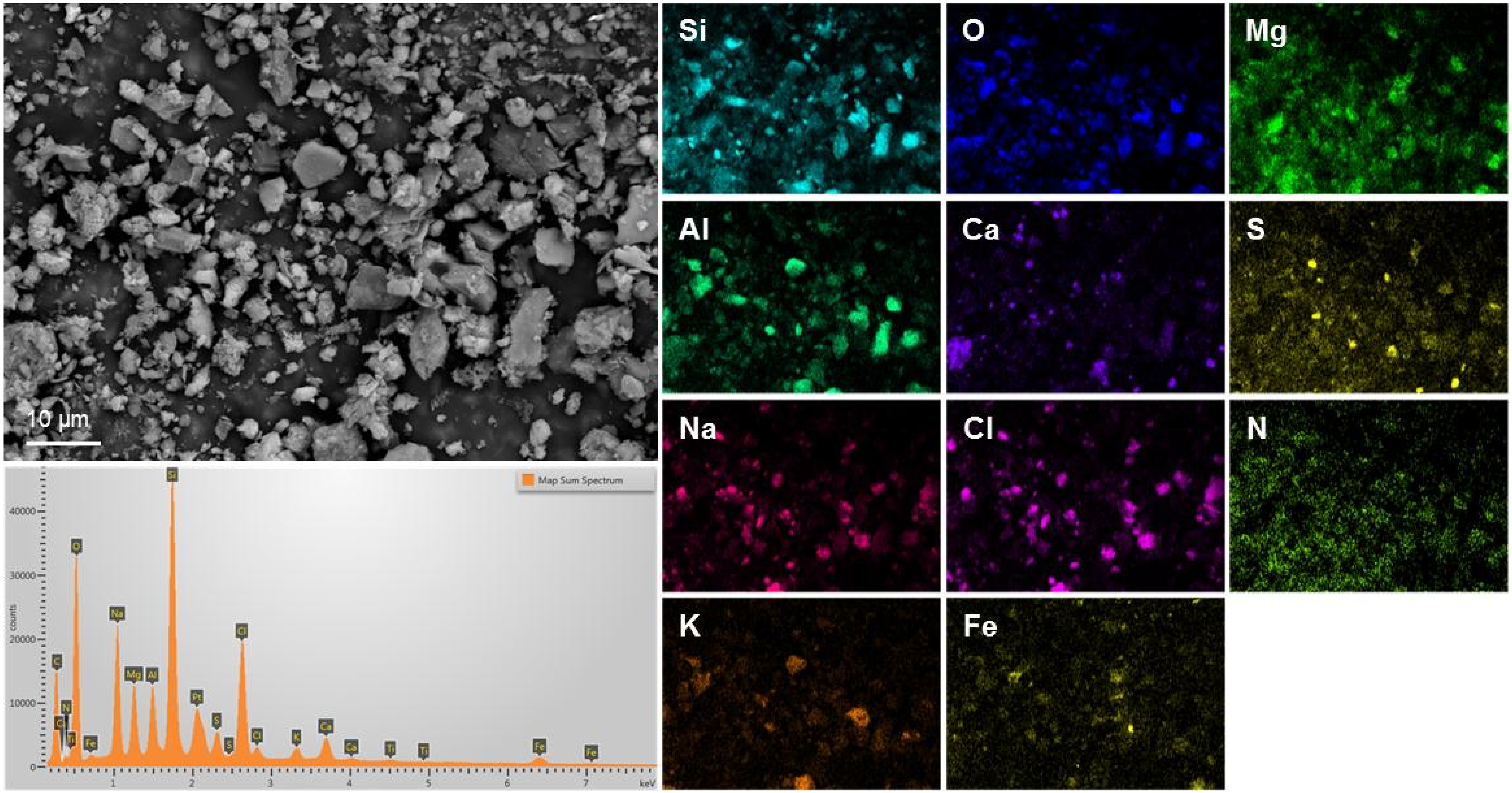

Figure 27. SEM image/EDS map (#1) of sample 170-003, collected from the top of the canister.

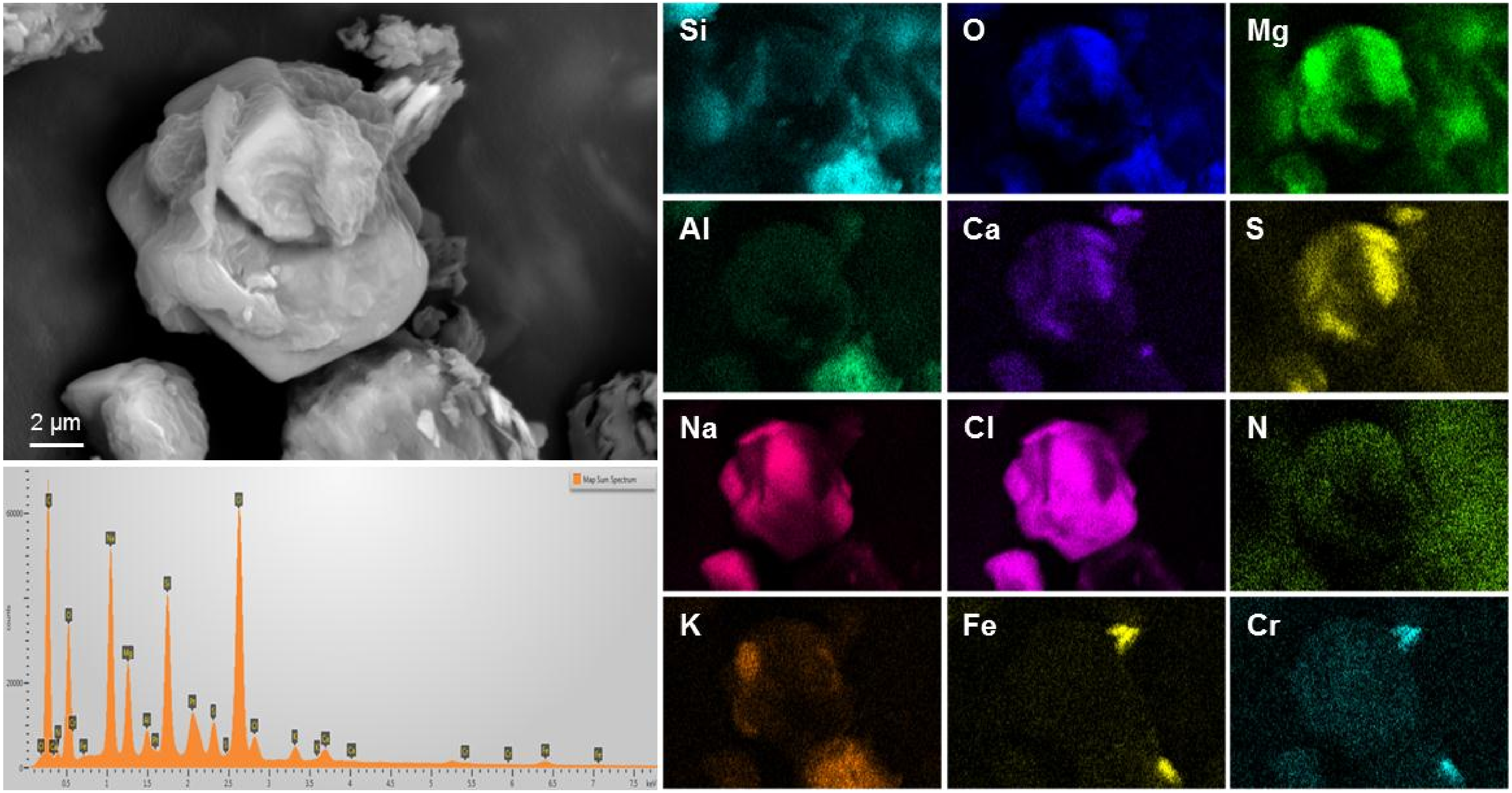

Figure 28. Magnified view of a sea-salt particle from sample 170-003 , showing intergrown NaCl and Mg-SO_4.

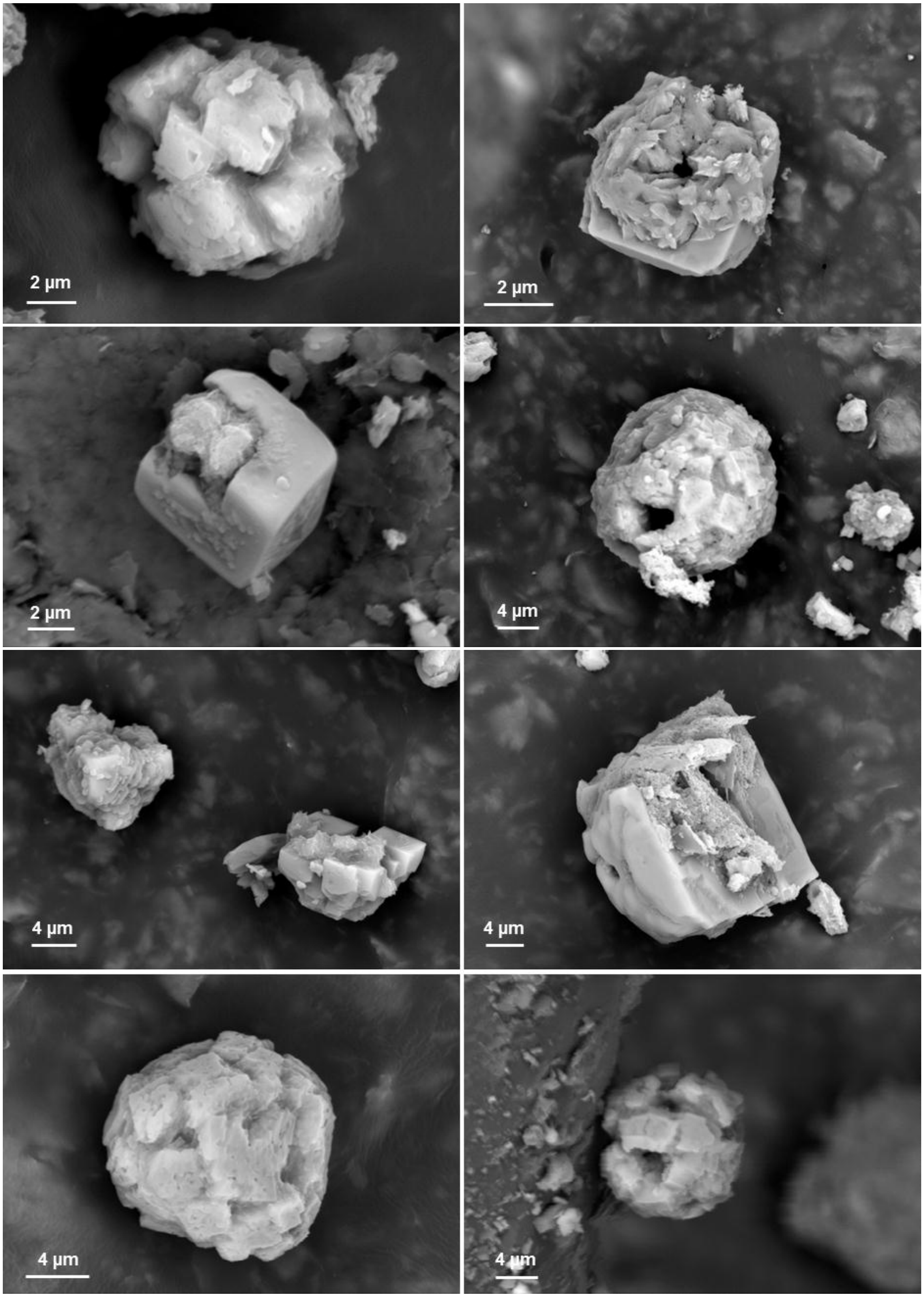

Figure 29. SEM images of sea-salt aggregates (intergrown NaCl cubes with interstitial Mg-SO$_4$) on sample 170-003, collected from the top OF mpc-170.

2.4.1.4 Summary of SEM/EDS analyses

To summarize, dust loads on the dry pad samples from the vertical sides of canisters at the Hope Creek and Diablo Canyon ISFSIs were very light, while the pads used to sample the flat tops of the canisters were heavily coated. In both cases, the dust consists largely of terrestrially-derived detrital grains of quartz and aluminosilicates, including larger grains of feldspars and the micas, and sparser grains or aggregates of possible clay phases such as kaolinite and illite. Carbonates of Ca and Ca-Mg were also common. Particles of 304SS, Fe-Cr oxides, iron, and iron oxide are common, and were generated during the canister manufacturing process. At Hope Creek, pollen was abundant in many samples, while at Diablo Canyon, pollen was rare, but fragments of diatoms and biologically derived carbonate structures were occasionally observed.

The composition and abundance of salt phases differed greatly at Hope Creek and Diablo Canyon. At Hope Creek, salts were rarely observed in the dust, and consist largely of Ca-sulfate and small (<5 µm), heavily etched grains of NaCl. At Diablo Canyon, salts were abundant, and occurred primarily as sea-salt aggregates of NaCl and Mg-SO_4. The morphology of these grains suggests they formed largely though evaporation of aerosol droplets of seawater, possibly after entering the heated overpack.

The SEM observations of dust from the surface of canisters MPC-123 and MPC-170 are critical to understanding the deposition, accumulation, and distribution of salts, and chloride, on the canister surfaces. If efforts are undertaken to characterize aerosols at the ISFSI sites using air samplers, a sufficient size range of particles must be sampled. Using PM10 sampling techniques is inadequate, as many of the sea salt grains that are deposited on the canister surfaces are larger than 10 µm. A method for sampling total suspended particulates (TSP) might be required. Also, the morphology of the sea-salt particles indicates that they formed by evaporation of seawater droplets suspended in the atmosphere. It is not clear when this evaporation occurred, but seems likely that on humid days, the sea-salts may be transported into the overpack dominantly as deliquesced or partially deliquesced droplets; the common occurrence of sea fogs in the Diablo Canyon area supports this conclusion. Therefore, the transported particles would be even larger and heavier than the observed sea-salt grains; again, this suggests that a TSP sampling method might be more accurate for determining the relevant atmospheric aerosol load than a PM10 instrument.

While the vast majority of the salt mass in the air is undoubtedly in large sea-salt particles, dust deposited on the sides of the canisters (the most critical location with respect to SCC), seems to have a relatively large fraction of finer sized (<2.5 µm) materials. Hence it is important to characterize the PM2.5 aerosol fraction as well. Moreover, the relative proportion of continental versus ocean-derived salts in air entering the overpack may vary with inlet direction, resulting in variations in the composition of deposited dusts. Many aerosol samplers use omnidirectional sampling heads, and yield only averaged values for dust composition.

The same caveats hold true for developing models for dust and chloride deposition. Any particle deposition model must consider a large range of particle sizes, as well as potential variations in dust composition with particle size (e.g. proportion of continentally-derived versus marine-derived particles). It might be necessary to consider the effects of inlet vent direction and dominant wind direction as well. Finally, an aerosol transport and deposition model would have to consider that the salts may frequently be entering the package as deliquesced or partially deliquesced droplets. An aerosol transport model must therefore capture the changes in mass and aerodynamic properties as the particles rise and dry out in the heated annulus of the overpack. The deposition model should consider the changes in the sticking properties of the particles, as they transition from brine droplets to dry salts. Aerosol particles impacting the canister near the inlet vent may still be partially deliquesced, resulting in build-up of salts at that location.

Any deposition model must also explain the greater rates of deposition on the canister tops. It should be noted that during sampling at Hope Creek, *Phragmites* grass seeds were observed in large amounts on the canister top. Surface stains and variations in the amount of accumulated dust (dunes) were also observed, suggesting that materials and rainwater may be regularly blown onto the canister tops through the outlet vents, an additional complicating factor.

It is important to remember that the canisters at Hope Creek and at Diablo Canyon are of similar type and geometry. In both cases, there are four outlet air vents at 90º from each other around the top of the overpack. These vents are offset 45º degrees from the inlet vents at the base of the units. Because the dust sampling was performed in a vertical line extending downward from the outlet vents, regions near the inlet vent were not sampled. It is possible that there is preferential deposition of salts near the inlet vents, especially if the salts enter the inlet vents as deliquesced droplets. We have no information on the surface deposits near the inlet vents.

A limited set of analyses were presented here. A complete suite of SEM images and EDS maps of samples from the Hope Creek and Diablo Canyon canisters is provided in *Analysis of Dust Samples Collected from Spent Nuclear Fuel Interim Storage Containers at Hope Creek, Delaware, and Diablo Canyon, California,* SAND2014-16383 (Bryan and Enos 2014).

2.4.2 XRF Analysis

XRF analysis was used to quantify element concentrations on the pads. The XRF was capable of mapping the filters and pads with a resolution of 100 µm, providing spatial compositional information on the scale of the filters. This information provides a link between the SEM data, which is confined to small areas on the sample surface, and the chemical analysis, which does not discriminate spatially, but rather provides an averaged composition for all the phases present. Moreover, the analysis provides element ratios which may be useful in estimating concentrations of some insoluble elements.

Relative to previous work with samples from Calvert Cliffs (Enos et al. 2013), the XRF instrument used here had lower sensitivity. This meant needing to count longer for each spatial position in the XRF map, selecting smaller map regions and increasing the step width (to ~100 mm) which decreased resolution for the measurement. Also, the samples did not appear to have as much residue on them as the previous samples from Calvert Cliffs, so the detection of material posed further difficulties. Finally, the pads used for the Hope Creek and Diablo Canyon sampling contained many elements that are commonly found in potential dust minerals, namely silicon, magnesium and, iron.

The low signal issue was addressed by comparing the full spectrum obtained on each sample to that of a clean, unused pad. Blank subtraction was performed to look for residual intensity that possibly could be assigned to residue on the sample. This method appears to work reasonably for qualitative assessment of material present on these pads. For each XRD pattern, a qualitative analysis is provided. It is important to note, when evaluating the XRF patterns provided in this report, that peak heights do not correspond to elemental abundances, but rather are a function of varying detection efficiencies as a function of wavelength.

The XRF results for a few representative samples are shown here. In each case, the raw XRF pattern is shown, as well as a blank-subtracted XRF pattern, to emphasize the differences between the samples and the blank.

<u>Blanks</u>. The XRF pattern and qualitative analysis results for the pad blank are shown in Figure 30. Although the pad was intended to be mineral-free, it actually contained talc ($Mg_3Si_4O_{10}(OH)_2$ as a filler material. This resulted in large Mg and Si peaks in the blank, and large estimated concentrations of Mg and Si in the blank pad (red boxes in Figure 30). Other compounds present in the pad include Ti, which is probably present in the oxide form as a white pigment, Ca, P, and S. All of these elements contribute to the measured XRD signal, but not all can be leached from the pad. The Mg, Si, Fe, Ti, and Ca appear to be sequestered in insoluble compounds in the pad. However, PO_4, SO_4, and Na leach from the pad in large concentrations and interfere with measurement of these elements in the dust soluble fractions

leached from the pads. Note that Na does not appear in the X-ray spectrum because of the low sensitivity of the method for this element.

Canister side samples. For both Hope Creek and Diablo Canyon, the dust loads on samples from the sides of the canisters were very light, and the XRF patterns and analyses varied little from the blank. Typically only Fe and Si were enriched relative to the blank. An example pattern for the lightly-coated canister side samples is represented by Hope Creek sample 144-005 (collected 13.5 feet below the upper edge of the canister) in Figure 31. The initial X-ray spectrum was similar to the blank spectrum. Following blank subtraction, only Fe was detected in the sample.

Canister top samples. For samples from the tops of the canisters, where the salt loads are higher, there is a clear X-ray contribution from the dust on the filters. Results for Hope Creek sample 144-011 are shown in Figure 32. Relative to the blank, several elements are significantly enriched, including Fe, Si, Zn, Ca, K, and S. The enrichment in Fe is consistent with the SEM observations of abundant stainless steel particles and Fe-oxides in the dust; and that of Si is consistent with the observations of abundant quartz and aluminosilicate minerals. Although Zn-rich particles, possibly from the paint on the outside of the overpacks, were only rarely observed, they are apparently the source of the Zn X-ray peak shown here. Minerals containing Ca, K, and S (as sulfate) were observed by SEM, and these elements comprise a large fraction of the soluble salts extracted from the pads (Section 3.3). These results are typical for the Hope Creek canister top samples.

XRF analysis results for sample #123-011, a representative canister top sample from Diablo Canyon, are shown in Figure 33. Relative to the blank, the Diablo Canyon sample is enriched in Fe, Si, Zn, Ca, K, S, and Cl. In some other Diablo Canyon samples, peaks for Cr were also present. As with the Hope Creek samples, this is largely consistent with the phases identified in the dust by SEM. Given the prevalence of sea-salt aggregates, one might expect to see peaks for Mg and Na as well; however, the method sensitivity for Mg is low, and for Na, very low. The detection of Cl and Zn, and of Cr in some other samples from Diablo Canyon, is definitive, because these elements do not occur in the blank.

Because many of the elements that were detected in the canister top samples from Hope Creek and Diablo canyon are present in relatively high amounts in the blank, caution must be taken in interpreting these results. False positive detections may occur because of variations in sample geometry, and the canister top collection sponges are thicker than the ones used for the canister sides—the additional compression (and concomitant densification) of the canister top sample sponges required during loading into the XRF may be responsible for the observed enrichments in the elements that are present in the pad matrix. Also, there are variations in the amount of resin/filler through the thickness of the original Scotch-Brite™ abrasive pads that were sectioned and thinned to make the sample pads. It is unlikely that the same side of the original pad was used to make all of the sampling pads and the blanks, or that the same face of each trimmed sampling pad was used during sampling and analysis. Hence, some of the variation in the contribution of the pads is almost certainly due to variations in the amount of binder/filler present. As will be discussed in Section 2.4.3, this conclusion is supported by the compositions of soluble salts leached from the dry pads samples.

The results of the XRF analysis of the sponges are summarized in Table 7 for Hope Creek, and in Table 8 for Diablo Canyon. The enrichment in Fe relative to the blank in all samples from the canister surface may be real, as the SEM analyses show that steel particles were abundant components of the dust in almost all cases. Moreover, the detection of Cr is some samples from Diablo Canyon is strong evidence that that the stainless steel particles in the dust are contributing to the X-ray signal. Similarly, the enrichment of Si in most samples may reflect a contribution from the dust. However, given the variability in the pad matrices, it is not possible to clearly attribute a portion of the signal for any component to the dust unless it is not present at all in the blank.

To conclude, XRF analysis of the dry pad samples was complicated by the presence of several elements in the blank, and by differences in pad resin/filler content. It is clear that some elements, however, represent dust collected from the canister surfaces. Detection of Zn on the Hope Creek pads, and Zn, Cl, and Cr on the Diablo Canyon pads, must represent components in the dust, as these are not present in the blank. It is likely that at least some of the enrichments observed in other elements, such as Fe and Si, are also in part due to dust on the pads.

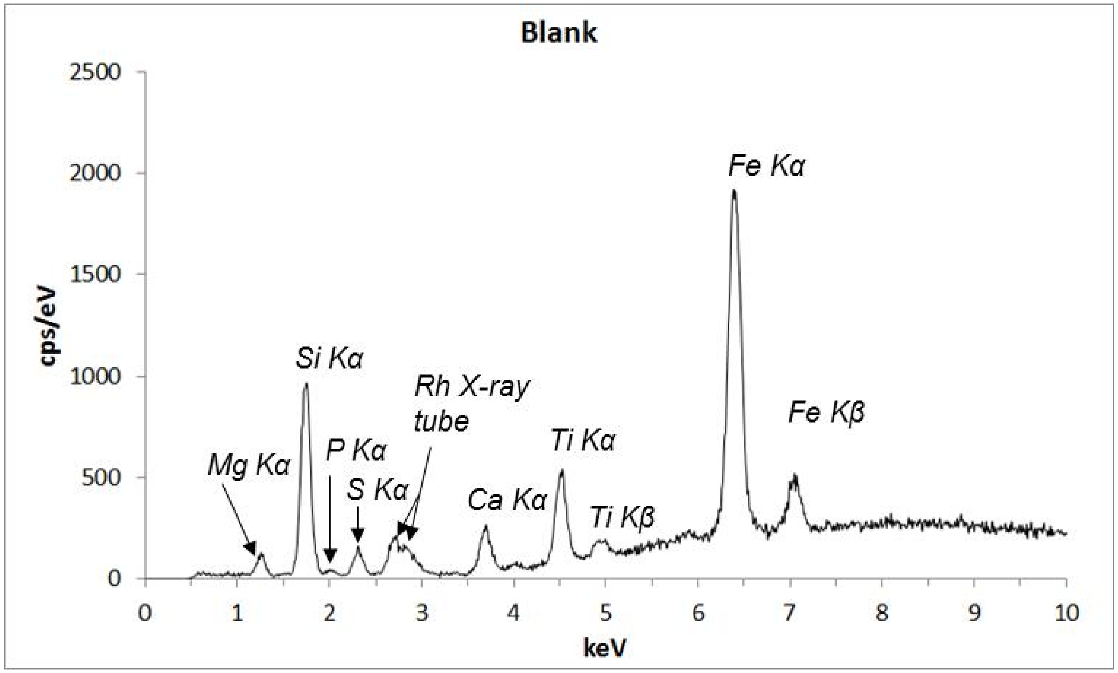

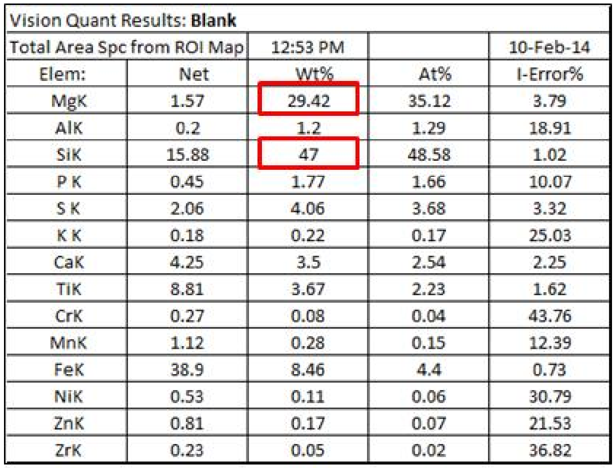

Vision Quant Results: **Blank**				
Total Area Spc from ROI Map		12:53 PM		10-Feb-14
Elem:	Net	Wt%	At%	I-Error%
MgK	1.57	29.42	35.12	3.79
AlK	0.2	1.2	1.29	18.91
SiK	15.88	47	48.58	1.02
P K	0.45	1.77	1.66	10.07
S K	2.06	4.06	3.68	3.32
K K	0.18	0.22	0.17	25.03
CaK	4.25	3.5	2.54	2.25
TiK	8.81	3.67	2.23	1.62
CrK	0.27	0.08	0.04	43.76
MnK	1.12	0.28	0.15	12.39
FeK	38.9	8.46	4.4	0.73
NiK	0.53	0.11	0.06	30.79
ZnK	0.81	0.17	0.07	21.53
ZrK	0.23	0.05	0.02	36.82

Elemental map for Fe

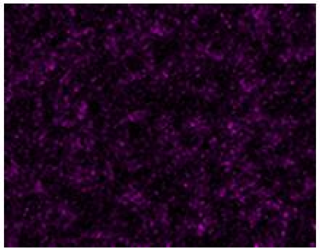

Figure 30. XRF pattern and XRF qualitative analysis results for the pad blank.

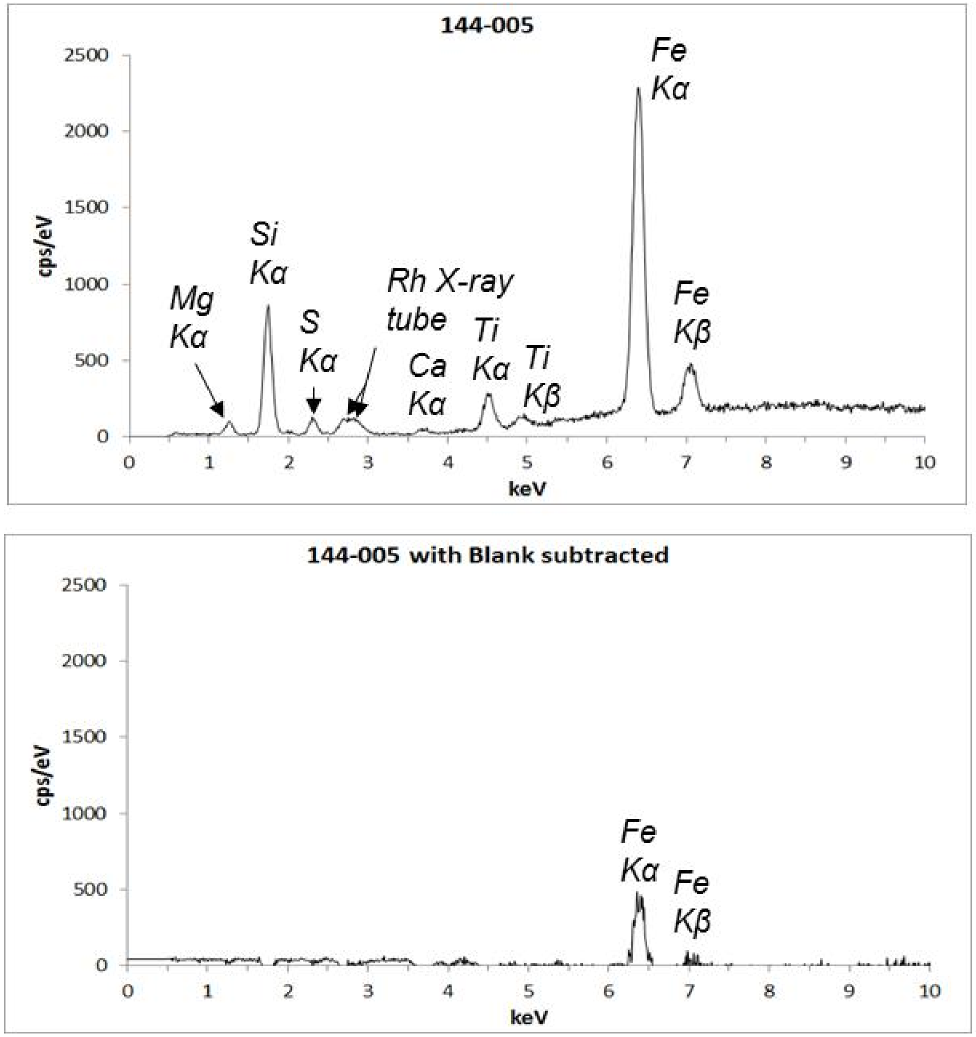

Vision Quant Results: 144-005				
Total Area Spc from ROI Map	2:04 PM			11-Feb-14
Elem:	Net	Wt%	At%	I-Error%
MgK	1.27	29	34.98	4.35
AlK	0.1	0.72	0.79	34.75
SiK	13.4	46.39	48.44	1.11
P K	0.32	1.46	1.39	12.82
S K	1.71	3.9	3.57	3.66
ClK	1.14	2.57	2.13	4.88
K K	0.17	0.25	0.19	23.98
CaK	0.62	0.6	0.44	8.46
TiK	4.8	2.2	1.35	2.26
CrK	0.54	0.17	0.09	18.27
MnK	0.64	0.17	0.09	17.98
FeK	49.14	12	6.3	0.61
NiK	0.56	0.15	0.07	24.74
ZnK	1.26	0.32	0.14	12.11
ZrK	0.3	0.08	0.03	26.5

Vision Quant Results: **Blank**				
Total Area Spc from ROI Map	12:53 PM			10-Feb-14
Elem:	Net	Wt%	At%	I-Error%
MgK	1.57	29.42	35.12	3.79
AlK	0.2	1.2	1.29	18.91
SiK	15.88	47	48.58	1.02
P K	0.45	1.77	1.66	10.07
S K	2.06	4.06	3.68	3.32
K K	0.18	0.22	0.17	25.03
CaK	4.25	3.5	2.54	2.25
TiK	8.81	3.67	2.23	1.62
CrK	0.27	0.08	0.04	43.76
MnK	1.12	0.28	0.15	12.39
FeK	38.9	8.46	4.4	0.73
NiK	0.53	0.11	0.06	30.79
ZnK	0.81	0.17	0.07	21.53
ZrK	0.23	0.05	0.02	36.82

Figure 31. XRF pattern and XRF qualitative analysis results for Hope Creek sample 144-005, from the side of the canister.

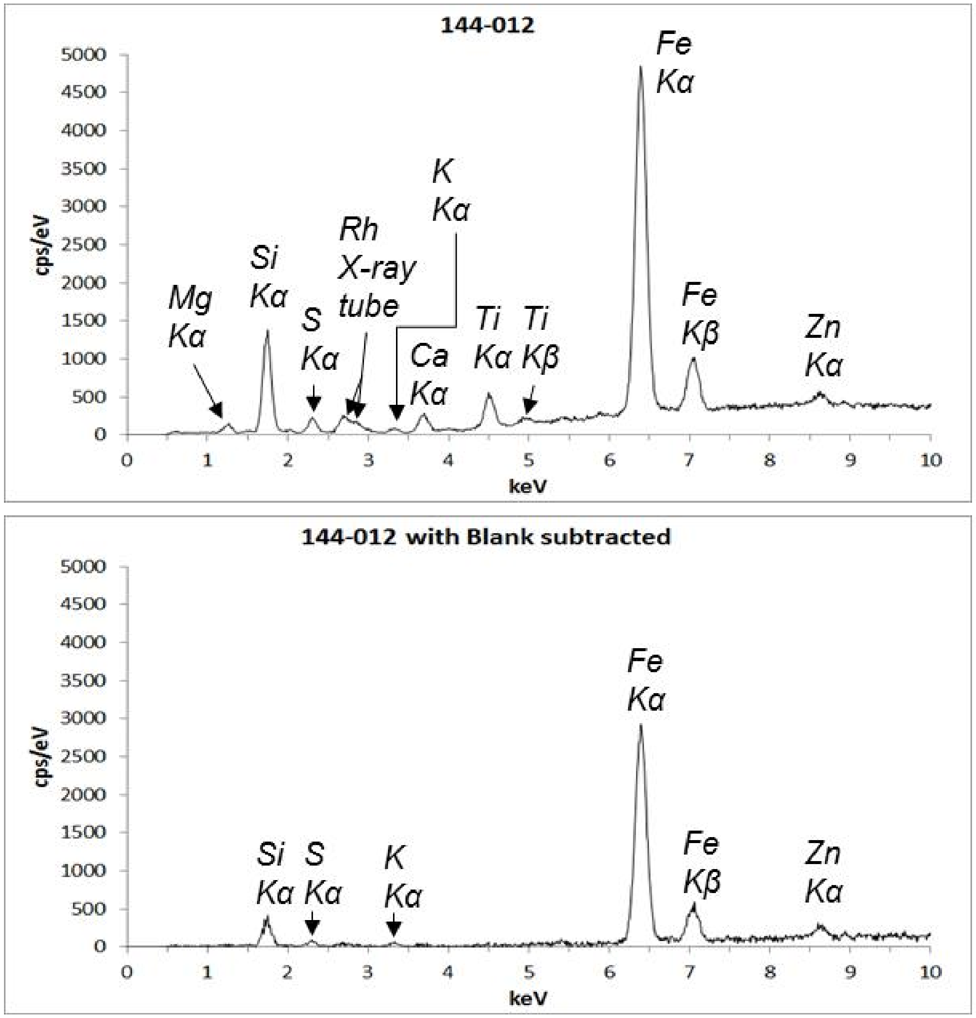

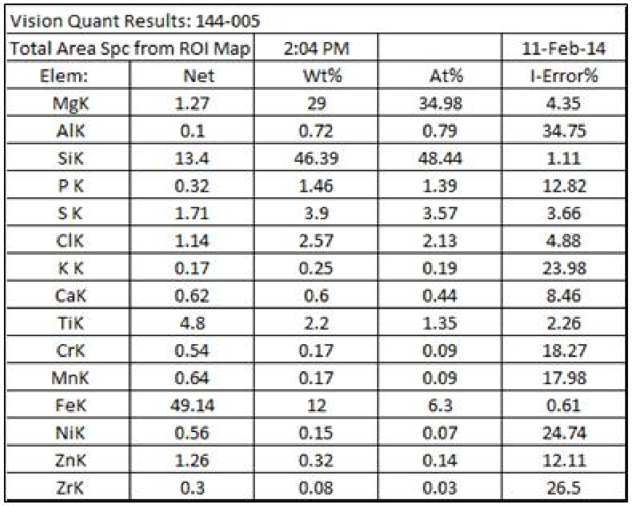

Vision Quant Results: 144-005				
Total Area Spc from ROI Map		2:04 PM		11-Feb-14
Elem:	Net	Wt%	At%	I-Error%
MgK	1.27	29	34.98	4.35
AlK	0.1	0.72	0.79	34.75
SiK	13.4	46.39	48.44	1.11
P K	0.32	1.46	1.39	12.82
S K	1.71	3.9	3.57	3.66
ClK	1.14	2.57	2.13	4.88
K K	0.17	0.25	0.19	23.98
CaK	0.62	0.6	0.44	8.46
TiK	4.8	2.2	1.35	2.26
CrK	0.54	0.17	0.09	18.27
MnK	0.64	0.17	0.09	17.98
FeK	49.14	12	6.3	0.61
NiK	0.56	0.15	0.07	24.74
ZnK	1.26	0.32	0.14	12.11
ZrK	0.3	0.08	0.03	26.5

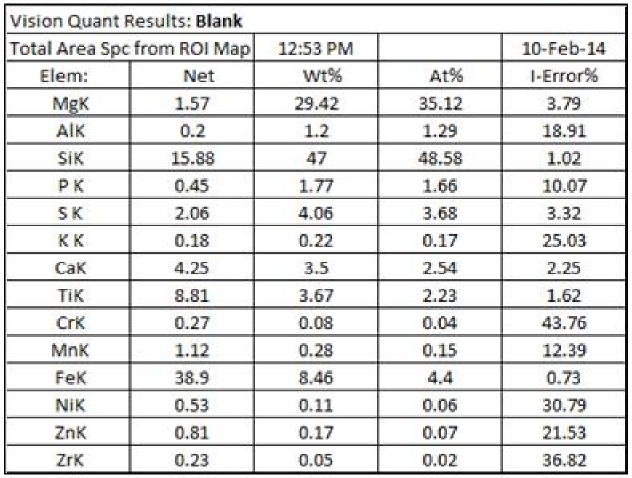

Vision Quant Results: **Blank**				
Total Area Spc from ROI Map		12:53 PM		10-Feb-14
Elem:	Net	Wt%	At%	I-Error%
MgK	1.57	29.42	35.12	3.79
AlK	0.2	1.2	1.29	18.91
SiK	15.88	47	48.58	1.02
P K	0.45	1.77	1.66	10.07
S K	2.06	4.06	3.68	3.32
K K	0.18	0.22	0.17	25.03
CaK	4.25	3.5	2.54	2.25
TiK	8.81	3.67	2.23	1.62
CrK	0.27	0.08	0.04	43.76
MnK	1.12	0.28	0.15	12.39
FeK	38.9	8.46	4.4	0.73
NiK	0.53	0.11	0.06	30.79
ZnK	0.81	0.17	0.07	21.53
ZrK	0.23	0.05	0.02	36.82

Figure 32. XRF pattern and XRF qualitative analysis results for Hope Creek sample 144-011, from the top of the canister.

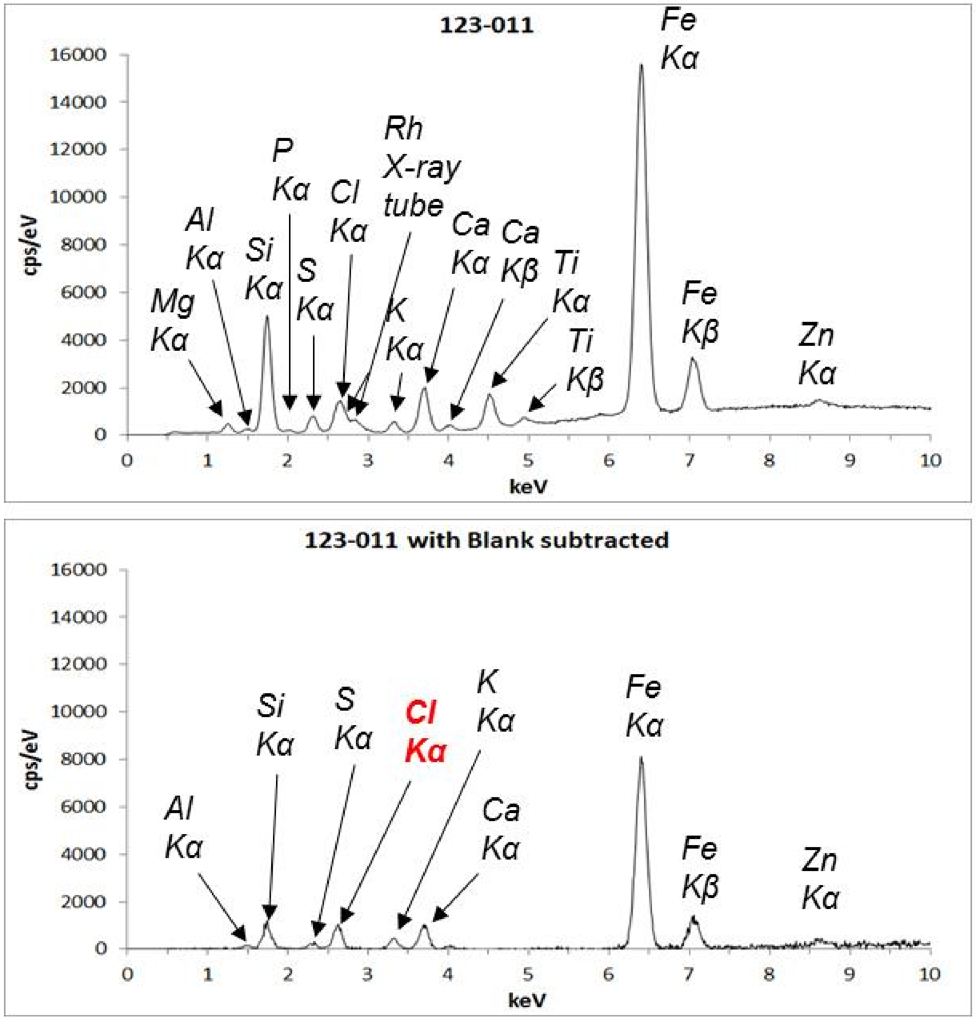

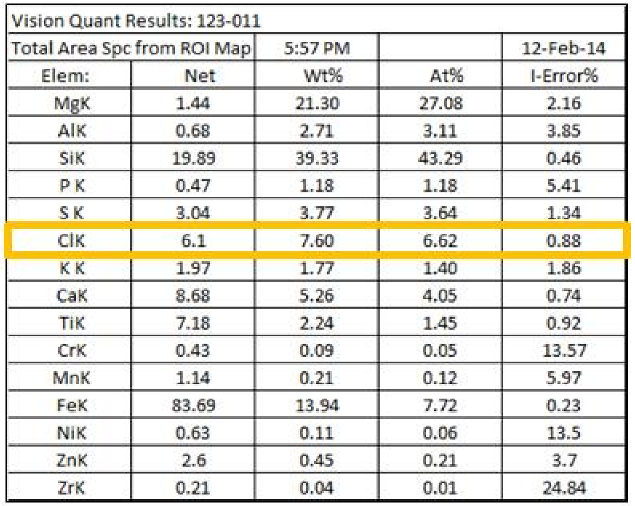

Vision Quant Results: 123-011				
Total Area Spc from ROI Map	5:57 PM			12-Feb-14
Elem:	Net	Wt%	At%	I-Error%
MgK	1.44	21.30	27.08	2.16
AlK	0.68	2.71	3.11	3.85
SiK	19.89	39.33	43.29	0.46
P K	0.47	1.18	1.18	5.41
S K	3.04	3.77	3.64	1.34
ClK	6.1	7.60	6.62	0.88
K K	1.97	1.77	1.40	1.86
CaK	8.68	5.26	4.05	0.74
TiK	7.18	2.24	1.45	0.92
CrK	0.43	0.09	0.05	13.57
MnK	1.14	0.21	0.12	5.97
FeK	83.69	13.94	7.72	0.23
NiK	0.63	0.11	0.06	13.5
ZnK	2.6	0.45	0.21	3.7
ZrK	0.21	0.04	0.01	24.84

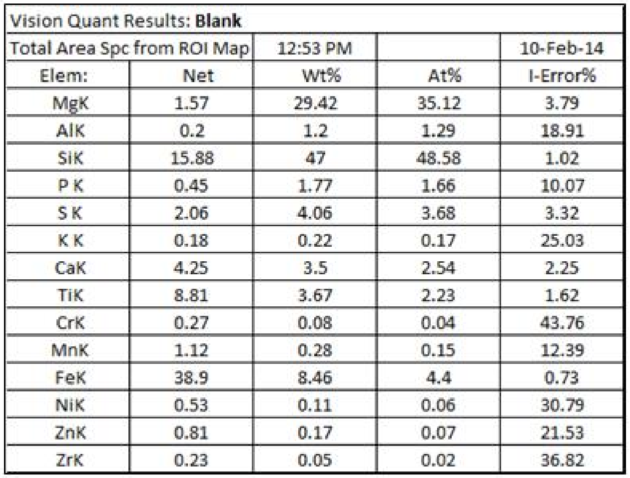

Vision Quant Results: **Blank**				
Total Area Spc from ROI Map	12:53 PM			10-Feb-14
Elem:	Net	Wt%	At%	I-Error%
MgK	1.57	29.42	35.12	3.79
AlK	0.2	1.2	1.29	18.91
SiK	15.88	47	48.58	1.02
P K	0.45	1.77	1.66	10.07
S K	2.06	4.06	3.68	3.32
K K	0.18	0.22	0.17	25.03
CaK	4.25	3.5	2.54	2.25
TiK	8.81	3.67	2.23	1.62
CrK	0.27	0.08	0.04	43.76
MnK	1.12	0.28	0.15	12.39
FeK	38.9	8.46	4.4	0.73
NiK	0.53	0.11	0.06	30.79
ZnK	0.81	0.17	0.07	21.53
ZrK	0.23	0.05	0.02	36.82

Figure 33. XRF pattern and XRF qualitative analysis results for Diablo Canyon sample 123-011, from the top of the canister.

Table 7. XRF Analysis of Hope Creek Dry Pad Samples—Elemental Enrichments Relative to the Blank Sample.

Sample	Location	Fe	Si	Ca	K	S	Zn
144-001	Unknown	minor	–	–	–	–	–
144-002	Unknown	–	–	–	–	–	–
144-005	Canister side	minor	–	–	–	–	–
144-006	Canister side	minor	trace	–	–	–	–
144-007	Canister side	trace	–	–	–	–	–
144-011	Canister top	major	minor	trace	trace	trace	trace
144-012	Canister top	major	minor	trace	trace	–	trace
145-001	Unknown	trace	–	–	–	–	–
145-003	Canister side	major	minor	–	–	–	–
145-004	Canister side	minor	minor	–	–	–	–
145-005	Canister side	minor	minor	–	–	–	–
145-012	Canister top	minor	trace	trace	trace	–	trace

Table 8. XRF Analysis of Diablo Canyon Dry Pad Samples—Elemental Enrichments Relative to the Blank Sample.

Sample	Location	Fe	Si	Ca	K	S	Zn	Cl	Cr	Ti
123-001	Unknown	major	minor	–	–	trace	–	–	–	–
123-006	Canister side	minor	minor	–	–	trace	–	–	–	–
123-007	Unknown	minor	minor	–	–	trace	–	–	–	–
123-008	Canister side	minor	trace	–	–	–	–	–	–	–
123-009	Canister side	major	minor	–	–	trace	–	–	–	–
123-011	Canister top	major	minor	trace	trace	trace	trace	–	–	minor
123-012	Canister top	minor	trace	–	minor	trace	trace	minor	minor	–
170-001	Unknown	major	trace	–	–	–	–	–	–	–
170-003	Canister top	major	minor	–	trace	trace	trace	minor	–	–
170-004	Canister side	major	minor	–	–	trace	trace	–	trace	–
170-005	Canister side	minor	minor	–	–	trace	trace	–	–	–
170-006	Canister side	major	minor	–	–	trace	trace	–	–	–

2.4.3 Chemical Analysis

The methods used for chemical analysis of the SaltSmart™ and dry pad samples from Hope Creek and Diablo Canyon are described in Section 2.2. As discussed in that section, the soluble salts extracted from the SaltSmart™ sensors and from the dry pads were analyzed. Because of the very light dust load on most pads, and the high degree of contamination by talc, a decision was made not to perform bulk analyses of the insoluble residues from the dry pads. The results of the analyses are presented and discussed below.

2.4.3.1 Hope Creek Samples

<u>SaltSmart™ Sensors</u>

Thirteen SaltSmart™ sensors were analyzed from the Hope Creek site, representing three samples from the side of each of the two containers sampled, and one or two from the top of each. Concentrations of soluble salts were generally quite low. Two samples of unknown origin were also analyzed from each canister. The amounts of each ionic species present in µg per sample are given in Table 9. Values in micro-equivalents (µEq) are provided in Table 10, along with the calculated charge balance errors. Also shown in these tables are three SaltSmart™ blanks run at Sandia, two with contact times of 8 minutes, and one with a contact time of 15 minutes. In addition, the 15 minute sample was stored approximately one week prior to analysis, to assess whether anything leached out of the SaltSmart™ components over time. There are several notable points. First, the salt loads are generally very light (≤25 µg/sample) for the sensors used on the sides of the storage container. Only the three samples from the canister tops (144-013, 144-014, and 145-013) have significant amounts of salt. The dominant cation in all cases was Ca, but Mg and Na are also abundant in the higher-concentration samples. Sulfate was the dominant anion in all samples, and nitrate was the second most abundant in all samples except for 144-014, for which chloride was the second most abundant.

Many of the charge balances are poor, and consistently indicate an anion deficiency. There are three possible reasons for this:

- Analytical uncertainties are high because of the very low salt concentrations. However, the consistent anion deficiency would suggest an analytical bias, not just analytical scatter.
- The ammonium data are suspect. Ammonium concentrations are low in terms of µg/sample, but ammonium has a low atomic mass, and the low values correspond to a significant fraction of the measured µEq of cations in most samples. Ammonium concentrations in the Hope Creek samples are similar to the concentrations observed in the blanks; in fact, they are always lower than the value for the 15 minute blank. During disassembly of the sensors, it was noted that silicone cement is used to seal the back of the sensors, where the flat film containing the electrodes exits the sensor. Since many silicone cements degas ammonia during curing, this material may be a source of the observed ammonium in the blanks. Reaction of ammonia with water in the sensor would produce ammonium and hydroxyl, and would contribute to the poor charge balances, because hydroxyl was not measured.
- Carbonate, a potentially important contributor to the anion total, was not analyzed. Since carbonate minerals were commonly observed in the dust samples by SEM, it is likely that at least a fraction of the charge balance error is due to the lack of data for carbonate.

The charge balance error correlates with the amount of calcium and magnesium present, and is actually largest for the two samples with the highest amounts of salts, for which the effect of ammonium is minimal, and analytical errors should be smallest. Thus, it is likely that the charge balance error is largely due to the presence of carbonate/bicarbonate minerals in the dust, and carbonate accounts for the missing unanalyzed anionic species in the leachate.

The chloride loads per unit surface area are given in Table 11. They are generally less than 10 mg m^{-2}, but the two highest samples, 144-013 and 144-014, get up to 14 and 60 mg m^{-2}, respectively. It should be noted that the concentrations listed here may in some cases underestimate the amount of salt and chloride present. For three samples, the reservoir pad was only partially saturated and it is not clear that sufficient water passed through the wick and across the canister surface to leach off all the soluble salts present. Also, for sample number 145-006, the SaltSmart™ wick apparently did not completely contact the surface; the discoloration on the wick covered only about 1/3 of the total area, so the listed chloride concentration probably underestimates the actual value on the package.

Table 9. Ion Concentrations in the Hope Creek SaltSmart™ Samples (µg/sample).

Sample #	Loc.	Depth, ft	Temp. , °F	Na	K	Ca	Mg	NH_4^+	F^-	Cl^-	NO_3^-	PO_4^{3-}	SO_4^{2-}	SUM
144-008	Side	13.0	93.2	*0.1*	*0.8*	3.4	0.6	2.7	nd	0.9	2.7	nd	4.1	15.4
144-009	Side	7.5	116.5	*0.1*	1.7	4.5	0.5	2.7	nd	0.9	6.4	*1.1*	6.5	24.3
144-010	Side	1.0	133.9	*0.4*	1.4	4.2	0.4	2.4	nd	1.2	5.0	nd	4.4	19.4
144-013	Top	0.0	138	42	18	102	33	2.8	0.4	4.2	19	4.8	91	317
144-014	Top	0.0	141.2	13	6.4	29	8.0	2.7	0.4	18	7.3	1.3	55	142
144-003	G.S.	—	—	nd	*0.6*	2.2	0.4	1.4	nd	*0.5*	3.3	1.2	2.1	11.6
144-004	G.S.	—	—	nd	*0.3*	3.2	0.6	2.9	nd	0.8	1.8	*0.5*	1.7	11.8
145-006*[#]	Side	13.0	70.6	*0.5*	2.2	4.4	0.6	2.3	nd	2.2	8.1	nd	4.7	25.1
145-007	Side	7.5	100.8	*0.7*	1.0	2.4	0.6	2.9	nd	2.1	2.2	*0.7*	5.3	17.9
145-014	Side	1.0	130.3	*0.6*	*0.9*	3.2	0.8	3.2	nd	1.2	2.5	nd	9.1	21.5
145-013**	Top	0.0	174.1	32	15	91	30	2.8	nd	2.2	15	3.5	82	273
145-011*	Blank	—	—	nd	*0.2*	2.3	0.3	3.0	nd	*0.7*	1.3	nd	1.7	9.6
145-002	G.S.	—	—	nd	1.2	4.8	0.5	2.7	nd	*0.7*	5.9	*0.8*	2.0	18.5
SS-Bl-8 min-1	—	—	—	nd	nd	1.3	0.2	1.1	nd	*0.4*	1.6	nd	*0.6*	5.1
SS-Bl-8 min-2	—	—	—	nd	nd	1.2	0.2	1.5	nd	*0.7*	*0.9*	*0.5*	*0.2*	5.2
SS-Bl-15 min	—	—	—	nd	nd	1.5	0.5	5.7	0.2	*0.7*	1.1	1.6	1.7	12.9

Notes: Italicized values in gray were above blank values, but too low to quantify accurately. nd = not detected.

* Reservoir pad only damp
** Reservoir pad only partially saturated
[#] SaltSmart™ wick appears to have only partially contacted the canister surface (~1/3 of the pad).

Table 10. Ion Concentrations in the Hope Creek SaltSmart™ Samples (µEq/sample).

Sample #	Na	K	Ca	Mg	NH_4^+	F^-	Cl^-	NO_3^-	PO_4^{3-}	SO_4^{2-}	Sum, Cation	Sum Anion	Chrg. Bal. Error, %†
144-008	*5.7E-03*	*2.1E-02*	1.7E-01	5.3E-02	1.5E-01	nd	2.6E-02	4.4E-02	nd	8.5E-02	4.0E-01	1.5E-01	44.4
144-009	*4.2E-03*	4.3E-02	2.2E-01	3.8E-02	1.5E-01	nd	2.5E-02	1.0E-01	*3.3E-02*	1.4E-01	4.6E-01	3.0E-01	21.5
144-010	*1.7E-02*	3.7E-02	2.1E-01	3.2E-02	1.3E-01	nd	3.3E-02	8.1E-02	nd	9.2E-02	4.3E-01	2.1E-01	35.1
144-013	1.8E+00	4.6E-01	5.1E+00	2.7E+00	1.5E-01	2.0E-02	1.2E-01	3.1E-01	1.5E-01	1.9E+00	1.0E+01	2.5E+00	61.0
144-014	5.8E-01	1.6E-01	1.4E+00	6.6E-01	1.5E-01	2.1E-02	5.1E-01	1.2E-01	4.0E-02	1.2E+00	3.0E+00	1.8E+00	24.1
144-003	nd	*1.6E-02*	1.1E-01	3.1E-02	7.7E-02	nd	*1.4E-02*	5.4E-02	3.8E-02	4.3E-02	2.3E-01	1.5E-01	22.3
144-004	nd	*8.1E-03*	1.6E-01	5.0E-02	1.6E-01	nd	2.1E-02	2.9E-02	*1.6E-02*	3.6E-02	3.8E-01	1.0E-01	57.7
145-006*#	*2.3E-02*	5.6E-02	2.2E-01	5.3E-02	1.3E-01	nd	6.2E-02	1.3E-01	nd	9.8E-02	4.8E-01	2.9E-01	24.3
145-007	*3.0E-02*	2.7E-02	1.2E-01	4.9E-02	1.6E-01	nd	6.0E-02	3.5E-02	*2.2E-02*	1.1E-01	3.8E-01	2.3E-01	25.5
145-014	*2.6E-02*	*2.3E-02*	1.6E-01	6.2E-02	1.8E-01	nd	3.5E-02	4.0E-02	nd	1.9E-01	4.5E-01	2.6E-01	25.7
145-013**	1.4E+00	3.8E-01	4.5E+00	2.5E+00	1.5E-01	nd	6.3E-02	2.3E-01	1.1E-01	1.7E+00	8.9E+00	2.1E+00	61.8
145-011*	nd	*6.1E-03*	1.1E-01	2.9E-02	1.7E-01	nd	*2.1E-02*	2.1E-02	nd	3.5E-02	3.2E-01	7.6E-02	61.2
145-002	nd	3.0E-02	2.4E-01	4.3E-02	1.5E-01	nd	*1.9E-02*	9.5E-02	*2.4E-02*	4.1E-02	4.6E-01	1.8E-01	44.3
SS-Bl-8 min-1	nd	nd	6.3E-02	1.6E-02	6.2E-02	nd	*1.0E-02*	2.6E-02	nd	*1.2E-02*	1.4E-01	4.9E-02	48.9
SS-Bl-8 min-2	nd	nd	5.9E-02	1.5E-02	8.3E-02	nd	*2.0E-02*	*1.5E-02*	*1.5E-02*	*5.1E-03*	1.6E-01	5.5E-02	48.4
SS-Bl-15 min	nd	nd	7.4E-02	4.0E-02	3.2E-01	1.2E-02	*1.9E-02*	1.8E-02	4.9E-02	3.5E-02	4.3E-01	1.3E-01	52.7

Notes: Italicized values in gray were above blank values, but too low to quantify accurately. nd = not detected.

† Charge balance calculated as ((Cations-Anions)/(Cations + Anions)) × 100
* Reservoir pad only damp
** Reservoir pad only partially saturated
\# SaltSmart™ wick appears to have only partially contacted the canister surface (~1/3 of the pad).

Table 11. Measured Chloride concentrations, in mg m^{-2}, on the Hope Creek Canister Surfaces.

Sample #	**Loc.**	**Depth, ft**	**Temp., °F**	**Cl^{-}, mg/m^{2}**
144-008	Side	13.0	93.2	3.0
144-009	Side	7.5	116.5	2.9
144-010	Side	1.0	133.9	3.9
144-013	Top	0.0	138	14
144-014	Top	0.0	141.2	60
144-003	G.S.	—	—	*1.6*
144-004	G.S.	—	—	2.5
145-006*$^{\#}$	Side	13.0	70.6	7.3
145-007	Side	7.5	100.8	7.1
145-014	Side	1.0	130.3	4.1
145-013**	Top	0.0	174.1	7.5
145-011*	Blank	—	—	*2.5*
145-002	G.S.	—	—	*2.2*
SS-Bl-8 min-1	—	—	—	*1.2*
SS-Bl-8 min-2	—	—	—	*2.3*
SS-Bl-15 min	—	—	—	*2.2*

Notes: Italicized values in gray were above blank values, but too low to quantify accurately.

* Reservoir pad only damp
** Reservoir pad only partially saturated
$^{\#}$ SaltSmart™ wick appears to have only partially contacted the canister surface (~1/3 of the pad).

Dry Pad Samples

Twelve dry pad samples were delivered to Sandia from the two canisters at Hope Creek, and three pad blanks. Two empty sample vials were also supplied as blanks. The amounts of each ionic species present in µg per sample are given in Table 12. Values in micro-equivalents (µEq) are provided in Table 13, along with the calculated charge balance errors.

As shown in Table 12, large quantities of Na$^{+,}$ SO$_4^{2-}$, and PO$_4^{3-}$ leach from the pad matrix, making quantification of these elements in any adhering dust impossible. Leachable amounts of each of these species are in the hundreds of micrograms per sample. If the concentrations of these species are entirely due to leaching from the pads, then the concentration of each should vary with the mass of the pad sample. While each of these species shows a strong trend with pad mass, there is significant scatter. The scatter could be due to contributions from dust, but is more likely due to variations in the pad matrix as discussed in Section 3.2. To address this, rather than plotting species concentrations against mass, it is more useful to plot them against PO_4^{3-}, a species that is unlikely to be present in the dust in any significant quantities (unlike Na^+ and SO_4^{2-}). These plots are shown in Figure 34. If the species is dominantly from the pad, then the blanks and samples should form a linear trend versus PO_4^{3-}, intersecting the origin of the plot. If the species is in the dust, or has a significant contribution from the dust, then it will not show a clear linear trend. There will still be a general increase in species concentration with PO_4^{3-}, however, because the larger sample pads were used on the canister tops and were more heavily loaded with dust. Examining the graphs, it is clear that, in addition to Na^+, SO_4^{2-}, and PO_4^{3-}, NH_4^+ is also leaching from the pads, and for all four of these, any contribution from the dust is negligible. K^+ and Mg^{2+} display weak trends, and may be partially derived from the pad. Other species such as Ca^{2+}, Cl^-, and NO_3^-, show no trend; these must be largely sourced to the dust.

Charge balance errors for the dry pad soluble salt analyses are generally less than a few percent, reflecting the high concentrations of the leachates from the pad matrix, which reduce analytical uncertainty. Moreover, carbonate in the dust cannot contribute significantly to the total, so the lack of carbonate analyses has no effect on the charge balance.

Given the limitation in the data, the dry pad samples offer little additional information than the SaltSmart™ sensors. The soluble components from the pads appear to be less Ca-rich and NO_3-rich than the material extracted from the SaltSmart™ sensors, and possibly contain slightly more Cl^-. However, given the small amounts of dust-derived material extracted from the pads, and the large amount of material leaching from the pads, even these qualitative statements must be viewed with caution.

Table 12. Ion Concentrations in the Hope Creek Dry Pad Samples (µg/sample).

Sample #	**Loc.**	**Depth, ft**	**Temp., ºF**	**Pad wt., g**	**Na**	**K**	**Ca**	**Mg**	**NH_4^+**	**F^-**	**Cl^-**	**NO_3^-**	**PO_4^{3-}**	**SO_4^{2-}**	**SUM**
144-005	Side	13.0	84.1	0.2879	339	6.5	0.20	0.80	12.7	*0.08*	5.3	5.5	384	111	865
144-006	Side	8.5	89.6	0.2990	302	5.5	0.27	0.76	12.3	*0.04*	5.3	4.8	304	89	723
144-007	Side	1.0	126.4	0.3373	316	5.1	*0.18*	0.71	12.0	*0.03*	5.0	5.5	365	107	816
144-011	Top	0.0	132.6	0.5146	544	11.8	1.6	2.3	20.9	*0.06*	8.7	10.9	573	178	1352
144-012	Top	0.0	141.2	0.4086	422	7.0	1.5	1.9	16.2	*0.09*	6.5	4.2	503	145	1107
144-001	G.S.	—	—	0.3083	317	6.7	0.54	0.99	13.2	*0.05*	8.6	12.2	400	121	880
144-002	G.S.	—	—	0.3419	324	5.7	0.72	0.80	11.8	—	—	—	—	—	—
145-003	Side	13.5	70.9	0.3349	344	5.8	0.22	0.87	14.2	*0.03*	4.3	5.7	429	124	927
145-004	Side	8.5	93.3	0.3454	356	5.9	0.22	1.05	14.3	*0.04*	7.8	6.7	435	123	950
145-005	Side	1.5	122.5	0.2985	332	6.3	0.24	0.87	12.9	*0.05*	5.1	9.3	379	116	861
145-012	Top	0.0	172.1	0.5769	582	11.4	1.1	2.5	23.2	*0.09*	7.8	8.4	712	221	1569
145-001	G.S.	—	—	0.3847	360	7.5	*0.17*	0.91	13.6	nd	6.0	5.8	448	129	971
Pad-Blank-1		—	—	0.3060	241	3.0	*0.12*	0.43	8.9	*0.04*	2.1	2.5	303	89	650
Pad-Blank-2	—	—	—	0.3447	269	2.7	*0.14*	0.62	9.9	*0.09*	2.3	1.3	355	103	744
Pad-Blank-3	—	—	—	0.3047	235	2.4	*0.07*	0.35	8.3	*0.06*	1.9	1.5	299	89	638
Vial-Blank-1	—	—	—	—	nd	nd	0.39	nd	0.26	*0.01*	0.29	0.65	nd	nd	1.6
Vial-Blank-2	—	—	—	—	nd	nd	0.24	nd	0.20	nd	0.44	1.3	nd	nd	2.2

Notes: Italicized values in gray were above blank values, but too low to quantify accurately. nd = not detected.

Table 13. Ion Concentrations in the Hope Creek Dry Pad Samples (µEq/sample).

Sample #	**Na**	**K**	**Ca**	**Mg**	**NH$_4^+$**	**F$^-$**	**Cl$^-$**	**NO$_3^-$**	**PO$_4^{3-}$**	**SO$_4^{2-}$**	**SUM Cations**	**SUM Anions**	**Ch. Bal Error, %**
144-005	1.5E+01	1.7E-01	1.0E-02	6.6E-02	7.0E-01	*4.0E-03*	1.5E-01	8.9E-02	1.2E+01	2.3E+00	1.6E+01	1.5E+01	3.3
144-006	1.3E+01	1.4E-01	1.3E-02	6.2E-02	6.8E-01	*1.9E-03*	1.5E-01	7.7E-02	9.6E+00	1.8E+00	1.4E+01	1.2E+01	9.1
144-007	1.4E+01	1.3E-01	*8.9E-03*	5.8E-02	6.7E-01	*1.8E-03*	1.4E-01	8.9E-02	1.2E+01	2.2E+00	1.5E+01	1.4E+01	2.1
144-011	2.4E+01	3.0E-01	7.8E-02	1.9E-01	1.2E+00	*3.2E-03*	2.5E-01	1.8E-01	1.8E+01	3.7E+00	2.5E+01	2.2E+01	6.6
144-012	1.8E+01	1.8E-01	7.4E-02	1.6E-01	9.0E-01	*4.6E-03*	1.8E-01	6.8E-02	1.6E+01	3.0E+00	2.0E+01	1.9E+01	1.2
144-001	1.4E+01	1.7E-01	2.7E-02	8.1E-02	7.3E-01	*2.6E-03*	2.4E-01	2.0E-01	1.3E+01	2.5E+00	1.5E+01	1.6E+01	-2.6
144-002	1.4E+01	1.4E-01	3.6E-02	6.6E-02	6.5E-01	nd	nd	nd	nd	nd	1.5E+01	—	—
145-003	1.5E+01	1.5E-01	1.1E-02	7.1E-02	7.9E-01	*1.6E-03*	1.2E-01	9.3E-02	1.4E+01	2.6E+00	1.6E+01	1.6E+01	-1.2
145-004	1.5E+01	1.5E-01	1.1E-02	8.6E-02	7.9E-01	*2.4E-03*	2.2E-01	1.1E-01	1.4E+01	2.6E+00	1.7E+01	1.7E+01	-0.4
145-005	1.4E+01	1.6E-01	1.2E-02	7.1E-02	7.2E-01	*2.7E-03*	1.4E-01	1.5E-01	1.2E+01	2.4E+00	1.5E+01	1.5E+01	2.4
145-012	2.5E+01	2.9E-01	5.7E-02	2.1E-01	1.3E+00	*4.7E-03*	2.2E-01	1.3E-01	2.2E+01	4.6E+00	2.7E+01	2.7E+01	-0.6
145-001	1.6E+01	1.9E-01	*8.3E-03*	7.5E-02	7.5E-01	nd	1.7E-01	9.4E-02	1.4E+01	2.7E+00	1.7E+01	1.7E+01	-1.1
Pad-Blank-1	1.0E+01	7.7E-02	*6.0E-03*	3.6E-02	4.9E-01	*1.9E-03*	6.0E-02	4.1E-02	9.6E+00	1.8E+00	1.1E+01	1.2E+01	-1.9
Pad-Blank-2	1.2E+01	6.9E-02	*6.7E-03*	5.1E-02	5.5E-01	*4.5E-03*	6.4E-02	2.1E-02	1.1E+01	2.1E+00	1.2E+01	1.3E+01	-4.1
Pad-Blank-3	1.0E+01	6.1E-02	*3.6E-03*	2.9E-02	4.6E-01	*3.1E-03*	5.4E-02	2.4E-02	9.4E+00	1.9E+00	1.1E+01	1.1E+01	-2.7

Notes: Italicized values in gray were above blank values, but too low to quantify accurately. nd = not detected.

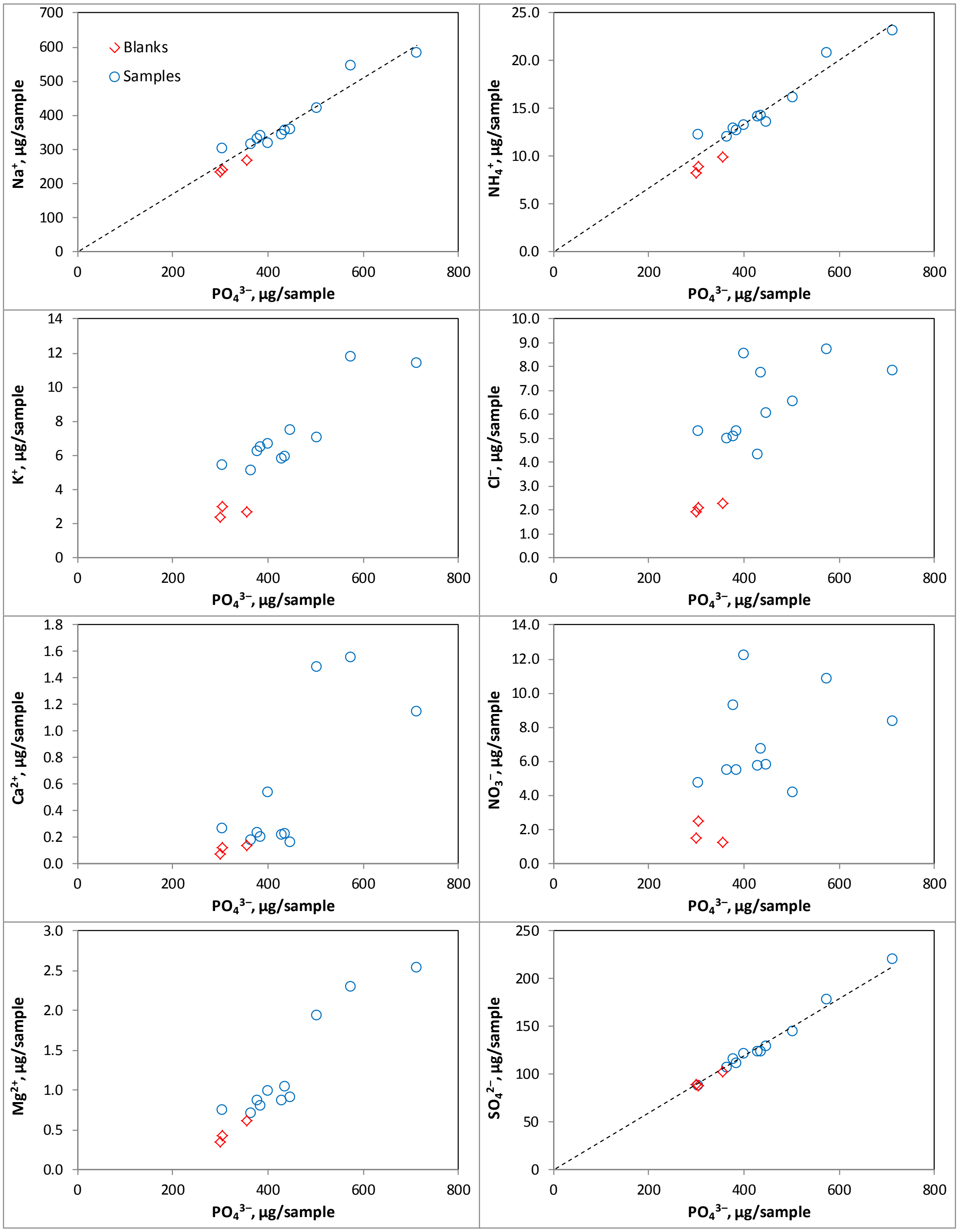

Figure 34. Plots of soluble species concentration versus PO_4^{3-} concentration for the Hope Creek dry pad samples.

2.4.3.2 Diablo Canyon Samples

SaltSmart™ Sensors

Nine SaltSmart™ sensors were analyzed from the Diablo Canyon site, representing three samples each from the sides of the two containers sampled, and three samples of unknown provenance. These canisters were much hotter than the Hope Creek canisters, exceeding the stated operating temperature of the SaltSmart™ sensors (90ºC) in many areas. For this reason, no SaltSmart™ samples were taken from the canister tops, and only a limited portion of the canister sides was sampled. However, as noted previously (Section 2.1), the actual temperature limit for the SaltSmart™ sensors is ~80ºC. Above that temperature, the wicks adhered to the silicone pressure pads behind them, and the reservoir pads inside the sensors were only moist, instead of saturated. It is not clear that the sensors extracted all of the salts from the waste package surface at temperatures above 80ºC, and the results shown here may be underestimates of the salt load on the canister surface.

The amounts of each ionic species present in µg per sample are given in Table 14. Values in micro-equivalents (µEq) are provided in Table 15, along with the calculated charge balance errors. For the samples from the canister sides, the total salt loads were extremely light (<25 µg), in some cases within the range of the blanks. This is not inconsistent with the SEM observations of the pads used for side sampling, but it may also be in part due to poor extraction efficiency at elevated temperatures, as discussed above.

For all of the canister samples, the mass of NO_3^- present exceeded that of Cl^-, and in most cases, Ca^{2+} was more abundant than Na^+. This seems inconsistent with the SEM data, which show abundant sea salt aggregates on the packages (Section 3.2.3); however, for the samples from MPC-123, at least, nitrate was commonly observed on the canister sides, and chloride salts were relatively rare.

For the two samples collected from the gamma shields of the Diablo Canyon canisters, Na^+ was the most abundant cation by mass. Chloride was the most abundant anion on the gamma shield from storage system MPC-123, while nitrate was the most abundant on the gamma shield from system MPC-170. Both gamma shield samples are Ca-rich. This suggests that the dust on the gamma shields contains both sea salts (rich in Na^+, Cl^-, Mg^{2+}, and SO_4^{2-}), and continental salts (rich in NH_4^+, Ca^{2+}, NO_3^-, and SO_4^{2-}).

Also shown in Table 14 and Table 15 are six SaltSmart™ blanks produced at Sandia and run with the Diablo Canyon samples to assess if contact time has any effect on the blanks. The SaltSmart™ blanks were run at contact times of 6, 8, 10, 12, and 14 minutes, and one sample (Blank-8(2)) was aged for 1 week after use and prior to disassembly and analysis, to see if additional materials would leach from the SaltSmart™ components over time. The blanks were all low and showed no compositional trends with contact time or with aging.

As with the Hope Creek SaltSmart™ data, the charge balances for the Diablo Canyon SaltSmart™ samples are poor, and consistently show a deficiency of anions. Once again, this is likely due to the presence of carbonate in the dust, since it was a common phase observed by SEM. As noted for the Hope Creek samples, another potential contributing factor might be ammonia.

Table 16 shows the measured chloride surface loads, in mg m^{-2}. In most cases, the measured chloride loads were <5 mg m^{-2}, in the range of the blanks. Only the samples from the gamma shields, which were collected at ambient temperatures after removal of the shield, showed a significant chloride load. The SEM analyses indicated that the dust loads on the dry pads from the Diablo Canyon canister sides were very light, so it is possible that these low values are correct. However, sea-salt aggregates were abundant in the small amount of dust that was present (Section 3.2.3), and such a small chloride load seems unreasonable. Given the potential issues with the SaltSmart™ sensors at the elevated temperatures of the canister surface (generally >80ºC), the measured salt and chloride loads for the Diablo Canyon samples must be considered questionable.

Table 14. Ion Concentrations in the Diablo Canyon SaltSmart™ Samples (µg/sample).

Sample #	**Loc.**	**Depth, ft**	**Temp., °F**	**Na**	**K**	**Ca**	**Mg**	**NH$_4^+$**	**F$^-$**	**Cl$^-$**	**NO$_3^-$**	**PO$_4^{3-}$**	**SO$_4^{2-}$**	**SUM, µg**
123-003	Side	14.0	119.7	0.30	0.76	2.9	0.73	2.5	0.40	1.4	1.8	*0.51*	5.1	16.4
123-004	Side	11.5	173.4	0.29	1.4	3.2	0.46	1.9	*0.17*	1.1	4.5	*0.15*	2.6	15.8
123-005*	Side	10.5	187.0	nd	0.33	4.5	0.30	1.7	0.35	0.59	0.7	*0.58*	1.7	10.7
123-002	G.S.	—	—	17.7	1.1	7.4	1.1	2.4	1.2	17.4	13.9	nd	12.8	75
123-010	Blank	—	—	4.0	2.3	2.7	0.59	2.8	1.2	7.5	1.6	1.03	2.0	26
170-007*	Side	10.5	177.5	1.2	0.43	2.5	0.31	1.4	0.32	1.3	2.4	nd	1.7	11.6
170-008*	Side	9.5	182.8	0.23	0.62	2.9	0.26	1.8	0.40	0.87	2.8	0.77	0.70	11.4
170-009*	Side	9.0	188.2	0.33	2.8	4.0	0.25	1.3	0.30	0.76	11.5	0.72	1.1	23
170-002	G.S..	—	—	9.0	1.6	7.3	1.6	2.6	*0.27*	4.0	26	0.98	7.6	61
Blank-6	—	—	—	0.88	1.2	2.2	0.23	1.4	*0.10*	1.3	3.9	0.87	0.45	12.5
Blank-8(1)	—	—	—	nd	0.23	1.2	0.15	1.4	0.53	0.42	*0.29*	*0.34*	*0.26*	4.8
Blank-10	—	—	—	*0.01*	0.35	1.5	0.21	1.1	0.38	0.68	2.3	0.97	0.35	7.8
Blank-12	—	—	—	0.33	1.0	1.3	0.19	1.2	*0.26*	1.2	2.2	0.91	0.33	8.9
Blank-14	—	—	—	nd	*0.14*	1.1	0.16	1.2	0.32	0.44	0.92	1.29	*0.23*	5.8
Blank-8(2)	—	—	—	nd	0.26	1.4	0.27	1.0	0.38	0.39	1.3	nd	0.52	5.5

Notes: Italicized values in gray were above blank values, but too low to quantify accurately. nd = not detected.

* Wick adhered to the silicone pressure pad, and reservoir pad only partially saturated

Table 15. Ion Concentrations in the Diablo Canyon SaltSmart™ Samples (µEq/sample).

Sample #	Na	K	Ca	Mg	NH$_4^+$	F$^-$	Cl$^-$	NO$_3^-$	PO$_4^{3-}$	SO$_4^{2-}$	Sum, Cation	Sum Anion	Chrg. Bal. Error, %†
123-003	1.3E-02	2.0E-02	1.4E-01	6.0E-02	1.4E-01	2.1E-02	4.0E-02	2.9E-02	*1.6E-02*	1.1E-01	3.7E-01	2.1E-01	27.3
123-004	1.3E-02	3.6E-02	1.6E-01	3.8E-02	1.1E-01	*9.2E-03*	3.1E-02	7.3E-02	*4.7E-03*	5.3E-02	3.5E-01	1.7E-01	34.8
123-005*	nd	8.4E-03	2.2E-01	2.5E-02	9.5E-02	1.9E-02	1.7E-02	1.1E-02	*1.8E-02*	3.5E-02	3.5E-01	1.0E-01	55.6
123-002	7.7E-01	2.7E-02	3.7E-01	8.6E-02	1.3E-01	6.1E-02	4.9E-01	2.2E-01	nd	2.7E-01	1.4E+00	1.0E+00	14.1
123-010	1.8E-01	5.9E-02	1.4E-01	4.9E-02	1.5E-01	6.1E-02	2.1E-01	2.5E-02	3.3E-02	4.2E-02	5.7E-01	3.7E-01	21.1
170-007*	5.3E-02	1.1E-02	1.2E-01	2.6E-02	8.0E-02	1.7E-02	3.6E-02	3.8E-02	nd	3.6E-02	2.9E-01	1.3E-01	39.6
170-008*	9.8E-03	1.6E-02	1.4E-01	2.1E-02	1.0E-01	2.1E-02	2.4E-02	4.5E-02	2.4E-02	1.5E-02	2.9E-01	1.3E-01	38.8
170-009*	1.5E-02	7.1E-02	2.0E-01	2.1E-02	7.0E-02	1.6E-02	2.2E-02	1.9E-01	2.3E-02	2.3E-02	3.8E-01	2.7E-01	16.6
170-002	3.9E-01	4.2E-02	3.6E-01	1.3E-01	1.4E-01	*1.4E-02*	1.1E-01	4.2E-01	3.1E-02	1.6E-01	1.1E+00	7.3E-01	18.9
Blank-6	3.8E-02	3.0E-02	1.1E-01	1.9E-02	7.8E-02	*5.2E-03*	3.5E-02	6.3E-02	2.8E-02	9.3E-03	2.8E-01	1.4E-01	32.4
Blank-8(1)	nd	5.9E-03	5.8E-02	1.2E-02	7.8E-02	2.8E-02	1.2E-02	*4.7E-03*	*1.1E-02*	*5.4E-03*	1.5E-01	6.1E-02	43.6
Blank-10	*5.6E-04*	8.9E-03	7.6E-02	1.7E-02	6.1E-02	2.0E-02	1.9E-02	3.6E-02	3.1E-02	7.3E-03	1.6E-01	1.1E-01	18.0
Blank-12	1.4E-02	2.6E-02	6.6E-02	1.6E-02	6.9E-02	*1.4E-02*	3.3E-02	3.5E-02	2.9E-02	6.8E-03	1.9E-01	1.2E-01	24.2
Blank-14	nd	*3.6E-03*	5.5E-02	1.3E-02	6.6E-02	1.7E-02	1.3E-02	1.5E-02	4.1E-02	*4.8E-03*	1.4E-01	9.0E-02	21.1
Blank-8(2)	nd	6.6E-03	7.2E-02	2.2E-02	5.7E-02	2.0E-02	1.1E-02	2.0E-02	nd	1.1E-02	1.6E-01	6.2E-02	43.7

Notes: Italicized values in gray were above blank values, but too low to quantify accurately. nd = not detected.

* Wick adhered to the silicone pressure pad, and reservoir pad only partially saturated

Table 16. Measured Chloride concentrations, in mg m^{-2}, on the Diablo Canyon Canister Surfaces.

Sample #	Loc.	Depth, ft	Temp., °F	Cl^{-}, mg/m^2
123-003	Side	14.0	119.7	4.8
123-004	Side	11.5	173.4	3.6
123-005*	Side	10.5	187.0	2.0
123-002	G.S.	—	—	58
123-010	Blank	—	—	25
170-007*	Side	10.5	177.5	4.2
170-008*	Side	9.5	182.8	2.9
170-009*	Side	9.0	188.2	2.5
170-002	G.S.	—	—	13
Blank-6	—	—	—	4.2
Blank-8(1)	—	—	—	1.4
Blank-10	—	—	—	2.3
Blank-12	—	—	—	3.8
Blank-14	—	—	—	1.5
Blank-8(2)	—	—	—	1.3

Notes: Italicized values in gray were above blank values, but too low to quantify accurately.

* Wick adhered to the silicone pressure pad, and reservoir pad only partially saturated

Dry Pad Samples

Twelve dry pad samples were delivered to Sandia from the two canisters at Diablo Canyon. While the SaltSmart™ sampling was limited by high canister surface temperatures, the dry pads are not temperature-sensitive. Therefore, the entire vertical extents of the canister sides were sampled, and samples were taken from the canister tops as well. The compositions of the leachates for each sample, in µg per sample are given in Table 17. Values in µEq are provided in Table 18, along with the calculated charge balance errors.

As with the Hope Creek samples, the Diablo Canyon dry pad samples were affected by large quantities of Na^{+}, SO_4^{2-}, and PO_4^{3-} leaching from the pad matrix, making quantification of these elements in any adhering dust impossible. Once again, we can plot each species against the concentration of PO_4^{3-} to assess whether there is any significant contribution from the dust (Figure 35). The species Na^{+}, SO_4^{2-}, and PO_4^{3-}, and NH_4^{+} are clearly derived from the pad matrix, while K^{+} and Mg^{2+} appear to be partially derived from the pad, but also to have a dust contribution, especially at the higher concentrations; Cl^{-} and NO_3^{-} do not appear to have a contribution from the pads.

Although the soluble salts are strongly affected by the effect of leaching from the pads, it is clear that both Cl^{-} and NO_3^{-} are enriched in all the samples relative to the blanks, and must be present in significant amounts in the dust. Moreover, samples from the tops of the canisters (the three points falling well above the trends in Figure 35) show the greatest enrichment in these species, reflecting the higher dust load on these samples. Ca, Mg, and K are also significantly enriched in the canister top samples, falling above the trends in Figure 35. Because sea-salts were commonly observed in the SEM analyses, we can infer that some fraction of the Na and SO_4 concentrations is also from the dust; however, any dust contribution to these species is insignificant relative to that of the pads, and these samples do not deviate significantly from the trend defined by the pad releases.

The soluble salt data from the pads confirm that chloride-rich salts are present on the canister surfaces, but cannot be used to quantify the amount of chloride present, because the efficiency of the pads with respect to dust collection is not known.

As with the Hope Creek samples, charge balance errors for the leachate analyses from the dry pad samples are generally less than a few percent, reflecting the high concentrations of the pad leachates, which reduce analytical uncertainty. Moreover, dust components comprise too small a fraction of the total ion load to affect the charge balance, even if unmeasured species such as carbonate are present in the dust.

Table 17. Ion Concentrations in the Diablo Canyon Dry Pad Samples (µg/sample).

Sample #	Loc.	Depth, ft	Temp., ºF	Pad wt., g	Na	K	Ca	Mg	NH_4^+	F^-	Cl^-	NO_3^-	PO_4^{3-}	SO_4^{2-}	SUM, µg
123-006	Side	11.0	177.2	0.4151	439	7.7	0.2	1.3	18.2	0.19	9.4	9.3	535	158	1179
123-008	Side	7.5	211.7	0.4837	519	8.8	0.3	1.4	22	0.18	10.4	9.1	619	171	1362
123-009	Side	3.0	245.5	0.5119	518	8.6	0.7	1.8	22	0.18	12.9	9.4	656	172	1401
123-011	Top	0.0	206.8	0.6222	676	13.7	1.9	4.0	24	0.18	74	21.5	732	236	1784
123-012	Top	0.0	204.0	0.5798	638	15.3	1.3	3.3	24	0.16	79	17.4	693	217	1690
123-001	G.S.	—	—	0.4765	485	7.5	0.2	1.3	19.5	0.14	16.7	11.3	579	173	1294
123-007	Blank	—	—	0.4518	478	9.0	0.2	1.4	20	0.16	11.4	9.1	581	168	1278
170-004	Side	11.0	153.9	0.4497	492	8.5	*0.2*	1.1	21	0.22	10.3	6.1	583	168	1291
170-005	Side	7.5	193.8	0.5594	616	9.9	0.5	2.2	26	0.26	8.2	7.9	754	225	1651
170-006	Side	3.0	180.6	0.5305	596	9.2	0.3	2.1	26	0.23	5.7	6.3	nd	202	849
170-003	Top	0.0	187.6	0.6155	710	12.7	0.8	3.5	29	0.22	67	11.5	818	253	1907
170-001	G.S.	—	—	0.5760	597	10.2	0.4	2.1	24	0.15	9.1	29.1	716	205	1594
Pad-Blank-1	—	—	—	0.3060	241	3.0	*0.12*	0.43	8.9	*0.04*	2.1	2.5	303	89	650
Pad-Blank-2	—	—	—	0.3447	269	2.7	*0.14*	0.62	9.9	*0.09*	2.3	1.3	355	103	744
Pad-Blank-3	—	—	—	0.3047	235	2.4	*0.07*	0.35	8.3	*0.06*	1.9	1.5	299	89	638

Notes: Italicized values in gray were above blank values, but too low to quantify accurately. nd = not detected.

Table 18. Ion Concentrations in the Diablo Canyon Dry Pad Samples (μEq/sample).

Sample #	**Na**	**K**	**Ca**	**Mg**	**NH_4^+**	**F^-**	**Cl^-**	**NO_3^-**	**PO_4^{3-}**	**SO_4^{2-}**	**SUM Cations**	**SUM Anions**	**Ch. Bal Error, %**
123-006	1.9E+01	2.0E-01	1.0E-02	1.1E-01	1.0E+00	1.0E-02	2.6E-01	1.5E-01	1.7E+01	3.3E+00	2.0E+01	2.1E+01	-0.4
123-008	2.3E+01	2.3E-01	1.3E-02	1.2E-01	1.2E+00	9.3E-03	2.9E-01	1.5E-01	2.0E+01	3.6E+00	2.4E+01	2.4E+01	1.1
123-009	2.3E+01	2.2E-01	3.5E-02	1.5E-01	1.2E+00	9.5E-03	3.6E-01	1.5E-01	2.1E+01	3.6E+00	2.4E+01	2.5E+01	-1.3
123-011	2.9E+01	3.5E-01	9.7E-02	3.3E-01	1.3E+00	9.2E-03	2.1E+00	3.5E-01	2.3E+01	4.9E+00	3.2E+01	3.0E+01	1.8
123-012	2.8E+01	3.9E-01	6.5E-02	2.7E-01	1.4E+00	8.5E-03	2.2E+00	2.8E-01	2.2E+01	4.5E+00	3.0E+01	2.9E+01	1.5
123-001	2.1E+01	1.9E-01	1.1E-02	1.0E-01	1.1E+00	7.4E-03	4.7E-01	1.8E-01	1.8E+01	3.6E+00	2.2E+01	2.3E+01	-0.2
123-007	2.1E+01	2.3E-01	1.1E-02	1.1E-01	1.1E+00	8.5E-03	3.2E-01	1.5E-01	1.8E+01	3.5E+00	2.2E+01	2.2E+01	-0.2
170-004	2.1E+01	2.2E-01	*7.5E-03*	9.1E-02	1.2E+00	1.2E-02	2.9E-01	9.9E-02	1.8E+01	3.5E+00	2.3E+01	2.2E+01	1.2
170-005	2.7E+01	2.5E-01	2.3E-02	1.8E-01	1.5E+00	1.3E-02	2.3E-01	1.3E-01	2.4E+01	4.7E+00	2.9E+01	2.9E+01	-0.3
170-006	2.6E+01	2.4E-01	1.4E-02	1.7E-01	1.4E+00	1.2E-02	1.6E-01	1.0E-01	na	4.2E+00	2.8E+01	—	—
170-003	3.1E+01	3.3E-01	3.9E-02	2.9E-01	1.6E+00	1.1E-02	1.9E+00	1.9E-01	2.6E+01	5.3E+00	3.3E+01	3.3E+01	0.0
170-001	2.6E+01	2.6E-01	1.9E-02	1.7E-01	1.3E+00	8.0E-03	2.6E-01	4.7E-01	2.3E+01	4.3E+00	2.8E+01	2.8E+01	0.2
Pad-Blank-1	1.0E+01	7.7E-02	*6.0E-03*	3.6E-02	4.9E-01	1.9E-03	6.0E-02	4.1E-02	9.6E+00	1.8E+00	1.1E+01	1.2E+01	-1.9
Pad-Blank-2	1.2E+01	6.9E-02	*6.7E-03*	5.1E-02	5.5E-01	4.5E-03	6.4E-02	2.1E-02	1.1E+01	2.1E+00	1.2E+01	1.3E+01	-4.1
Pad-Blank-3	1.0E+01	6.1E-02	*3.6E-03*	2.9E-02	4.6E-01	3.1E-03	5.4E-02	2.4E-02	9.4E+00	1.9E+00	1.1E+01	1.1E+01	-2.7

Notes: Italicized values in gray were above blank values, but too low to quantify accurately. na = not analyzed.

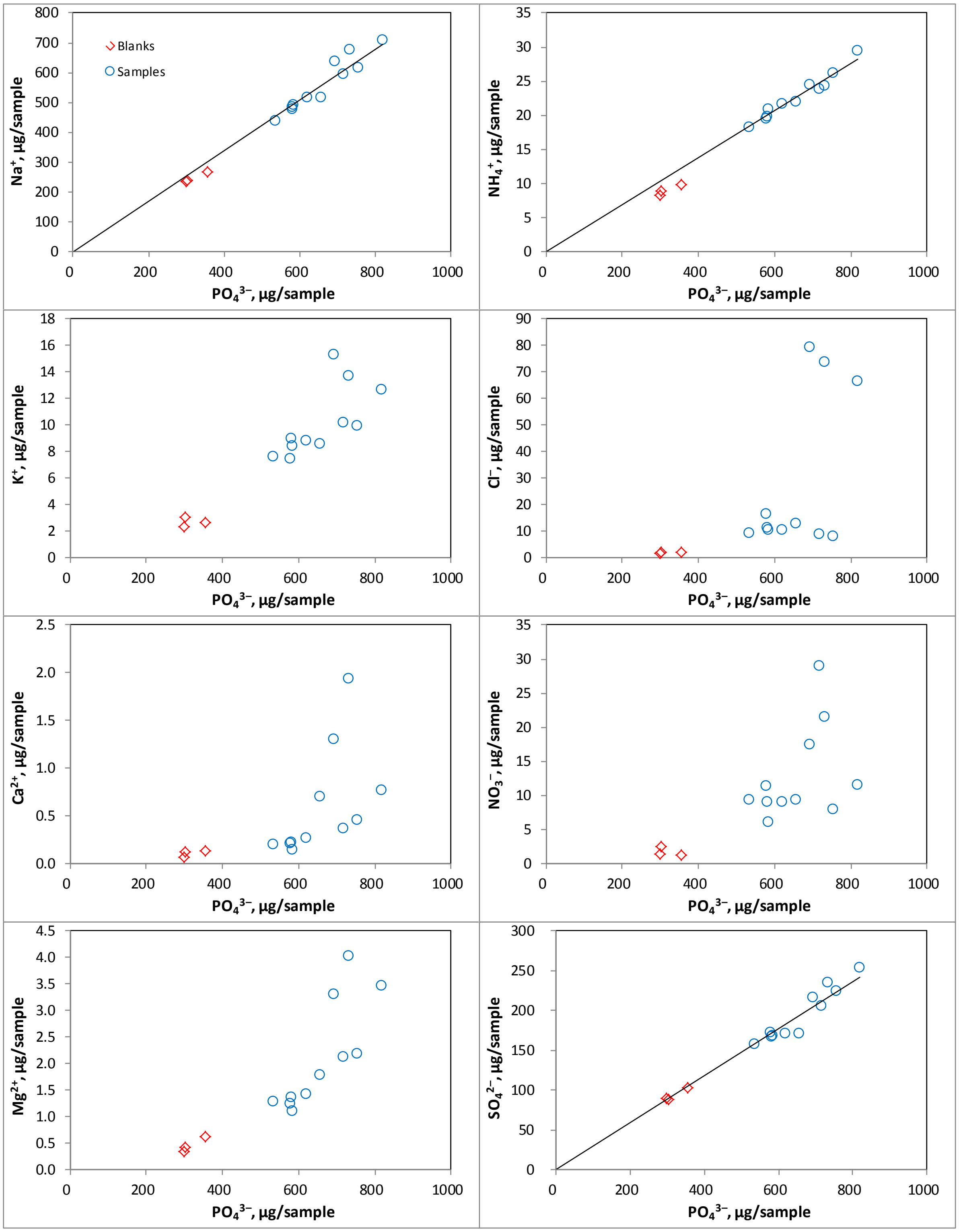

Figure 35. Plots of soluble species concentration versus PO43– concentration for the Diablo Canyon dry pad samples.

2.5 Conclusions

As part of a program to characterize possible environments on the surface of spent nuclear fuel dry storage canisters, the Electric Power Research Institute has sampled dust on the surface of in-service storage canisters at three different near-marine Independent Spent Fuel Storage Installations. Following collection, the samples from the final two sites, the Hope Creek and Diablo Canyon ISFSIs, were sent to Sandia National Laboratories for chemical and mineralogical characterization.

Two canisters were sampled at each site, and two different types of samples were collected. First, SaltSmart™ sensors were used to sample the soluble salts on the canister surface. Ideally, the SaltSmart™ sensor samples provide, upon analysis, salt and chloride loads per unit surface area. Second, an abrasive sponge was brushed across the metal surface, dislodging and collecting dust. Although the dry pad samples do not allow quantification of the salt load per unit area, the collected dust was analyzed by SEM/EDS to provide mineralogy and textural information. Additional compositional information was gained by XRF analysis of the dust on the dry pads, and by leaching and analysis of soluble salts on the pads. These data complement that collected by the SaltSmart™ sensors.

Both methods had limitations. The SaltSmart™ wicks are widely used in industry, and quantitatively leach salts from the contacted surface at room temperature (Memo from C. Bryan to L. Zsidai dated Nov. 13, 2013; SAND#2013-9948P). However, their stated operational temperature limit of 90ºC limited their use on the hot Diablo Canyon canisters; moreover, their performance actually degraded at temperatures greater than ~80ºC, affecting most of the samples collected from the Diablo Canyon canisters. The dry sponge pads had no temperature limitations, and were used sample the entire surfaces of the canisters at both Hope Creek and Diablo Canyon. Although the dry pad samples were effective for providing dust mineralogical and textural information, the matrix of the pads leached many chemical species that are potentially in the dust (especially Na^+, SO_4^{2-}, PO_4^{3-}, and NH_4^+), limiting their use for determining soluble salt compositions.

Despite the limitations of the methods utilized, samples from the two sites were successfully characterized. At both sites, canister tops were much more heavily loaded with dust than canister sides, and terrestrially-derived silicate minerals, including quartz, feldspars, micas, and clays, comprise the largest fraction of the dust. Also significant at both sites were particles of iron and iron-chromium metals and oxides generated by the manufacturing process. Soluble salt phases were a minor component of the Hope Creek dusts, and were compositionally similar to inland salt aerosols, rich in calcium, sulfate, and nitrate. Chloride surface loads were very low, <8 mg/m2 on the canister sides and ≤60 mg m^{-2} on the canister tops. At Diablo Canyon, however, sea-salt aerosols, occurring as aggregates of NaCl and Mg-sulfate with trace amounts of K and Ca, were a major component of the dust samples. The sea-salt aerosols were 5-20 µm in diameter, and commonly occurred as hollow spheres, which may have formed by evaporation of suspended aerosol seawater droplets, possibly while rising through the heated annulus between the canister and the overpack. Although sea-salt aggregates were a significant component of the dusts on the Diablo Canyon canisters, measured chloride loads on the canister sides were very low (<5 mg m^{-2}). Damage to the sensors at the elevated sampling temperatures suggests that salt recovery from the surface may not have been complete, so these results should be treated with caution; they may underestimate the actual salt loads at the areas sampled. Even if the measured salt loads at Diablo Canyon are accurate, they may not be bounding, because the heavily-loaded canister tops at Diablo Canyon were too hot to sample using the SaltSmart™ sensors.

An additional reason why the salt and chloride loads measured at both Hope Creek and Diablo Canyon may not be bounding is that the sampling was done through outlet vents; the sampled locations, extending downward for the outlet vents, were not proximal to inlet vents, where salts may preferentially be deposited.

The differences in salt composition and abundance for the two sites are attributed to differences in proximity to the open ocean and to wave action. The Diablo Canyon facility is on the shores of the Pacific Ocean, while the Hope Creek facility is on the shores of the Delaware River, several miles from the open ocean. Hence, the Hope Creek dusts have a negligible component of coarse wave-derived sea salt aerosols.

Finally, at Diablo Canyon, nitrate salts were found in the finest fraction of the surface dust, but on only one of the two sampled canisters. The nitrates occurred on the canister with the hottest surface temperatures. We conjecture that the hot surface temperatures prevented deliquescence of the salts and degassing of the nitrate as nitric acid. Alternatively, perhaps the presence of nitrates is tied to vent and wind directions, and differences in source direction; sampling was carried out on opposite sides of the two canisters evaluated at Diablo Canyon.

3. LARGE-SCALE INTERIM STORAGE CONTAINER MOCK-UP

3.1 Overview

Stress corrosion cracking (SCC) of interim storage containers has been indicated as a high priority data gap by DOE (Hanson et al. 2012), EPRI (2011), NWTRB (2010), and the NRC (2012a, 2012b). Uncertainty exists both in terms of the environmental conditions that exist on the surface of the storage containers (as discussed above/below) as well as for the behavior of the storage containers themselves. The goal of this task is to enhance the understanding of the latter aspect of the issue.

The material used to construct the storage containers, as well as the manner through which the containers are constructed (i.e., formed and welded plates) dictates not only the susceptibility of the material to localized attack such as SCC, but also provides the driving force (i.e., the stress) for crack propagation in the form of residual stresses from welding and, to a lesser extent, forming of the metal plates used to build the storage container. The primary material of construction across the various cask designs in use today is 304SS (Hanson et al. 2012), a material that has been demonstrated throughout the literature to be susceptible to chloride induced stress corrosion cracking.

Due to the carbon content of 304SS, when welded it is prone to a phenomenon known as sensitization. The thermal cycling associated with welding facilitates the precipitation of chromium carbides. As the chromium diffusion rate is significantly faster along grain boundaries than within the bulk, these carbides tend to grow at the grain boundaries, being supported by the rapid mass transfer of chromium at such sites. In time, zones where the chromium has been significantly depleted are formed along the grain boundaries. These chromium depleted zones are significantly less corrosion resistant than the surrounding grains, and serve as a preferential site for localized corrosion to initiate, potentially providing a crack initiation site (and fast growth path) for stress corrosion cracking.

In order to assess the implications of the environment that develops on the surface of an interim storage container, it is essential that the susceptibility of the container, in particular, the weld regions, be understood. As such, a full-scale mockup storage container has been fabricated. The text which follows outlines the various techniques which will be used to determine

1. The near surface and through-thickness residual stress states associated with the welds used to construct the container
2. The near-surface and through-thickness residual stress states associated with the as-formed walls of the container (i.e., far from the welds)
3. The degree of sensitization associated with the various weldments used to form the container
4. The resistance of the container in both the welded and un-welded regions to stress corrosion crack initiation and propagation

3.2 Container design

The designs used by each of the primary vendors, in particular, the ones that have been fielded for an extended period of time, were reviewed for their materials and methods of construction. Nearly all designs used 304SS (for older containers) and welding was multi-pass and typically done via the submerged arc welding process with a double-V edge preparation. Inquiries, followed by requests for quote were made to Holtec, NAC, and Areva-TN (formerly Transnuclear). After much deliberation, the decision was made to pursue the TransNuclear NUHOMS® 24P design. This container design is employed at the Calvert Cliffs nuclear power station, which was the first site surveyed by EPRI for the dust composition on the surface of the containers (Gellrich, 2013). The mock-up, pictured schematically in Figure 36 below, consisted of three cylindrical shells, each being 48 inches high, 67.2 inches in diameter, and with a wall thickness of 5/8 inch. Each shell was formed by cold forming a plate into a cylinder, then making a single longitudinal weld to form the cylinder. The three cylinders were then welded together to form a single large cylinder 12 feet in length with two circumferential welds. All of the welds were formed via the submerged-arc welding process and were multi-pass. The inner diameter was welded first, followed by the outer diameter.

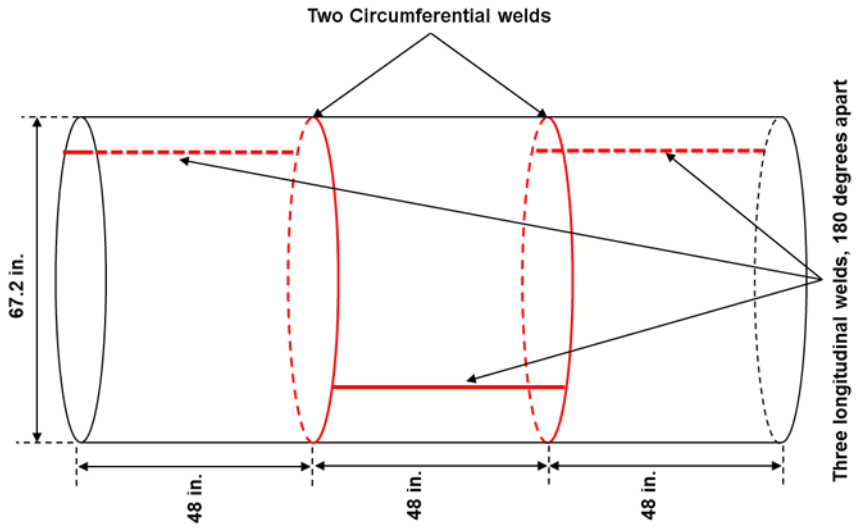

Figure 36. Schematic representation of the full scale mock storage container manufactured at Ranor.

Production of the container was done at Ranor (located in Westminster, MA), the fabrication facility where the containers located at the Calvert Cliffs site were produced. Use of the same manufacturer was critical as, while the overall design is owned by Areva-TN, the production methodologies used are proprietary to Ranor. In other words, Areva-TN specified the overall design (i.e., material, overall dimensions, etc.) but Ranor had to figure out how to build it.

An extensive data package is being supplied along with the container. This will assist in our understanding how the material was treated, as well as enable the use of models aimed at predicting the properties of the container. For the welds, the key parameters documented include:

1. Compositional information on the weld metal and flux materials used to form each weldment
2. Number of passes and their deposition sequence, inter-pass temperature, and other process related details such as weld speed, etc.
3. Joint design and fabrication procedure (including a schematic of the joint design, the techniques used to fabricate it, etc.)
4. The nature of any fixtures (external or temporarily welded in place) used to minimize distortion and assist with assembly
5. Method of flux delivery (flux cored wire, powder delivered to weld via a hopper, etc.)

In addition to welds formed under nominal conditions, discussions with Transnuclear and Holtec have indicated that there will likely be repaired regions along the welds, for regions where the nondestructive testing indicated that the weld did not conform to the criteria in ASME B&PVC Section III, Division 1, Subsection NB. As such, all of the welds were subjected to a full radiographic inspection, and any indications requiring repair were addressed. In the event that the welds did not have any issues, a region of each circumferential weld was subjected to a repair procedure on the outer diameter. As with the basic welding, an extensive data package is being supplied for the non-destructive evaluation and subsequent repair procedures. For the non-destructive evaluation, that package includes:

1. Radiography for all weldments
2. A marking system that enables identification of where each image is from. Indications made on the container shall be a minimum of 6 inches from the center of the nearest weldment.

The location of all repairs will be similarly marked on the surface of the container, with radiography provided for the region both before and after the completion of the repair (irrespective of whether the repair was done to address an actual defect, or if it was done to demonstrate the impact of the repair process)

3.3 Test Plan

The large scale mock-up container represents a substantial investment by the Used Fuel Disposition program, and will be used to facilitate research at many of the laboratories performing work aimed at understanding the behavior of interim storage containers. The test plan below outlines the basic steps that will be taken in analyzing the container. It should be stressed that the text below serves as an overview, and that the detailed plan will be developed as part of the UFD work-scope for FY15. This plan will progress in two stages. In the first, the container will be assessed in its entirety. Specifically, efforts will be made to evaluate the residual stress states associated with the weldments and in the walls far from the welds. These stresses are the result both of the processes used to form the container, as well as the mechanical constraint provided by the overall container geometry. Thus, as the container is subdivided into smaller sections, the constraint will be relaxed, and the stress state within the container walls potentially changed. A secondary goal of the work defined below is to establish to what extent stress relaxation occurs as the sample is subdivided, to establish what the minimum sample size is to maintain the stress state in the as-formed container, as well as to determine to what extent the residual stress has been alleviated in samples which are insufficiently large to maintain the as-formed stress state.

3.3.1 Assessment of Residual Stresses within the Welded and Un-welded Regions

In addition to a susceptible material and a sufficiently aggressive environment, the nucleation and growth of a stress corrosion crack requires the presence of a sufficiently large stress. In the case of interim storage containers, the stress existing with the structure will be predominantly residual stress resulting from the forming of the metal plates into a cylinder and the subsequent welding of the panels. The latter are likely to be the largest in magnitude, and are the result of the constraint placed by the structure of the container (and any additional fixtures used during fabrication) on the weld as it solidifies. A wide variety of methods are available for residual stress measurement, as summarized in NUREG-2162 (Benson, 2014). Techniques are typically based on either diffraction of X-rays or neutrons, or upon strain measurements made upon mechanically altering the material being investigated. The techniques vary in terms of their sensitivity and depth of penetration into the substrate metal. The most appropriate technique for assessing the mock-up storage container will be one capable of measuring the stresses through the thickness of the container wall. Furthermore, the technique must allow for evaluation of large sections, as it is desired that the stress state be measured prior to and following the sectioning of the container into smaller samples for use in corrosion or stress corrosion cracking experiments.

Three techniques have been initially targeted for use in this study. These include neutron diffraction, the contour method, and the deep-hole drilling method. Neutron diffraction will be explored via collaboration with LANL. The other two techniques will also involve collaboration with other groups, though located at SNL.

3.3.2 Assessment of the Degree of Sensitization in the Weld Heat Affected Zones

As discussed above, the thermal cycling associated with the welding process will result in the precipitation of chromium carbides and the formation of chromium depleted regions along the grain boundaries. This effect will be particularly pronounced in the weld heat affected zone (i.e., the region near the weld fusion zone that has been impacted by the heat input from the welding process). The extent to which sensitization has taken place will be documented as a function of position from the edge of the weld fusion zone. This will be done both for the near surface regions, as well as through the thickness of the container wall. A volumetric assessment of the degree of sensitization will illustrate the extent of the region and illustrate the presence/absence of an active path for crack propagation through the material.

Samples taken from the container will be prepared metallographically and evaluated electrochemically for the degree of sensitization. Evaluation will be done through either the single loop electrochemical reactivation (EPR) test or double-loop EPR test. For the single loop test, as defined in ASTM G108 "Standard Test Method for Electrochemical Reactivation (EPR) for Detecting Sensitization of AISI Type 304 and 304L Stainless Steels", the surface to be analyzed is polarized anodically such that the surface is activated. This results in enhanced dissolution of the chromium depleted grain boundaries, while the remainder of the grain is rendered passive. The net charge associated with dissolution of the chromium depleted regions along the grain boundaries is determined based upon the total current passed during the aforementioned polarization. This technique requires characterizing the microstructure of the material (specifically, the grain size), such that the overall charge per unit area of grain boundary can be calculated, the magnitude of which defines the extent of sensitization. The second technique is a modification of the first, and is more suitable for instances where the surface finish of the material being evaluated is less well defined, or measurement of the grain size within the material is difficult. This technique, developed by ASTM, 1995 is known as the double-loop EPR technique. In this method, the sample is essentially subjected to the same polarization as the single loop EPR, but it is applied twice. The ratio of the peak currents extracted from the first and second polarization is then recorded. The magnitude of this ratio is directly related to the degree of sensitization of the material. For an un-sensitized microstructure, the first polarization passivates the sample, such that the peak current from the second polarization is considerably lower than the first. However, in the case of a sensitized microstructure, the chromium depleted zones are not passivated by the first polarization, and the peak current for the second polarization will be large, approaching the value of the first polarization. The magnitude of the ratio is used to assess the degree of sensitization, with the value approaching 1 for heavily sensitized materials.

In the event that the electrochemical techniques are insufficient to define the degree of sensitization of the container wall material, alternate methods will be pursued, such as those defined in ASTM A262 "Standard Practices for Detecting Susceptibility to Intergranular Attack in Austenitic Stainless Steels" This specification provides a series of immersion tests designed to activate grain boundaries such that the extent of attack can be assessed either via metallography or weight change measurement.

3.3.3 Assessment of the Stress Corrosion Cracking Susceptibility of the Container

Establishing the susceptibility to SCC will require both the resistance to crack nucleation as well as the magnitude of crack propagation to be assessed as a function of the environmental conditions to which the container is subjected while exposed to stresses as defined by the full scale mock-up. A wide variety of experiments are planned,

1. The information learned from the residual stress measurements, combined with the electrochemically determined degree of sensitization will enable the fabrication of material simulating the weld heat affected zone. A Gleeble instrument will be used to replicate the

thermomechanical processing to which the heat affected zone has been subjected. These samples will then be used in simple U-bend experiments, where marine aerosols are deposited on the surface of the bent portion of the sample (replicating the surface deposits observed via in-service inspections, as well as predicted worst-case deposits), then subjected to combinations of humidity and temperature typical of coastal ISFSI sites.

2. Crack propagation studies will be conducted using compact tension specimens where the microstructure has been modified so as to accurately simulate the conditions in the heat-affected zone of welds on actual storage containers. The surface deposits and exposure conditions will be similar to those explored for U-bend specimens.
3. Specimens taken from the large scale mockup, sized so as to maintain a residual stress distribution similar to that for the as-received condition will be used for crack initiation and propagation studies. A combination of worst case and field representative deposits will be placed on the surface of the samples, after which they will be subjected to relevant temperature and humidity exposure. It should be noted that these samples will be limited in number, and as such the aforementioned tests will be used to define the conditions used to evaluate specimens taken from the mock-up.

4. CREVICE CORROSION IN LIMITED REACTANT

The materials used to construct most interim storage containers (i.e., austenitic stainless steels such as 304 and 316) are susceptible both to localized attack and stress corrosion cracking in chloride rich solutions. The goal of the work discussed in this section is to explore the susceptibility of these materials in terms of the extent of attack that can be supported under atmospheric conditions, where a bulk electrolyte is not present. Understanding the susceptibility of the materials to localized attack will provide considerable insight into the existence of potential SCC nucleation sites on the metal surface, as well as the extent of electrochemical activity (crevice corrosion, pitting, or SCC) that can be supported under such conditions.

Researchers have suggested that for highly corrosion resistant/passive materials, several factors will prevent extensive localized corrosion due to the presence of a thin electrolyte layer. Turnbull (1997) demonstrated for cracks and crevices that if the cathodic reactions which support the dissolution taking place at the corrosion site are pushed into the occluded geometry of the crack/crevice, that the pH would increase (due to hydroxyl ion production at the cathode), resulting in an inhibiting effect. Essentially, by moderating the pH it would not be possible to form and maintain the critical crevice solution required for continued activity of the crevice. More recently, Payer (2008) and Kelly (2006) demonstrated that the capacity of the external cathode controls the extent to which a crevice may propagate. Furthermore, Payer (2008) demonstrated that the capacity of the cathode would be determined by the quantity of salt/contaminant available on the metal surface outside of the crevice, as it dictates the volume and properties of the brine layer. In addition to the electrochemical limitations, physical limitations (e.g., limited volume of brine coupled with consumption or sequestration of aggressive species in the corrosion product) can also play a role in governing the stability of a localized corrosion site.

In an effort to determine if there is indeed a potential for deliquescent brines to result in extensive localized corrosion, or if any localized corrosion will stifle due to limitations as described above, a series of experiments has been performed. 304SS coupons were decorated with thin layers of salt in the presence of an occluded geometry in an effort to establish if localized corrosion (i.e., crevice corrosion) could initiate and propagate under such conditions. In these experiments, no inert species were added, so potential physical sequestration of the brine by the dust layer due to capillary forces have been eliminated, allowing all of the material deposited on the metal surface to participate in the corrosion reaction.

The 304SS samples with three replicates of 50, 100 and 200 µg/cm^2 salt loadings were exposed for 7, 14, 25, 50 and 100 days. Each sample had a multiple crevice former assembly placed on it as illustrated in Figure 37 below. After removing the samples from the environmental chamber and allowing them to cool, the crevice former assembly was taken apart and the residual surface salt and metal oxides on the coupon were cleared away via sonication in distilled water. The post environmental exposure sample in Figure 38 was exposed for 7 days and had a 200 µg/cm^2 salt loading.

A complete survey of the edge around each tooth was conducting using SEM imaging. Images were taken around the circumferential edge of each tooth in the pattern shown in Figure 39. The outer circle is the edge of the salt coating. The first three teeth are outlined; even in SEM images the tooth edge, and therefore the area where crevice corrosion can occur, was usually apparent. These images were used to conduct a thorough survey of the extent of crevice corrosion on all teeth in each sample. The number density and two dimensional surface area of the various sites have been presented previously in FCRD-UFD-2013-000324 (Enos et al. 2013).

In previous reports, the number density and two-dimensional area of crevice corrosion sites was presented in an attempt to characterize the nucleation and growth of crevice corrosion sites as a function of time and salt loading on the surface. In those data, there was no apparent corrosion stifling in the time period observed, and it was not clear if this observation is due to an insufficiently long time interval for the experiments reported here or if stifling simply does not occur under these conditions, or if some other factor were determining the response. Regardless of how much total corrosion area was observed for each sample, the results provided convincing evidence that more aggressive attack corresponding with more volume loss is observed with increasing exposure time. However, without actual volume data for each site, it wasn't clear if there is a distinct trend of increasing total volume loss as a function of exposure time throughout the 7-100 day time frame.

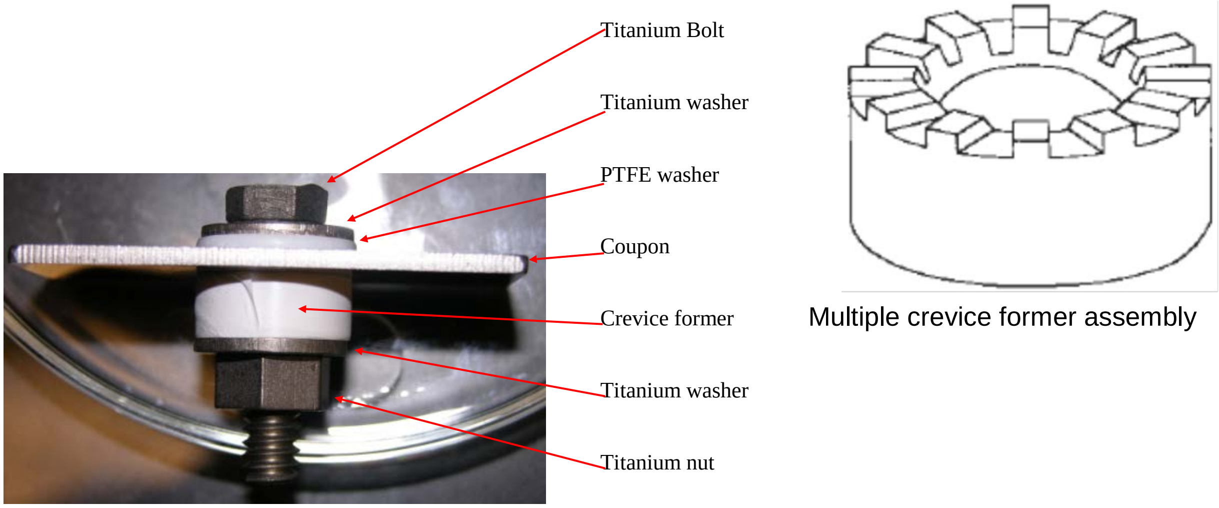

Multiple crevice former assembly

Figure 37. Experimental configuration for crevice corrosion experiments. The MCA was held in place via a torque of 70 in-lbs. Salt was deposited only on the side where the MCA was located.

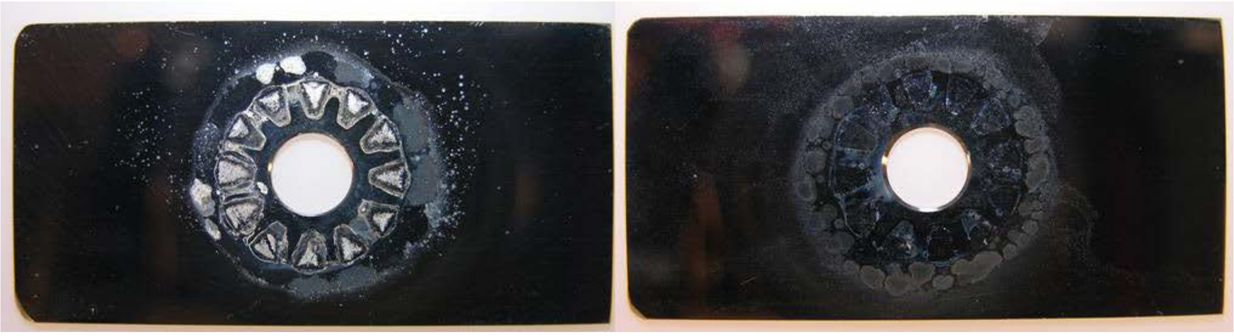

Figure 38. 304SS coupon with 200 µg/cm^2 and 7 day exposure after crevice former removal (L) and rinsing (R).

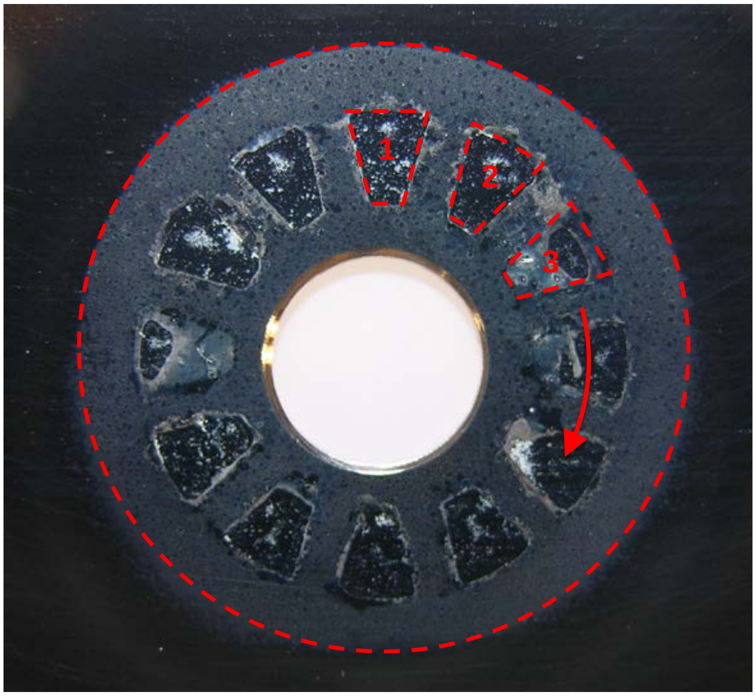

Figure 39. Crevice corrosion site survey location and pattern.

Laser confocal microscopy was used to assess the depth and volume of typical crevice corrosion sites. In past work, the sites were generically classified based upon their perceived depth from SEM images. The actual data from the laser confocal microscopy was combined with the previously reported area data in order to provide an approximate volume of corrosion as a function of salt loading and exposure time. The total volume, estimated as described, is presented in Figure 40 as a function of salt loading and exposure time. As seen in the figure, the change in total volume of attack from 50 to 100 days is substantial, and indicates that stifling has not yet occurred. As expected, with time the number (and hence overall volume) of larger, deep sites increases with time irrespective of the salt loading, as illustrated in Figure 41.

The data presented below, combined with the number density of crevice sites presented previously in (Enos, 2013) indicate that site nucleation occurs primarily at early times, perhaps within the first few weeks of exposure, followed by growth of the sites over time. It is not clear why such a substantial increase in volume occurred between the 50 and 100 day data sets. One possible explanation is that the material source, and hence the composition and underlying microstructure, of the samples used for the 100 day tests (which were the first experiments performed) was different than that used for the later tests. As such, tests will shortly be underway using material from the 7 and 14 day experiments that have been re-polished and loaded with salt for 100 and 150 day exposures. These experiments should first, establish if the 100 day is an anomalous result related to the material source, and second, determine is site growth continues beyond the 100 day mark or if it stifles.

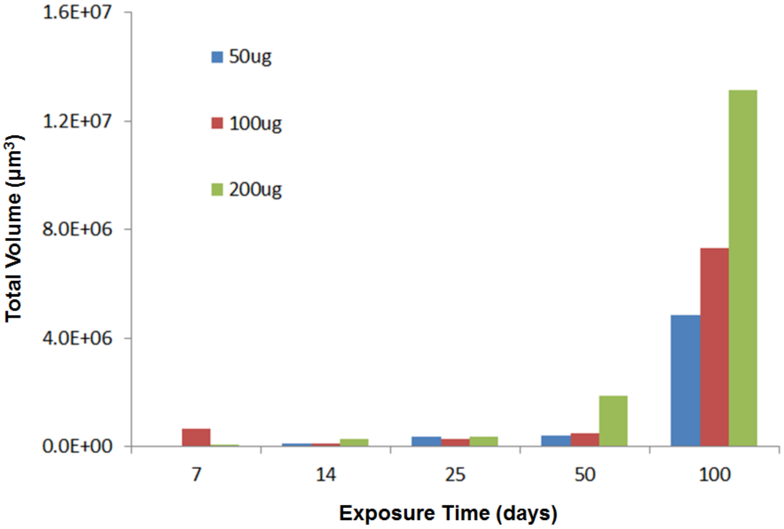

Figure 40. Estimate total crevice corrosion volume as a function of salt loading and exposure time. Volumes are based upon laser confocal microscope measurements taken from representative sites corresponding to the different site geometry “bins” used when reporting the 2-D surface area of corrosion sites.

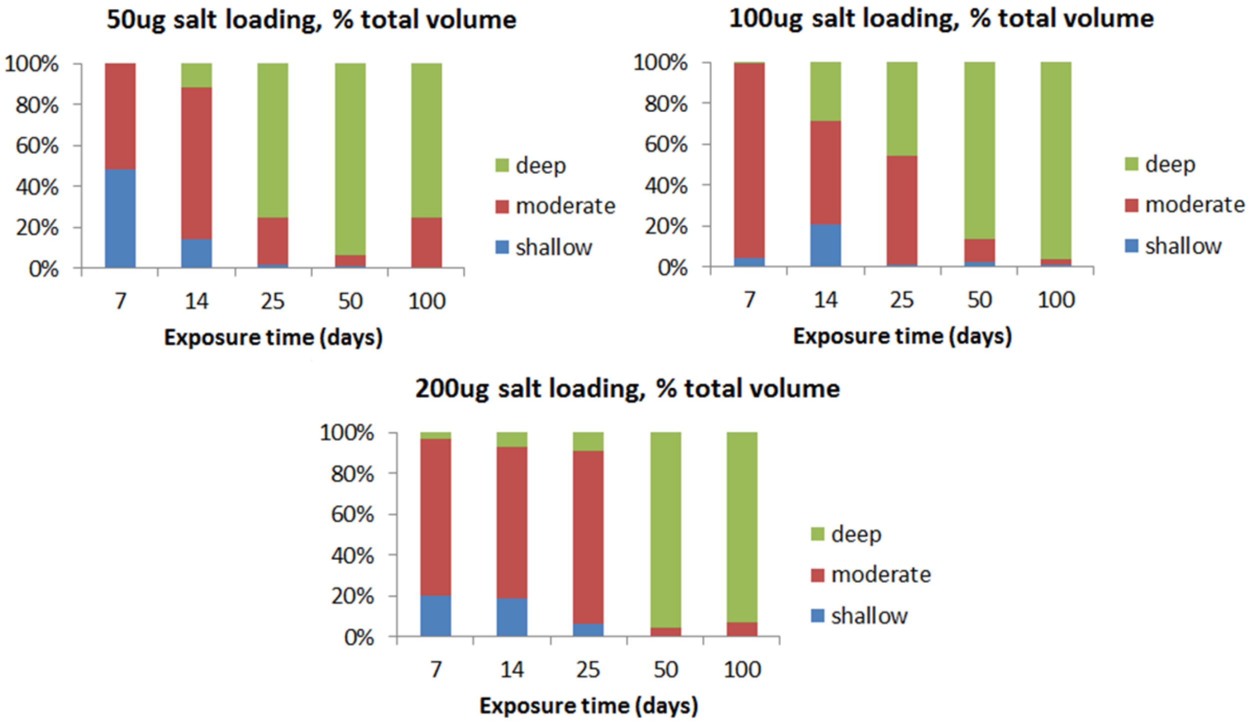

Figure 41. Corrosion site distribution as a function of time for each loading level. Shorter times are dominated by shallow and moderate depth sites, while longer times are dominated by deep sites.

5. SALT DEPOSITION

In addition to the crevice corrosion experiments described above, future experiments to be performed to assess the SCC properties of interim storage container materials when subjected to marine aerosols will require a means to accurately deposit low concentrations of salt solutions onto the sample surface. Such a system is also needed for exploration of brine chemistry evolution on the surface of heated surfaces (i.e., to evaluate how marine aerosols evolve compositionally with time when deposited on the surface of a loaded spent nuclear fuel container).

A system has been developed centered around commercial air-brush designs to deposit marine aerosols. An x-y plotter system is used to manipulate the airbrush to deposit aerosolized salt on samples within a 50-200 $\mu g/cm^2$ loading range. Directional maneuvering of the airbrush is controlled using an 18 inch x-y linear, belt driven positioner and motion control system employing stepper motors (C4/MD2 Stepper Motor System, Arrick Robotics, Tyler, TX). The x-y positioner can be used for single pass coats or can be programmed to raster back and forth depositing overlapping coats over a larger area. The airbrush is attached to the x-y positioner stage and its vertical position relative to the sample being coated can be adjusted to accommodate a range of stand-off distances. A variety of commercial airbrush models (Badger Air-Brush Co., Franklin Park, IL) including both internal and external mix designs, are used for deposition, depending on the desired coating. The internal mix models (150 and 200-20) mix air and salt solution inside the brush tip, while the external mix brush (Model 350) mixes the air and salt solution streams external to the brush tip but surrounded by a nozzle to provide directional control. Compressed air is used as the carrier for the airbrush, and the salt solutions are fed to the brush via a syringe pump (KD Scientific, Holliston, MA), with flow rates ranging from 0.5 to over 200 mL/h. Figure 42 illustrates an internal mix airbrush attached to the system.

The sample being coated is secured to a vacuum hot plate (Gel Dryer, Labconco, Kansas City, MO) so salt can be deposited on heated samples in the 40-80°C range if desired. The surface to which the sample is mounted is large, allowing multiple samples (or a single large sample) to be coated at once. A Maxtek Research Quartz Crystal Microbalance (R-QCM, Inficon Inc., East Syracuse, NY) is used to monitor salt deposition in real time. For ambient temperature salt deposition, a crystal holder is used to position the QCM crystal such that it is at the same vertical distance from the airbrush as the sample being coated. Dry deposition at ambient temperature using low solution feed rates (0.5-1 mL/h) has yielded the most uniform coatings for depositing sea salt. Deposition of 50/50 NaCl/KCl is best accomplished via wet deposition using a methanol solvent and an external mix airbrush with a high solution feed rate of 200mL/h.

In addition to depositing NaCl/KCl mixtures as used in the crevice corrosion experiments described above, an effort was made to deposit marine aerosols using a salt chemistry similar to that described in ASTM D1141 “Standard Practice for the Preparation of Substitute Oceanwater”. The chemistry deviated from that mixture in that minority constituents were omitted. While the NaCl/KCl salt mixture was readily deposited with a methanol carrier, this was not the case for the oceanwater. One of the main constituents, sodium sulfate (Na_2SO_4) is insoluble in alcohols. Several attempts were made to grind the material into a fine powder to be incorporated into the solvent (to be deposited as a solid), but XRD analysis of the resulting deposit indicated that the composition differed from that of a salt layer that would evolve from evaporation of an aqueous solution. As a result, experiments were initiated using alcohol-water mixtures as well as water alone. While deposition is more difficult with these solutions, the resulting deposit had the desired chemical composition.

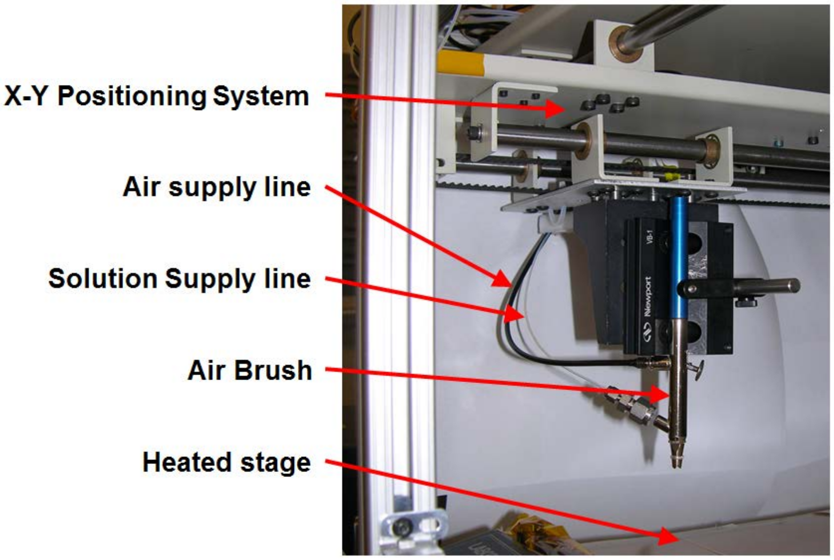

Figure 42. Salt aerosol deposition system used to apply well defined salt loadings using either a water or methanol carrier solvent. Both NaCl/KCl mixtures and a mixture simulating ASTM artificial ocean water (salt loading per ASTM D1141).

6. CONCLUSIONS

This progress report describes work being done at Sandia National Laboratories (SNL) to assess the localized corrosion performance of container/cask materials used in the interim storage of used nuclear fuel. The work involves both characterization of the potential physical and chemical environment on the surface of the storage canisters and how it might evolve through time, and testing to evaluate performance of the canister materials under anticipated storage conditions.

To evaluate the potential environment on the surface of the canisters, SNL is working with the Electric Power Research Institute (EPRI) to collect and analyze dust samples from the surface of in-service SNF storage canisters. In FY 13, SNL analyzed samples from the Calvert Cliffs Independent Spent Fuel Storage Installation (ISFSI); here, results are presented for samples collected from two additional near-marine ISFSI sites, Hope Creek NJ, and Diablo Canyon CA. The Hope Creek site is located on the shores of the Delaware River within the tidal zone; the water is brackish and wave action is normally minor. The Diablo Canyon site is located on a rocky Pacific Ocean shoreline with breaking waves.

Two types of samples were collected: SaltSmart^{TM} samples, which leach the soluble salts from a known surface area of the canister, and dry pad samples, which collected a surface salt and dust using a swipe method with a mildly abrasive ScotchBrite™ pad. The dry samples were used to characterize the mineralogy and texture of the soluble and insoluble components in the dust via microanalytical techniques, including mapping X-ray Fluorescence spectroscopy and Scanning Electron Microscopy. For both Hope Creek and Diablo Canyon canisters, dust loadings were much higher on the flat upper surfaces of the canisters than on the vertical sides. Maximum dust sizes collected at both sites were slightly larger than 20 µm, but *Phragmites* grass seeds ~1 mm in size, were observed on the tops of the Hope Creek canisters. At both sites, the surface dust could be divided into fractions generated by manufacturing processes and by natural processes. The fraction from manufacturing processes consisted of variably-oxidized angular and spherical particles of stainless steel and iron, generated by machining and welding/cutting processes, respectively. Dust from natural sources consisted largely of detrital quartz and aluminosilicates (feldspars and clays) at both sites. At Hope Creek, soluble salts were dominated by sulfates and nitrates, mostly of calcium. Chloride was a trace component and the only chloride mineral observed by SEM was NaCl. Chloride surface loads measured by the Saltsmart™ sensors were very low, less than 60 mg m^{-2} on the canister top, and less than 10 mg m^{-2} on the canister sides. At Diablo Canyon, sea-salt aggregates of NaCl and Mg-SO_4, with minor K and Ca, were abundant in the dust, in some cases dominating the observed dust assemblage. Measured Saltsmart™ chloride surface loads were very low (<5 mg m^{-2}); however, high canister surface temperatures damaged the Saltsmart™ sensors, and, in light of the SEM observations of abundant sea-salts on the package surfaces, the measured values may not be valid.

Experimental efforts at SNL to assess corrosion of interim storage canister materials include three tasks in FY14. First, a full-diameter canister mockup, made using materials and techniques identical to those used to make interim storage canisters, was designed and ordered from Ranor Inc., a cask vendor for Areva/TN. The mockup will be delivered prior to the end of FY14, and will be used for evaluating weld residual stresses and degrees of sensitization for typical interim storage canister welds. Following weld characterization, the mockup will be sectioned and provided to participating organizations for corrosion testing purposes. A test plan is being developed for these efforts.

In a second task, experimental work was carried out to evaluate crevice corrosion of 304SS in the presence of limited reactants, as would be present on a dust-covered storage canister. This work tests the theory that limited salt loads will limit corrosion penetration over time, and is a continuation of work carried out in FY13. Laser confocal microscopy was utilized to assess the volume and depth of corrosion pits formed during the crevice corrosion tests. Results indicate that for the duration of the current experiments (100 days), no stifling of corrosion occurred due to limitations in the amount of reactants present at three different salt loadings.

Finally, work has been carried out this year perfecting an instrument for depositing sea-salts onto metal surfaces for atmospheric corrosion testing purposes. The system uses an X-Y plotter system with a commercial airbrush, and deposition is monitored with a quartz crystal microbalance. The system is capable of depositing very even salt loadings, even at very low total deposition rates.

7. REFERENCES

ASTM, 1995. *Corrosion Tests and Standards: Application and Interpretation. Chapter 7: Electrochemical Tests*, R. Baboian (Ed), ASTM manual series; MNL-20, ASTM International.

Benson M., Rudland D., and Csontos A., 2014. *Weld Residual Stress Finite Element Analysis Validation: Part 1 – Data Development Effort*, NUREG-2162, U.S. Nuclear Regulatory Commission.

Bryan C. and Enos D., 2013, *Memo to Laszlo Zsidai of Holtec International entitled: Analysis of SaltSmart™ Samples from Holtec Test Run*, SAND2013-9948P, Sandia National Laboratories, Albuquerque, NM, November 2013.

Bryan C. and Enos D., 2014, *Analysis of Dust Samples Collected from Spent Nuclear Fuel Interim Storage Containers at Hope Creek, Delaware, and Diablo Canyon, California*, SAND2014-16383, Sandia National Laboratories, Albuquerque, NM, July 2014, 281 p.

Calvert Cliffs Nuclear Power Plant, 2012. *Response to Request for Additional Information, RE: Calvert Cliffs Independent Spent Fuel Storage Installation License Renewal Application (TAC No. L24475)*, ADAMS ML12212A216.

Calvert Cliffs Nuclear Power Plant, 2013. *Response to Request for Additional Information, RE: Calvert Cliffs Independent Spent Fuel Storage Installation License Renewal Application (TAC No. L24475)*, ADAMS ML13170A574.

Electric Power Research Institute (EPRI), 2011. *Extended Storage Collaboration Program (ESCP) Progress Report and Review of Gap Analyses*, Technical report no. 1022914, EPRI Palo Alto, California.

Enos D., Bryan C., and Norman K., 2013. *Data Report on Corrosion Testing of Stainless Steel SNF Storage Containers*, FCRD-UFD-2013-000324 (SAND2013-8314P), Sandia National Laboratories.

Gellrich G.H., 2013. *Response to Request for Additional Information, Re: Calvert Cliffs Independent Spent Fuel Storage Installation License Renewal Application (TAC No. L24475)*, NRC Adams accession numbers ML13119A242, ML13119A243, and ML13119A244.

Hanson B., Alsaed H., Stockman C., Enos D., Meyer R., and Sorenson K., 2012. *Gap Analysis to Support Extended Storage of Used Nuclear Fuel*, FCRD-USED-2011-000136, Pacific Northwest National Laboratory.

Kelly R.G., Agarwal A., Cui F., Shan X., Landau U., and Payer J., 2006. *Considerations of the Role of the Cathodic Region in Localized Corrosion*, IHLRWM, April 30-May 4, 2006, Las Vegas, NV.

Nuclear Waste Technical Review Board (NWTRB), 2010. *Evaluation of the Technical Basis for Extended Dry Storage and Transportation of Used Nuclear Fuel*, NWTRB.

Nuclear Regulatory Commission (NRC) 2012a. *Potential Chloride Induced Stress Corrosion Cracking of Austenitic Stainless Steel and Maintenance of Dry Cask Storage System Canisters*, NRC Information Notice 2012-20, U.S. NRC, Washington D.C.

NRC 2012b. *Identification and Prioritization of the Technical Information Needs Affecting Potential Regulation of Extended Storage and Transportation of Spent Nuclear Fuel*. Draft for comment. U.S. NRC, Washington, D.C.

Payer J., Shan X., Agarwal A.S.,and Landau U., 2008. *Crevice Corrosion Processes in Thin Films of Electrolyte*, NACE Corrosion 2008, Paper no. 08266, March 2008, New Orleans, LA.

Turnbull, A., 1997. "Implications of Internal Cathodic Reactions for Crevice Attack of Stainless Steels in Chloride Environments", *British Corrosion Journal*, 32(4), p. 283-290.